

Copyright

by

Rongfeng Shen

2010

The Dissertation Committee for Rongfeng Shen
certifies that this is the approved version of the following dissertation:

**Exploring The Bizarrerie: Research on Selective Physical
Processes in Gamma-Ray Bursts**

Committee:

Pawan Kumar, Supervisor

J. Craig Wheeler

Edward L. Robinson

Volker Bromm

Bing Zhang

Peter Hoeflich

Miloš Milosavljević

**Exploring The Bizarrerie: Research on Selective Physical
Processes in Gamma-Ray Bursts**

by

Rongfeng Shen, B. E.; M.S.

Dissertation

Presented to the Faculty of the Graduate School of

The University of Texas at Austin

in Partial Fulfillment

of the Requirements

for the Degree of

Doctor of Philosophy

The University of Texas at Austin

August 2010

Acknowledgments

Firstly and foremost, I would like to thank my advisor, Pawan Kumar. He is a great mentor. Not only he is providing suggestions and guidance, but also he is bringing encouragement and confidence. I feel lucky to be his student.

I thank Bing Zhang, Miloš Milosavljević, Craig Wheeler and Rob Robinson for the privileges working with and/or getting advices from them. My special thanks go to colleague and collaborator Rodolfo Barniol Duran, with whom innumerable inspirational discussions on innumerable topics are adorable. I benefited tremendously from discussing literature with Jarrett Johnson, Erin McMahon, Patrick Crumley and Rodolfo Santana in the weekly GRB Journal Club. I thank officemate and colleague Chris Lindner for useful discussions on collapsar accretion.

I am indebted to my lovely wife, Dan, for her all time support and help.

RONGFENG SHEN

The University of Texas at Austin

August 2010

Exploring The Bizarrerie: Research on Selective Physical Processes in Gamma-Ray Bursts

Publication No. _____

Rongfeng Shen, Ph.D.

The University of Texas at Austin, 2010

Supervisor: Pawan Kumar

Gamma-ray bursts (GRBs) are the mysterious, short and intense flashes of gamma-rays in the space, and are believed to originate from the rare, explosively devastating, stellar events that happens at cosmological distances. Enormous progress has been made from four decades of GRB research endeavor but the ultimate understanding of their origins has yet to arrive. Recently revealed features in their early afterglows broadened the opportunity space for exploration. We have carried out extensive studies on various physical processes in GRBs. We showed that the distribution of electrons' energy spectral index in GRBs and other relativistic sources is inconsistent with the prediction from the first-order Fermi theory of the shock particle acceleration (Chapter 2). We investigated the photon scattering processes within the relativistic outflow that produces the GRB and calculated the resultant emission flux from it (Chapter 3). We showed the scattering of the GRB prompt photons by the circum-burst dust, although an attractive possibility, can not explain the puzzling

plateau component in the GRB afterglow light curve (Chapter 4). We made meaningful constraint on the GRB prompt emission radius, $R \geq 10^{14}$ cm, by studying the synchrotron self absorption for a small sample of bursts with good data (Chapter 5). We showed that a late jet, which is thought to be producing the late X-ray flares in GRB afterglows, will produce detectable emissions from its interactions with other components in the explosive event of GRB, and identification of these emissions could verify the existence of the late jet and further prove the massive star origin of long-duration GRBs (Chapter 6).

Contents

Acknowledgments	iv
Abstract	v
Chapter 1 Introduction	1
1.1 History	1
1.2 Observed behaviors	2
1.2.1 Prompt emission	2
1.2.2 Afterglow	4
1.3 Relativistic fireball model	5
1.4 Progenitors and central engines	6
1.4.1 Central engines	6
1.4.2 Progenitors of long bursts	7
1.4.3 Progenitors of short bursts	8
1.5 Recent development	9
1.5.1 <i>Swift</i> 's new discoveries	9
1.5.2 Interpretations	11
1.5.3 Implications for central engines and progenitors	13
Chapter 2 Non-Universality for Electrons' Power-Law Index p	15
2.1 Introduction	15
2.2 The distribution of p in GRBs	16
2.2.1 The GRB spectral sample	16

2.2.2	Distribution of p and its narrowing	17
2.2.3	Statistical description of the narrowness of p 's distribution	19
2.3	Systematic errors in β	21
2.3.1	The 'Band' function fit to the spectra	21
2.3.2	Time-averaging effect	23
2.4	p -distributions for BeppoSAX GRBs and HETE-2 XRFs, XRR GRBs and GRBs	25
2.5	p -distribution for X-ray afterglows	25
2.6	Distribution of p in Blazars and pulsar wind nebulae	26
2.6.1	Blazars	26
2.6.2	Pulsar wind nebulae	27
2.7	Summary and Discussions	28
Chapter 3 Scattered Emission from A Relativistic Outflow		30
3.1	Introduction	30
3.2	Emission from a relativistic shell	31
3.3	Two shells scenario	32
3.3.1	Incident flux on shell 2	34
3.3.2	Light path geometry	35
3.4	Scattering from shell 2	36
3.4.1	Scattered flux	36
3.4.2	Shell radii	38
3.4.3	Time dependence of scattered emission	38
3.5	Primary and scattered emission relations	39
3.5.1	Time delay	39
3.5.2	Ratio of frequencies	39
3.5.3	Ratio of observed durations	41
3.6	Results	42
3.6.1	Ratio between scattered and primary fluxes	42
3.6.2	Hot shell 2	43
3.7	Application to the shallow decay component in GRB early X-ray afterglows	46

3.7.1	Thomson scattering	46
3.7.2	Inverse Compton scattering in shell 2	49
3.8	Faster shell 2	51
3.9	X-Ray dim or dark GRBs	52
3.10	Summary and Conclusions	55
Chapter 4	Scattered X-ray Emission by Dust Grains near GRB Sites	57
4.1	Introduction	57
4.2	Spectral softening in dust echo emission	58
4.2.1	Extended dust zone	61
4.3	Search for spectral evidences in the data	64
4.3.1	Sample	64
4.3.2	Results	65
4.4	Time history of the spectral during the plateau	66
4.5	X-ray LCs in soft and hard energy channels	71
4.6	Optical extinction due to the dust	71
4.7	Conclusion and Discussion	75
Chapter 5	Prompt Optical Emission Constraints GRB's Emission Site	77
5.1	Introduction	77
5.2	Determining the self-absorption frequency	79
5.3	The one-spectral-component assumption	82
5.4	Deriving R constraints from ν_a and SED	84
5.5	GRB data sample	89
5.6	Results	91
5.6.1	The dependence of results on Γ and B	93
5.6.2	Comparison with results from an alternative modelling approach . .	99
5.7	Conclusion and Discussions	100
5.7.1	Multi-color information for the low-energy spectrum	101
5.7.2	Limitations of the method	102

Chapter 6 Late Jet in GRBs	104
6.1 Introduction: late jet and a multi-component GRB stellar explosion	104
6.2 Late jet - SN ejecta interaction	106
6.2.1 The cavity in the SN ejecta	109
6.2.2 Late jet - SN ejecta crossing	109
6.2.3 Thermal emission from the late cocoon break out	110
6.3 Late jet - cocoon interaction	113
6.3.1 Cocoon geometry and dynamics	113
6.3.2 Cavity in the cocoon	114
6.3.3 The jet - cocoon interaction phases	117
6.3.4 The emission from the late jet - cocoon interaction	120
6.3.5 Light curves	123
6.3.6 Results	129
6.4 Observational implication and detection prospects	134
6.4.1 The Late jet - SN ejecta interaction	134
6.4.2 Late jet - cocoon interaction	135
6.5 Summary	137
Chapter 7 Conclusions	141
Appendices	143
Bibliography	154
Vita	168

Chapter 1

Introduction

1.1 History

Gamma-ray bursts (GRBs) were first known as the short, intense flashes of gamma-rays (a few $\times 10$ keV to $\gtrsim 100$ MeV) from the space. It was first discovered in 1960's by Vela, a US satellite that was designed to monitor other countries' compliance to a nuclear bomb banning treaty (Klebesadel et al. 1973). Early GRB research was hindered by two facts. First, observing in gamma-rays tends to have poor angular resolution. Second, both in time and in position over the sky GRBs happen randomly, and they last very shortly (typically a few tens seconds). Both facts make it hard for follow-up observations. Therefore in the following two decades, still little was known about the origin and mechanism of GRBs. Lacking the critical information about distances, people don't know whether GRBs are galactic, extragalactic or cosmological events. Thus, there were many GRB models then, spanning from neutron stars to supermassive black holes. Absorption features at 20 keV and 40 keV in GRB spectrum once were detected by GINGA, and were interpreted as electron's cyclotron absorption lines, corresponding to a magnetic field strength $\sim 10^{12}$ G that is comparable to typical neutron star surface field strength (Fenimore et al. 1988; Murakami et al. 1988). This was considered then as a major evidence for the galactic neutron star origin of GRBs.

One corner stone of GRB research came after the Compton Gamma-Ray Observatory (CGRO) was launched. Its onboard all-sky γ -ray instrument, BATSE, detected about 2700

bursts in 9-year CGRO mission. Statistics showed that the GRB distribution over the sky is isotropic, which strongly suggested a cosmological origin (Meegan et al. 1992). The discovery of GRB 970228's X-ray afterglow by Beppo-SAX was the second corner stone of GRB research (Costa et al. 1997). Afterglow is the rapidly dimming emission that is detected in longer-wavelength bands and from the burst site after the γ -rays have died off. To be distinctive, people frequently call the γ -rays in bursts the “prompt emission”. X-ray observation can achieve positioning accuracy $\sim 1'$, which enables follow-up observing of afterglows in long wavelengths and eventually leads to the identification of host galaxies and their red shifts ($z = 0.695$ for GRB 970228; Bloom et al. 2001). Since then, the cosmological origin of GRBs was confirmed.

1.2 Observed behaviors

1.2.1 Prompt emission

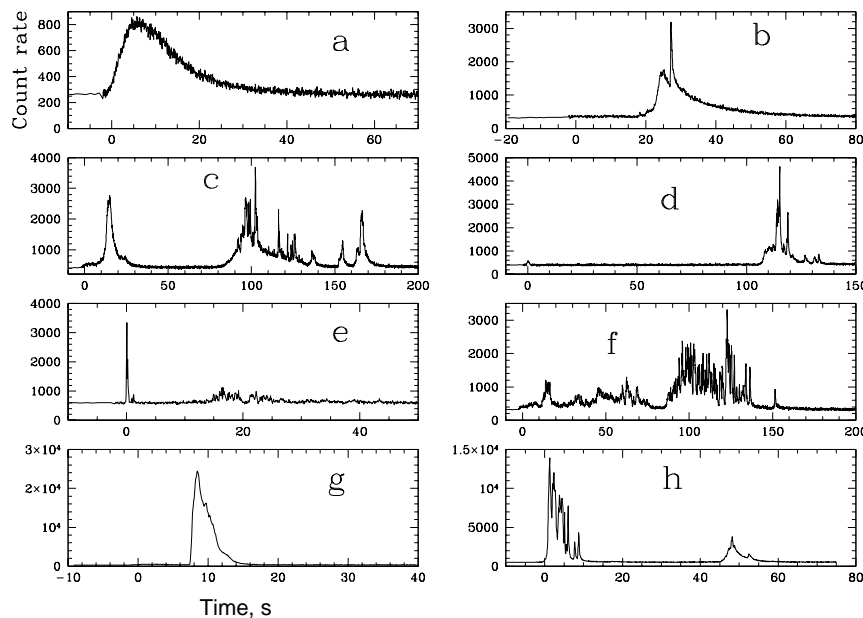


Figure 1.1: Examples of GRB prompt emission light curves (LCs) in 25 – \gtrsim 300 keV energy band. Each panel corresponds to a burst. From Stern et al. (1999). All examples shown here belong to the long GRB class. There is evidence that complex variability structure also appears in some short GRB LCs (Nakar 2007).

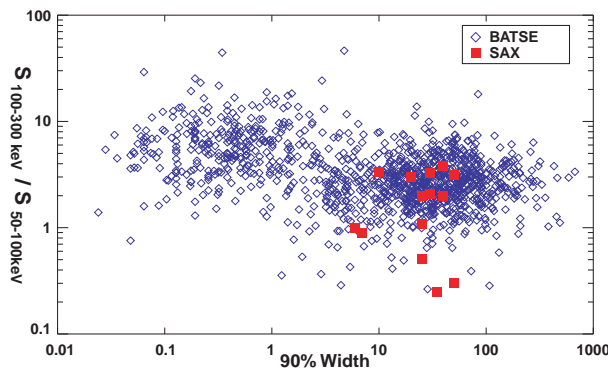


Figure 1.2: The distribution of durations and hardness ratios for GRBs in the BATSE 4B Catalog, plotted together with a few BeppoSAX bursts. The duration is represented by T_{90} , length of the time window over which 90% of the total γ -ray photon counts are received. The spectral hardness is defined as the ratio of total photon count fluxes recorded in two neighboring energy bands. The distribution clearly shows a bi-modality: short (< 2 s), hard bursts vs. long (> 2 s), soft bursts. From Kulkarni et al. (2000).

Typical burst light curves (LCs) are highly variable and erratic (see Figure 1.1). It is composed of individual pulses (or peaks). There is no general trend of pulse width's evolution with time within a burst (Ramirez-Ruiz & Fenimore 2000). A pulse usually shows spectral hardening during its rising phase (e.g., Lu et al. 2010). Typical shortest variability time scale is ~ 0.1 s¹, implying a compact stationary source with size $\lesssim 10^9$ cm. A typical observed fluence is $\sim 10^{-6}$ erg cm⁻²; for a cosmological event of $z = 2$, that corresponds to an isotropically released energy of $\sim 10^{52}$ erg (i.e., 1% of total solar rest mass energy!), or a luminosity of $\sim 10^{51}$ erg s⁻¹. This extremely high energy budget could be alleviated by noting the possibility that the source is narrowly beamed toward the observer. If $\theta_j \ll 1$ is the source opening angle, the beaming-corrected energy release would be smaller than the isotropically equivalent value by a factor of $1/\theta_j^2$.

The spectrum of the burst usually can be described by two joint power laws (Band et al. 1993). The high energy power law typically has a index β slightly below -1 (β is defined as in $f_\nu \propto \nu^\beta$), and the low energy power law index $\beta \approx 0$. The peak energy of the spectrum is typically around 300 KeV (Preece et al. 2002). The high energy power law does not show clear feature of cut-off up to a few tens of MeV.

GRBs can be phenomenologically classified into two subclasses: long, soft bursts

¹There have been cases for which millisecond variability was identified (Walker et al. 2000).

and short, hard bursts (Kouveliotou et al. 1993; also see Figure 1.2). Recently, newly discovered properties of both long and short bursts prompted some authors to advocate a progenitor-oriented classification scheme (see Zhang et al. 2009).

1.2.2 Afterglow

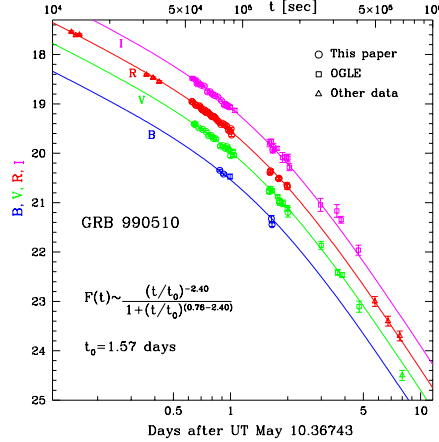


Figure 1.3: An example of a GRB’s IR/optical afterglow LCs. The temporal decay transition at ~ 1 day after the burst is interpreted as the time when deceleration of the relativistic ejecta causes the relativistic-beaming angle ($\sim 1/\Gamma$, where Γ is the ejecta Lorentz factor; Rybicki & Lightman 1979) to exceed the ejecta’s real opening angle so that the ejecta dynamics can not be considered as being spherically symmetric. From Stanek et al. (1999).

The afterglow LCs are usually found to decay in power laws with time (e.g., in Figure 1.3), and their spectra are also in power-law forms such that $f_\nu(t) \propto \nu^\beta t^\alpha$, with $\alpha \sim -1$ and $\beta \sim -1$, but both α and β are slightly different between in different wave bands (say, optical vs. X-ray).

One feature about afterglow in the post-BeppoSAX era is that some LCs show a temporal slope steepening around days after burst (Figure 1.3). This break can be interpreted as when the edge of a beamed ejecta starts to be visible due to the deceleration of a relativistic ejecta that produces the burst and the afterglow (Kulkarni et al. 1999; Mészáros & Rees 1999). In fact, this feature has long been anticipated by the GRB models involve relativistic, beamed jet (next section). Thus, this break not only confirms the relativistic motion but also alleviates the high energy budget for GRB.

1.3 Relativistic fireball model

Relativistic motion of the GRB source is required to circumvent the so-called “compactness problem”, which is explained as follows. Let us consider an individual pulse of the prompt emission whose isotropic equivalent energy release is $E_{iso} \sim 10^{50}$ erg and variability time scale is $\delta t \sim 10^{-1}$ s. It immediately implies a compact region ($\lesssim 10^9$ cm) containing an enormous amount of energy, colloquially dubbed “fireball”, in which the photon field energy density is so high that the optical depth for $\gamma + \gamma \longrightarrow e^+ + e^-$ is huge:

$$\tau_{\gamma\gamma} = f_p \frac{E_{iso} \sigma_T}{E_p (c \delta t)^2} \sim 10^{12}, \quad (1.1)$$

where $E_p \sim 300$ keV is the characteristic observed photon energy, σ_T is the Thompson cross section and f_p represents the fraction of the photon pairs with energies that satisfy $\sqrt{E_1 E_2} > m_e c^2$. This is inconsistent with the observations because the prompt emission spectrum does not show a high-energy cut-off due to photon annihilation up to 10 - 100 MeV (Kaneko et al. 2008). The way around this inconsistency is to require the source to be relativistically moving toward the observer with a Lorentz factor Γ . In that case, the comoving size of the source is estimated as $\sim \Gamma^2 c \delta t$, and the photon energy in the source rest frame is de-boosted to $\sim E_p / \Gamma$. Since $f_p \propto E_p^{\beta+2}$ where β is the high energy power law index of the emission spectrum, the optical depth will be lowered by a factor of Γ^5 . Therefor the requirement of $\tau_{\gamma\gamma} < 1$ implies $\Gamma > 10^{2.4}$.

The internal-shock model is the most popular model describing the prompt emission; it postulates that non-uniformity in the Lorentz factor history of the outflow causes collisions between faster and slower parts of the outflow when they have moved to a larger distance (e.g., Rees & Mészáros 1994; Paczynski & Xu 1994). The resultant energy dissipation heats and accelerates charged leptons to highly relativistic energies in order for them to radiate the prompt emission. The work presented in Chapter 2 is dealing with one specific particle acceleration mechanism – diffusive shock acceleration. Also, Chapter 3 discusses an natural outcome of the internal-shock model and attempts to apply it to explain a newly discovered feature in afterglows. Challenging issues with this model have been pointed out (e.g., Kumar & McMahon 2008) and various versions of a relativistic mini-emitter model

have been discussed (Lyutikov & Blandford 2003; Kumar & Narayan 2009; Lazar et al. 2009).

The interpretation of the afterglow in the post-BeppoSAX era by the external-shock model (Rees & Mészáros 1992; Mészáros & Rees 1993) has been largely successful. Based on this model, the fast moving ejecta that carries kinetic energy of $\gtrsim 10^{51-52}$ erg will sweep and shock-heat the circumburst medium, whose relativistic charged leptons emit the radiation as the afterglow. Once the collected medium amounts to be comparable to the initial rest mass of the ejecta, the latter starts to decelerate, and this time marks the start of the dimming of afterglow.

Emission mechanism is an essential part in constructing successful model for GRBs and afterglows. The most promising one are the synchrotron and / or synchrotron self inverse-Compton (SSC) emission (e.g., Sari et al. 1998; Kumar & McMahon 2008; also see Piran 1999, 2005 and Mészáros 2002 for extensive reviews). Some alternatives include photosphere emission (Mészáros & Rees 2000; Rees & Mészáros 2005; Pe’er et al. 2006; Giannios & Spruit 2007; Ryde & Pe’er 2009) and jitter radiation (Medvedev 2000; Workman et al. 2007; Morsony et al. 2009) but with less observational support. The work presented in Chapter 5 discusses and utilizes a second-order effect in synchrotron radiation — the self absorption.

1.4 Progenitors and central engines

1.4.1 Central engines

Central engine is a colloquial term that refers to whatever at the source produces the GRB relativistic outflow. The most important ingredient of a central engine model is the ability of generating the relativistic jet. The variability constraint points to a stellar mass compact object. Currently two most frequently discussed models are the black hole (BH) accretion disk model and the millisecond proto-magnetar model.

The most gigantic version of BH accretion disk system has long been used to explain the existence of relativistic jets in active galactic nuclei (AGNs) and the high-energy emission detected in blazars, one subclass of AGNs. Therefore, the stellar mass version of the BH

accretion disk system is a natural candidate for GRB central engine. Two categories of mechanisms for launching the jet in this system have been seriously explored, i.e., the neutrino-driven jet (e.g., Narayan et al. 1992; Eichler et al. 1989) and the magnetically driven jet, respectively. In the first category, luminous neutrino flux from the inner disk is deposited near the polar axis region, launching the jet. However, the neutrino flux is very sensitive to the accretion rate, thus, the neutrino-driven jet is too transient and overall efficiency is too low (e.g., Di Matteo et al. 2002). The magnetic category comprises two varied versions. In one version, the so-called BZ mechanism (Blandford & Znajek 1977; Komissarov et al. 2009), the electromagnetic energy of the black hole is directly tapped and transported in the polar direction in the form of e^-e^+ pairs. In another scenario (Lyden-Bell 1996; Lovelace et al. 2002; Uzdenski & MacFadyen 2006), the magnetic field lines threading the disk are twisted by differential rotation to form a magnetic tower, which grows and accelerates in the polar direction and eventually launch the jet.

The alternative central engine model envisages a newly born, rapidly rotating magnetar (spin period $P \sim 1$ ms, surface magnetic field $B \sim 10^{15}$ G; Usov 1992; Duncan & Thompson 1992). Such a proto-magnetar might be produced in a rotating type-Ib/c SN progenitor, accretion-induced collapse of a white dwarf, or the merger of two white dwarfs or two neutron stars. Because the proto-magnetar was born hot ($T \geq 10$ MeV), it launches thermal neutrino-driven hydrodynamic winds via processes $\nu_e n \rightarrow pe^-$ and $\bar{\nu}_e p \rightarrow ne^+$. As the magnetar cools on time scale ~ 20 s, the wind becomes increasingly magneto-centrifugally dominated with the magnetization parameter σ approaches $\sim 10^2$. Once the wind undergoes the acceleration phase in which magnetic energy is transformed into kinetic energy, it eventually could attain a Lorentz factor $\Gamma \sim \sigma$ (Bucciantini et al. 2006; Thompson et al. 2006; Metzger et al. 2007). Bucciantini et al. (2008) showed that beaming of the jet can be obtained in the context of type Ib/c SN progenitor where the stellar envelope material acts to collimate the wind into the polar direction.

1.4.2 Progenitors of long bursts

Observational clues to long GRBs' progenitors come from two aspects: (1) GRBs are found to be in actively star forming galaxies (e.g., Christensen et al. 2004, Castro Cerón et al.

2006) or in star (especially massive ones) forming regions of the host galaxies (e.g., Paczyński 1998; Bloom et al. 2002; Fruchter et al. 2006); (2) for a subset of nearly a dozen of GRBs, X-ray-rich GRBs and X-ray flashes, supernova (SN) features – both temporally and spacially associated with the bursts (Woosley & Bloom 2006 for a review) – were detected. For four of those: GRB 980425 (e.g., Galama et al. 1998), 030329 (e.g., Hjorth et al. 2003), 021211 (Della Valle et al. 2003) and 031203 (e.g., Malesani et al. 2004), the physically associated SNe were not only photometrically but also spectroscopically confirmed. The others of the subset show a late-time (~ 10 days) SN-like “bump” in the optical afterglows, with a simultaneous strong color evolution, e.g., in GRB 980326 (Bloom et al. 1999) and 011121 (Bloom et al. 2002), consistent with the hypothesis of an underlying SN. All these point to the massive star origin for long GRBs, especially some explosive event that marks the catastrophic deaths of the stars.

The class of models that have the BH accretion disk as the central engine and the massive star ($\sim 10 - 30M_{\odot}$) as the progenitor are generally dubbed “collapsar” model. In this scenario, BH forms as the end product of the core collapse at the end of the star’s thermonuclear life. The formation of a disk requires a minimum specific angular momentum $j_{\min} \approx 3 \times 10^{16} (M_{BH}/3M_{\odot}) \text{ cm}^2 \text{ s}^{-1}$ for the accreted stellar material. This implies a fast rotating progenitor.

The typical duration of the prompt burst ($T_{90} \sim 10$ s, in host rest frame) bears some implication about the size of the progenitor, independent of the nature of central engine: the time spent by the jet traversing the progenitor stellar envelope should not be long compared with the T_{90} . The jet traversing speed is about $0.1c$ (Ramirez-Ruiz et al. 2002; Matzner 2003; see also Shen et al. 2010). This sets an approximate upper limit of the size of the progenitor, $R_* \leq 10^{11}$ cm. The compact carbon-oxygen or helium Wolf-Rayet stars (progenitors for type Ib/c SNe) are the most likely candidates.

1.4.3 Progenitors of short bursts

The phenomenology of the host galaxies for short GRBs shows distinctive properties from the hosts of long GRBs. The hosts for shorts include both early- (elliptical) and late-type (spiral) galaxies, as well as field and cluster galaxies (Nakar 2007 and references therein).

Table 1.1: Host galaxy properties for long and short GRBs, respectively (Nakar 2007 and references therein).

	Long GRBs	Short GRBs
Host type	dwarf spiral starbursts	various types; spiral and elliptical
Specific star formation rate	$\approx 10M_{\odot} \text{ yr}^{-1}(L/L_{*})^{-1}$	$\leq 1M_{\odot} \text{ yr}^{-1}(L/L_{*})^{-1}$
SN association	yes (at least for some)	no
Field or cluster galaxy	field galaxy	both

This is in contrast to the long-GRB hosts who are typically late-types and in the field (see Table 1.1). In average, the short GRB hosts show less star formation activity. No associated SN has been detected for short GRBs despite their systematically low red shifts. These support the distinct natures of long and short GRBs.

The merger of a compact binary (neutron star + BH or neutron star + neutron star) has long been discussed as the potential short GRB progenitor (e.g., Eichler et al. 1989; Narayan et al. 1992). The binary merge as a result of energy and angular momentum loss due to gravitational-wave radiation. A BH accretion disk system can form after the merger with a disk mass of $0.01 - 0.3M_{\odot}$. The life time of the disk is $\sim 0.1 - 1$ s, much shorter than in the collapsar scenario, therefore making it a natural candidate for the short GRB progenitor. A number of analytical (Popham et al. 1999; Narayan et al. 2001; Di Matteo et al. 2002) and simulation (Lee & Ramirez-Ruiz 2002; Rosswog & Davis 2002, Rosswog & Liebendörfer 2003; Rosswog et al. 2003) work have investigated the evolution of the disk in this picture. The jet launching mechanism is expected to not differ in nature from in the collapsar scenario.

1.5 Recent development

1.5.1 *Swift*'s new discoveries

Thanks to its unprecedented rapid slewing capability, the *Swift* satellite was able to catch the X-ray afterglow right after the prompt emission dies off. Shortly after its launch, it has recently unveiled a “canonical” behavior pattern in about two-thirds of GRBs’ early X-ray

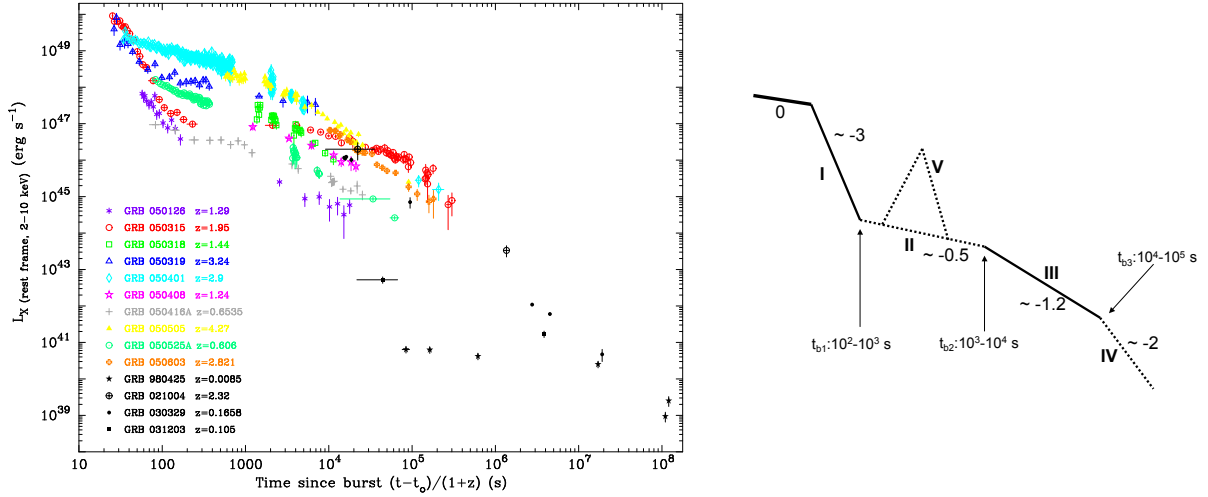


Figure 1.4: *Left*: X-ray afterglow LCs for a sample of *Swift* GRBs with established redshifts (colored; as in 2006), plotted together with selected pre-*Swift* events (black). From Nousek et al. (2006). *Right*: Schematic view of the “canonical” X-ray afterglow LC revealed by *Swift*. The phases or components are: I – steep decay; II – plateau; III – normal decay; IV – post-jet-break decay; V – flares. Also marked are the temporal decay indices of various phases. From Zhang et al. (2006).

afterglows (Nousek et al. 2006; O’Brien et al. 2006): a rapid decline phase lasting for $\sim 10^2$ s is followed by a shallow decay phase lasting $\sim 10^3 - 10^4$ s, then by a “normal” power-law decay and finally by a possible jet break. The “normal” decay phase is reminiscent of the power-law decay seen in the pre-*Swift* era. A number of exemplar LCs and a schematic diagram are shown in Figure 1.4.

In addition, X-ray flares are found in about 50% of all *Swift* bursts; they have been discovered in all of the above phases (Burrows et al. 2005, 2007; Chincarini et al. 2007)². X-ray flares are observed at a few $\times 10^2 - 10^3$ s (as late as $10^4 - 10^5$ s in some cases) after the burst, with a fluence typically about one tenth of the fluence of the prompt γ -rays; in one case, GRB 050502B, this ratio is ~ 1 (Falcone et al. 2007). Figure 1.5 shows four early *Swift* events with flares. Flares are characterized by a large flux increase and by a very steep rise and decay. Typical increase of the flux ranges from a factor of order unity to 10 and in some rare cases even a few hundred. The decay after the flare peak is as steep as $\propto t^{-4}$, much steeper than the underlying afterglow decay ($\propto t^{-1}$). The pulse width to the peak time ratio $\Delta t/t$ is much smaller than unity, typically ~ 0.3 . Strikingly, late flares are

²Even long before *Swift*, a late X-ray flare was detected by BeppoSAX for GRB 970508 (Piro et al. 1998).

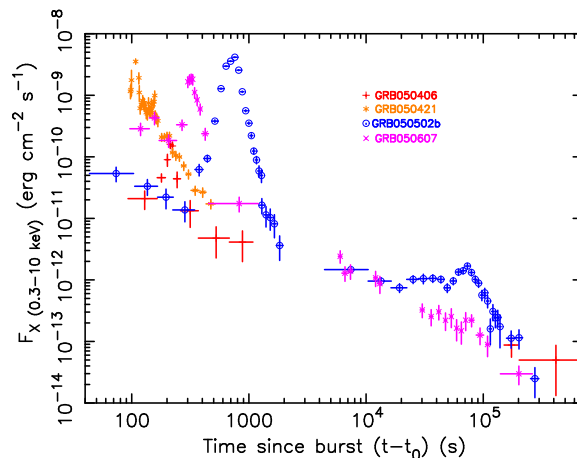


Figure 1.5: X-ray afterglow LCs for a few selected GRBs with X-ray flares. From Nousek et al. (2006).

also found in short bursts (Barthelmy et al. 2005; Campana et al. 2006b).

1.5.2 Interpretations

The “normal” decay at late times is the canonical afterglow component due to the interaction of the decelerated GRB ejecta with the circumburst medium, i.e., the forward shock model. The steep decline is generally interpreted to have the same origin as the prompt γ -ray emission; specifically, it is the prompt photons that are emitted from the larger observing angle region of the ejecta and hence arrive to the observer at a delayed time (e.g., Kumar & Panaitescu 2000; Liang et al. 2006; Zhang et al. 2009). Following this interpretation, Lazzati & Begelman (2005) constrain the radius of the last emitting ejecta to $R \gtrsim \sim 10^{14}$ cm. However, Barniol Duran & Kumar (2009) suggest a major fraction of the steep declines are directly from a continued, rapidly declining, activity of the central engine. Indeed, an early, rapid declining accretion phase is found in collapsar simulation (Linder et al. 2010).

The intervening shallow decay, sometimes called the ‘plateau’, is the most puzzling feature of the X-ray LC. The most straightforward interpretation is a late steady energy injection into the external shock, where the latter is produced by the decelerated early ejecta plunging into the medium. The late energy injection could be due to a new ejecta from the late activity of the central engine (e.g., Dai & Lu 1998a,b; Zhang & Mészáros 2001; Dai 2004;

Yu & Dai 2007), or due to a slow trailing part of the outflow catching up with the already forward-shock-decelerated early part of the outflow when the outflow has a spread in its Lorentz factor distribution (e.g., Granot & Kumar 2006). If it is the first scenario, then this interpretation implies a steady, late activity of the central engine – lasting as long as a day – which poses a challenge to the models of the central engine. Moreover, according to the energy-injection interpretation, the plateau-to-normal transition in the LC corresponds to the cessation of the energy injection, thus the transition should be achromatic. But in about 1/3 of the X-ray plateau GRBs with optical afterglow observations, the optical LC does not show a simultaneous plateau-to-normal break, while in another smaller fraction of the plateau cases, the plateau-to-normal breaks in optical and X-ray are indeed simultaneous (Panaitescu 2007). In most cases the power-law decay following the plateau is consistent with the predictions (the closure relationships) of the forward shock model, which in turn is consistent with the energy injection interpretation.

There is a long list of alternative models for the plateau phase, such as a slow energy transfer from the ejecta to the ambient medium (Kobayashi & Zhang 2007), a two-component jet model (e.g., Granot et al. 2006), a varying shock microphysical parameter model (e.g., Panaitescu et al. 2006), and a reverse shock dominated afterglow model (Uhm & Beloborodov 2007; Genet et al. 2007), etc. (see Zhang 2007 for a review), but none of them satisfy all the observational constraints.

Shao & Dai (2007) suggested an attractive interpretation of the X-ray plateau: dust is likely to exist in the vicinity of the GRB site since it is in a star forming region; X-ray photons from the GRB and its afterglow can be scattered in small angles by dust grains, and those scattered photons arrive to the observer with a time delay, thus can manifest as the plateau component. However, we show in Chapter 4 that this model is ruled out for most cases with plateaus because one intrinsic feature of this model is inconsistent with data.

The late X-ray flares is the most intriguing discovery made by *Swift*. They cannot be due to external-origin mechanisms such as, a density clump in the circumburst medium, or the energy injection into the afterglow blastwave by the trailing slower shells, because the decay slope after the rebrightening from these mechanisms always follows the standard

afterglow model, and $\Delta t/t \sim 1$ is always expected (Nakar et al. 2003; Nakar & Granot 2007; Lazzati & Perna 2007). They are also unlikely to arise from late collisions between two slow moving shells ejected at same time as the main γ -ray producing shells, since the resultant internal shock is too weak to give rise to the significant emission observed in flares (Zhang 2006). The most likely possibility for X-ray flares is the late activity of the central engine (e.g., Fan & Wei 2005). Such a late activity was proposed already in 1998 as an alternative origin of GRB afterglow (Katz & Piran 1998; Katz et al. 1998).

The scenario involving the late engine activity can easily satisfy the constraint that $\Delta t/t \ll 1$. Also in this scenario the late flare is physically separate from the “background” afterglow, so the large amplitude increase of the flux superposed on the decaying afterglow can be naturally explained. Chapter 6 will address some observational consequences of the late jet.

1.5.3 Implications for central engines and progenitors

Both the X-ray flares and the plateaus, especially the former, seem to point to the late activities of the central engine, either in continuous (for the plateau and/or steep decay) or intermittent (for flares) form. Proposed scenarios of extended central engine activities include: relativistic electromagnetic wind from a newly born millisecond magnetar due to spin-down (Dai & Lu 1998a, b; Zhang & Mészáros 2001; Yu & Dai 2007); continuous accretion of the entire progenitor star (Kumar et al. 2008a, b); fall-back accretion of the bound material ejected during a SN, like the ones studied earlier by Chevalier (1989) and MacFadyen et al. (2001); late accretion of ejected material orbiting in eccentric orbits in the compact binary merger (e.g., Faber et al. 2006; Rosswog 2007; the latter found late accretion luminosity $\sim 10^{45}$ erg s $^{-1}$ at 1 hr after merger).

Lazzati et al. (2008) found that the mean flux of a flare declines with its occurrence time as $\sim t^{-1.5}$. Recently updated analysis shows a slightly steeper slope (Margutti et al. 2010). If a constant conversion efficiency from accretion luminosity to jet luminosity and in turn to radiation luminosity is assumed, this long-term decay slope bears interesting constraint on the extended central engine activity.

In relative to the controversy in interpreting the plateau phase, the implication from

the flares in particular is clear: somehow the central engine has to restart at times of minutes to hours after the prompt, active phase. Some proposed scenarios are: fragmentation of the core during the collapse and subsequent merger of the fragments with a central compact object (King et al. 2005); fragmentation of the accretion disk (Perna et al. 2006); interior field wind-up and subsequent reconnection in the millisecond magnetar (Dai et al. 2006); the off-on switch in accretion rate caused by some magnetic braking barrier mechanism operating at the inner boundary of the disk (Proga & Zhang 2006); glitches in the angular momentum profile of the progenitor star (Perna & MacFadyen 2010); fall-back of eccentrically ejected material in binary merger scenario (Rosswog 2007; Lee & Ramirez-Ruiz 2007).

The new “canonical” behavior and late flares discovered by *Swift* provides exciting opportunities to improve our understanding of GRB origins. For instance, the long-term X-ray afterglow behavior may carry clues to progenitor properties such as size, density, angular momentum and/or composition profiles (e.g., Kumar et al. 2008a; Cui et al. 2010; Perna & MacFadyen 2010). Flares are believed to originate from late central engine ejecta, with the dissipation and radiation mechanism probably resembling the one responsible for the prompt emission. Physical properties of the ejecta that produces flares, such as magnetization and radius, still wait to be explored. Also worthwhile is to study the forward-shock signature of the late flare-producing ejecta. The abounding multi-band (IR, optical and X-ray) data make those tasks accomplishable in the near future. Undoubtedly, understanding the flare origin may forge a path to understanding the enigma of prompt emission origin.

Chapter 2

Non-Universality for Electrons’ Power-Law Index p

2.1 Introduction

GRBs are observed to have non-thermal spectra during its prompt emission phase (Band et al. 1993). It is widely believed that the synchrotron radiation and/or the inverse Compton scattering are the likely emission mechanism(s) for GRB’s prompt hard X-ray and γ ray emission. The electrons accounting for these emissions are thought to be accelerated in relativistic shocks in GRBs. According to the shock diffusive acceleration model, particles are accelerated when they repeatedly cross a shock front, and the competition between the particle’s energy gain and escape probability per shock crossing cycle leads to a power-law spectrum for the particles:

$$N(\gamma)d\gamma \propto \gamma^{-p}d\gamma , \quad (2.1)$$

where γ is the Lorentz factor of the particle (e.g., Blandford & Ostriker 1978). For non-relativistic shocks, the value of p depends on the the compression ratio of the flow stream across the shock; while in relativistic or ultra-relativistic shocks, which is most likely the case in GRBs, analytical and numerical studies show that p has an “universal” value, $\approx 2.2 - 2.3$ (Kirk et al. 2000, Achterberg et al. 2001, Bednarz & Ostrowski 1998, Lemonine & Pelletier 2003).

In this chapter we investigate the “universality” of the power-law index p for GRBs, which we calculate directly from the high-energy (0.1 – 2 MeV) photon spectrum of GRBs (Preece et al. 1998, 2000), assuming the spectrum is from synchrotron or synchrotron self-inverse-Compton emission of the power-law distributed highly relativistic electrons, using the relations between p and the spectral index, β , of the high-energy power-law photon spectrum.

In §2.2, we describe the GRB spectral data set used and the process of determining the parent p -distribution. In §2.3, we examine the contributions from the spectral fit procedure and the time averaging effect to the dispersion of the parent distribution of p . The p -distributions derived from BeppoSAX GRBs and from HETE-2 (High Energy Transient Explorer) GRBs, X-ray flashes and X-ray rich GRBs are presented in §2.4. We determine the p -distributions for X-ray afterglows in §2.5 and for blazars and pulsar wind nebulae in §2.6. A summary and discussions are given in §2.7.

2.2 The distribution of p in GRBs

2.2.1 The GRB spectral sample

For our analysis, we use the BASTE GRB Spectral Catalog presented by Preece et al. (2000). In the catalog, the time sequences of spectral fit parameters for 156 bright bursts are presented, using mostly the high energy and time resolution data from the Large Area Detectors (LAD), which covers an energy range of typically 28 - 1800 keV. All bursts have at least 8 spectra in excess of 45 σ above background. The spectral models used in fit are (i) ‘Band’ function; (ii) Comptonized spectral model (a power-law with an exponential cut-off); (iii) Broken Power-Law model; and (iv) Smoothly Broken Power-Law model. The ‘Band’ function, the one used most frequently, is an empirical function (Band et al. 1993)

$$N(E) = A \begin{cases} (E/100)^\alpha \exp[-E(2 + \alpha)/E_{peak}], & E < \frac{\alpha - \beta}{2 + \alpha} E_{peak} \\ \left[\frac{(\alpha - \beta) E_{peak}}{100(2 + \alpha)} \right]^{\alpha - \beta} \exp(\beta - \alpha)(E/100)^\beta, & E \geq \frac{\alpha - \beta}{2 + \alpha} E_{peak} \end{cases}$$

where $N(E)$ is the photon counts, A is the amplitude, α is the low-energy spectral index, β the high-energy spectral index, and E_{peak} is the peak energy in the νF_ν spectrum (when

$\beta < -2$).

Since we are here caring about the high-energy power-law portion of the GRB spectra, and also because one possible source of systematic error in the spectral parameter determination arises in selecting different spectral models for different bursts (Preece et al. 2002), only the spectral parameters of those 'Band' function fitted spectra are selected for our analysis.

One of our major concerns is to select the sample of spectra for which β is reliably determined. The BATSE burst signal-to-noise ratio decreases at higher energies as a result of lower photon flux and the decreased detector efficiency. In particular, β may not be well determined if E_{peak} is close to the higher limit of the LAD energy range, E_{max} (≈ 2 MeV) (Preece et al. 1998), thus we must choose those spectra with E_{peak} much lower than E_{max} . Therefore, we select the spectrum for which $100 \text{ keV} < E_{peak} < 200 \text{ keV}$ and the error in β is less than $0.1 |\beta|$. This gives a total sample of 395 spectra for 78 bursts.

2.2.2 Distribution of p and its narrowing

For electrons' distribution given by a power-law:

$$N(\gamma_e) \propto \gamma_e^{-p}, \text{ for } \gamma_e > \gamma_{min}, \quad (2.2)$$

the emergent high energy synchrotron spectrum is asymptotically a power law function: $F_\nu \propto \nu^{-(p-1)/2}$ for $\nu_m < \nu < \nu_c$ ("slow cooling" regime) and $\propto \nu^{-p/2}$ for $\nu > \nu_c$ ("fast cooling" regime), where $\nu_m = \nu_{syn}(\gamma_{min})$ is the synchrotron injection frequency, and $\nu_c = \nu_{syn}(\gamma_c)$ is the synchrotron cooling frequency above which the synchrotron energy loss becomes important.

The spectral index, p , of shock accelerated electrons is associated with the high-energy power-law photon index, β , of GRB photon spectrum, by either $\beta = -p/2 - 1$ ("fast cooling" regime) or $\beta = -(p+1)/2$ ("slow cooling" regime) depending on relative positions of ν_m and ν_c and on which portion of the spectrum is detected. There is one regime, $\nu_c < \nu < \nu_m$, in which $\beta = -3/2$, independent on p . This case can be ruled out by discarding those spectra with $\beta \geq -3/2$ from our sample. We found only one with

$\beta \geq -3/2$ in the BATSE sample of 395 spectra and discarded it.

Piran (2004) argues that the fast cooling must take place during the GRB prompt phase and the reasons are: (i) the relativistic shocks must radiate their energy efficiently, to avoid a serious inefficiency problem; (ii) the electrons must cool rapidly in order that the fast variability could be observed. But there is no firm evidence to date that could rule out the slow cooling case for the GRB itself, since it is difficult to measure the values of γ_c and γ_{min} for a specific burst. Thus in our analysis, we assume that each GRB spectrum above E_{peak} could be in either slow cooling or fast cooling regime, so as to minimize the width of p distribution.

First we plot distribution of p by assuming all spectra are in fast cooling regime. Then we make the distribution narrower by relaxing this constraint. Basically the narrowing process is to move some left-hand part of the distribution to the right by adding 1 to p and assuming this part of sample are in slow cooling regime, since there is a difference of 1 about p value between the two regimes. The algorithm used is described below.

Several algorithms are implemented to get the narrowest distribution. In the most straightforward one, each spectra has the freedom of calculating p from β either in “fast cooling” or “slow cooling” regime, so the number of possible distributions is 2^N for a sample of N spectra. The distribution having the smallest standard deviation is chosen as the narrowest one. This algorithm works well only for $N < 20$ because of the computer running time. For $N > 20$, we divide the overall range of the sample’s β distribution into 20 equal-width bins and treat the spectra with β located in each bin indistinguishably. Then we apply the first algorithm to the 20 bins. In an alternative algorithm, we start with the histogram of p calculated in the “fast cooling” regime and mark a demarcation line within and close to the lower limit of the range of p . Then all p at left to the line in the histogram are moved to right by adding 1 to p , and the new histogram’s standard deviation is calculated. This is repeated after shifting the demarcation line rightward by a step of 0.01 on the p -axis. Finally the smallest standard deviation, hence the narrowest distribution, is found. It turns out that both algorithms give the same results for most of the samples presented in this work. For one sample where minor difference exists between two algorithms’ results, we use the narrower one.

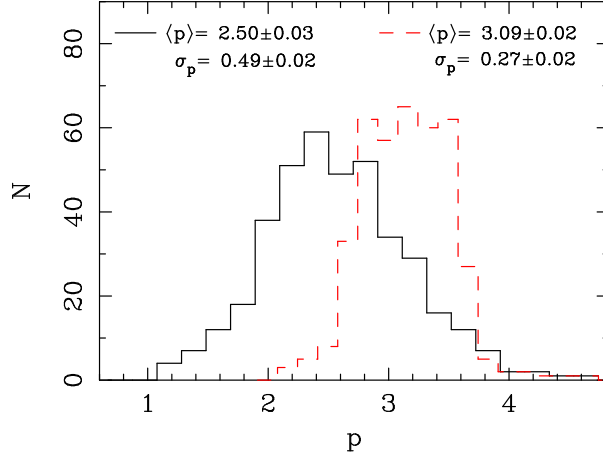


Figure 2.1: Distributions of p for a sample of 394 GRB spectra with $100 < E_{peak} < 200$ keV. *Solid* line: using the relation $p = -2\beta - 2$. *Dashed* line: after narrowing the distribution by using the relation of either $p = -2\beta - 2$ or $p = -2\beta - 1$.

We show the results of the analysis for BATSE bursts in Figure 2.1. Note that all the errors presented in this chapter are at 1σ level. The parent distribution of p for BATSE bursts has a width of 0.54 at a 14σ confidence level. The method that estimates the mean and the width of the parent distribution of p is described below. Note that the mean value of p is ≈ 3 , substantially larger than that for the distribution before the minimization, which is an artifact of choosing some of the spectra to be in the “slow cooling” regime, equivalent to moving the left part of the histograms in the upper panels rightward, in order to minimize the width of the distribution.

2.2.3 Statistical description of the narrowness of p ’s distribution

The observed distribution of p plotted in Figure 2.1 is a convolution of the measurement error distribution and the true distribution (or parent distribution) of p . What we want to know is the true distribution of p . We use the maximum likelihood method to estimate the true p -distribution. Let us say the true distribution of p is Gaussian,

$$P(p) = \frac{1}{\sqrt{2\pi}\sigma_p} \exp\left[-\frac{1}{2} \frac{(p - \bar{p})^2}{\sigma_p^2}\right]. \quad (2.3)$$

Further, we assume the measurement errors have Gaussian distributions too. Then the probability distribution for any one measurement (p_i, σ_i) is the convolution of two Gaussians,

which is the Gaussian

$$P(p_i, \sigma_i, \bar{p}, \sigma_p) = \frac{1}{\sqrt{2\pi}(\sigma_p^2 + \sigma_i^2)^{1/2}} \exp\left[-\frac{1}{2} \frac{(p_i - \bar{p})^2}{\sigma_p^2 + \sigma_i^2}\right]. \quad (2.4)$$

The likelihood function for the set of n measurements p_i, σ_i is

$$L = \prod_{i=1}^n \frac{1}{\sqrt{2\pi}(\sigma_p^2 + \sigma_i^2)^{1/2}} \exp\left[-\frac{1}{2} \frac{(p_i - \bar{p})^2}{\sigma_p^2 + \sigma_i^2}\right]. \quad (2.5)$$

The principle of the Maximum Likelihood Estimate is that, the best estimates of \bar{p} and σ_p^2 are the ones that maximize L . Take

$$l = \ln L = -\frac{1}{2} \sum_i^n \frac{(p_i - \bar{p})^2}{\sigma_p^2 + \sigma_i^2} - \frac{1}{2} \sum_i^n \ln(\sigma_p^2 + \sigma_i^2), \quad (2.6)$$

then the maximum occurs when the following equations

$$\left. \frac{\partial l}{\partial \bar{p}} \right|_{\hat{\bar{p}}, \hat{\sigma}_p^2} = 0, \quad (2.7)$$

$$\left. \frac{\partial l}{\partial (\sigma_p^2)} \right|_{\hat{\bar{p}}, \hat{\sigma}_p^2} = 0 \quad (2.8)$$

have their solution at $\bar{p} = \hat{\bar{p}}$ and $\sigma_p^2 = \hat{\sigma}_p^2$, where “ \wedge ” symbolizes the best estimation of the parameters. If we assume that the distribution of $\hat{\bar{p}}$ and $\hat{\sigma}_p^2$ are both Gaussian, then one can show that the variances of $\hat{\bar{p}}$ and $\hat{\sigma}_p^2$ are

$$\sigma_{\hat{\bar{p}}}^2 = - \left[\left. \frac{\partial^2 l}{\partial \bar{p}^2} \right|_{\hat{\bar{p}}, \hat{\sigma}_p^2} \right]^{-1}, \quad (2.9)$$

$$\sigma_{\hat{\sigma}_p^2}^2 = - \left[\left. \frac{\partial^2 l}{\partial (\sigma_p^2)^2} \right|_{\hat{\bar{p}}, \hat{\sigma}_p^2} \right]^{-1}, \quad (2.10)$$

respectively. So the best estimate of the parameters of true distribution of p are obtained by numerically solving equations (7) and (8), and their associated errors are calculated through equations (9) and (10).

2.3 Systematic errors in β

2.3.1 The ‘Band’ function fit to the spectra

Preece et al. (2000) carried out a Band function fit to GRB spectra observed by BATSE, and this way determined the high energy power-law index (β) and the random error in β due to error in the observed spectral energy distribution. There is also a systematic error in β resulting from the finite bandwidth of the BATSE detector, which was not reported in Preece et al., and we estimate it here. The purpose of this exercise is to estimate the contribution of this systematic error, and its dependence on the peak of the spectrum (E_{peak}), to the dispersion in the p -distribution.

The systematic error arises because the synchrotron spectrum does not make a sharp transition from one power-law index to another when one crosses a characteristic frequency. In particular, the steepening of the spectrum to $\nu^{-p/2}$ above the synchrotron and cooling frequencies does not occur suddenly at E_{peak} , but instead the spectrum approaches this theoretical value asymptotically at $E \gg E_{peak}$.

Since the spectrum is observed in a finite energy range, the measured spectral index will always be somewhat smaller than the true asymptotic value by an amount that depends on the ratio of E_{max} and E_{peak} (E_{max} is the highest energy photon that the detector is sensitive to). The larger the E_{max}/E_{peak} is the smaller the systematic error in β would be, and this dependence on E_{peak} causes some broadening of the observed β distribution.

To estimate this systematic error we generate synthetic spectra with different values for E_{peak} , and carry out a Band function fit to the synthetic spectra to determine β and its deviation from the true asymptotic value.

The synthetic synchrotron spectra is calculated for a relativistic homogeneous shell. The electron distribution function behind the shock is taken to be a single power-law function: $N(\gamma_e) \propto \gamma_e^{-p}$, for $\gamma > \gamma_{min}$, where $m_e c^2 \gamma_{min}$ is the minimum electron energy after they cross the shock front. The magnetic field in the shell is taken to be uniform and the energy density of the field is some fraction (ϵ_B) of the thermal energy density of the shocked fluid; γ_{min} and ϵ_B are chosen so that the peak of the spectrum, E_{peak} , is at some desired value. As electrons move down-stream from the shock front they cool via the synchrotron

and inverse-Compton processes, and their distribution function is modified. We calculate the effect of this cooling on electron distribution functions using a self consistent scheme described in Panaitescu & Mészáros (2000) and McMahon et al. (2006).

The synchrotron spectrum, for a given electron distribution, in the shell comoving frame is calculated as described in detail by Sari et al. (1998) (also see section 2.2). The spectrum in the observer frame is calculated by integrating the spectral emissivity in the comoving frame over the equal-arrival-time surface as described in Kumar & Panaitescu (2000). Errors are then added to this spectrum in a way that mimics the real GRB spectrum.

The synthetic spectrum for a known p is fitted to the Band function in a finite energy range corresponding to the BATSE energy coverage. By varying E_{peak} of the generated spectra we determine the discrepancy between fitted value and “true” value of β as a function of E_{max}/E_{peak} . The results are shown in Figure 2.2. We find the fit always gives a smaller β (in absolute value) than the true asymptotic value and that the “observed” β does indeed depend on E_{max} . The error in β is about 10% when E_{max}/E_{peak} is order unity, whereas the error is $\sim 5\%$ when $E_{max}/E_{peak} \sim 20$. The error also depends on the p value as shown in Figure 2.2; for E_{peak} located between 100 keV to 200 keV, $E_{max} = 1.8$ MeV, and $p = 2.5$, the contribution of this systematic error to the dispersion in β is less than 1.3% – the corresponding contribution to the dispersion in p is $\sigma_p < 0.03$.

We have also carried out a similar calculation for the synchrotron self- inverse-Compton (SSC) spectrum for a population of synchrotron electrons. The incident photons are the synchrotron photons due to the same population of electrons that contribute to inverse-Compton scatterings. The synchrotron radiation is taken to be homogeneous and isotropic in the shell comoving frame, and its spectrum is calculated as described above. The overall SSC spectrum is obtained by the convolution of the synchrotron spectrum and electron energy distribution using equation (7.28 a) in Rybicki & Lightman (1979). The curvature in the SSC spectrum is due to the convolution of the incident spectrum and the electron distribution, and we find that the asymptotic value for the SSC power-law index is reached when $E_{max}/E_{peak} \sim 100$. For this reason we find that for the SSC case, the systematic error in β is $\sim 13\%$ for the typical E_{max}/E_{peak} in BATSE bursts. The dispersion in p caused by E_{peak} being distributed between $E_{peak} = 100$ keV to $E_{peak} = 200$

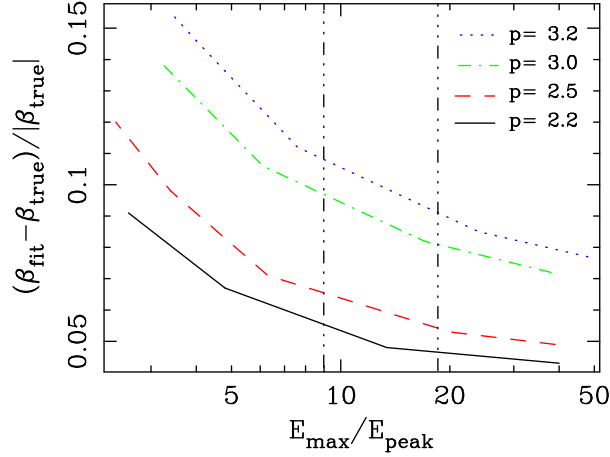


Figure 2.2: The discrepancy between the fitted value and the ‘true’ value of β , as a function of the higher end of the fitting energy range for the synchrotron spectra fitted by the ‘Band’ function. Two vertical lines mark the range of E_{max}/E_{peak} corresponding to the E_{peak} range of the sample in Figure 2.1. The errors of the spectrum data are assumed to be proportional to square root of photon counts: $\sigma(N(\nu)) \propto \sqrt{N(\nu)}$.

keV is, however, small – $\sigma_p < 0.04$.

These results show that the discrepancy between the fitted value and the “true” value of β is small and dependent on E_{max}/E_{peak} , but its dependence on E_{max}/E_{peak} is too small to account for the observed dispersion in the p distribution.

2.3.2 Time-averaging effect

Another source of systematic error in β is the time-averaging of multiple spectra undergoing spectral evolution, i. e., E_{peak} evolving with flux (Ford et al. 1995, Crider et al. 1999). The flux-weighted time-averaging of multiple ‘Band’ spectra may distort the intrinsic high-energy power law.

To examine this effect, we select BATSE time-resolved spectra with E_{peak} in 100 - 200 keV and in 200 - 300 keV, respectively, divide them into non-evolving groups and evolving groups, and analyze their p distributions separately. The results are shown in Table 2.1 We find the evolving spectra groups tend to have flatter p or β , which may be an outcome of the time-averaging effect. But the widths of p distributions for two groups are consistent with each other, showing that the time-averaging does not contribute to observed dispersion in p in Figure 2.1.

Table 2.1: Parameters of parent distribution of p for BATSE GRB spectra samples with E_{peak} -evolution ($\Delta E_{peak} > 15\% E_{peak}$) and without E_{peak} -evolution ($\Delta E_{peak} < 15\% E_{peak}$), where ΔE_{peak} is the E_{peak} difference between any two *adjacent-in-time* spectra. All spectra are assumed in “fast cooling” regime.

Spectra samples	$100 < E_{peak} < 200$ keV		$200 < E_{peak} < 300$ keV	
	Non-evolving	Evolving	Non-evolving	Evolving
$\langle p \rangle$	2.86 ± 0.06	2.38 ± 0.03	2.50 ± 0.07	2.14 ± 0.03
$\sigma(p)$	0.44 ± 0.04	0.47 ± 0.03	0.58 ± 0.06	0.42 ± 0.03

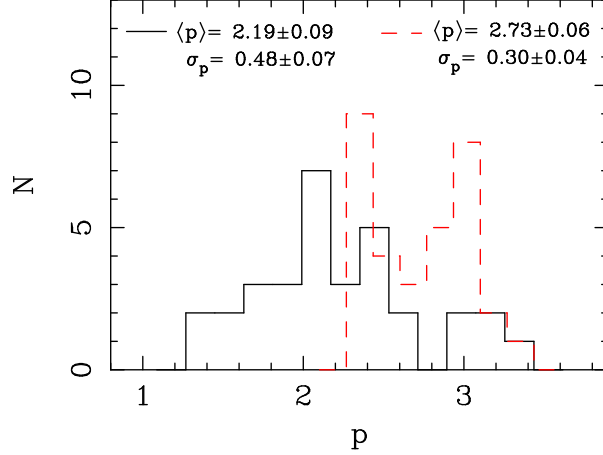


Figure 2.3: The distribution of p determined from 32 time-integrated GRB spectra. *Solid* line: p is inferred from the high-energy power-law index β by the relation $p = -2\beta - 2$. *Dashed* line: the narrowest distribution of p using the relation either $p = -2\beta - 2$ or $p = -2\beta - 1$. β is taken from the ‘Band’-function fit by Band et al. (1993) to the time-integrated spectrum for each burst.

The time-averaging effect is further examined when we use an early BATSE spectral catalog by Band et al. (1993) in which the time-integrated spectrum of each burst is fitted with the ‘Band’ function. We restrict our samples to those with $E_{peak} \leq 300$ keV, and error in β less than $0.1 |\beta|$, which gives a sample of 32 spectra from the catalog of 54 GRBs. The p distribution is shown in Figure 2.3. Comparing with Fig 2.1, one can see that it has approximately the same σ_p as that for the time-resolved GRB spectra. This supports that the time-averaging effect has no impact on the observed dispersion in p .

2.4 p -distributions for BeppoSAX GRBs and HETE-2 XRFs, XRR GRBs and GRBs

We also analyzed a sample of 11 GRBs observed by BeppoSAX. The combined (2 - 700 keV) Wide Field Cameras (WFC) and Gamma-Ray Burst Monitor (GRBM) spectra for these bursts are fitted with the ‘Band’ function by Amati et al. (2002). The narrowest distribution of p for this sample is shown in Figure 2.4 left panel. It has the same estimated mean value of p as in the BATSE bursts, and the width of the parent distribution for p is consistent with that for the BATSE bursts. The larger errors in $\langle p \rangle$ and σ_p are due to the smaller size of the BeppoSAX sample.

Sakamoto et al. (2005) present a catalog of X-ray flashes (XRFs), X-ray-rich (XRR) GRBs and GRBs observed by HETE-2 WXM (Wide Field Camera) (2 - 25 keV) and FREGATE (French Gamma Telescope) (7- 400 keV) instruments. Among 45 bursts in the catalog, 16 bursts have measured high-energy power-law photon index, β , which is obtained through the spectral fit with the ‘Band’ function or a single power-law model. For those XRF spectra fitted by a single power law, it is found that $\beta < -2$. Sakamoto et al. (2005) explain this as that we are observing the high-energy power-law portion of their “Band”-function spectra. Two GRBs (GRB 020813 and 030519) for which “Band” model is used have E_{peak} lying near or above the upper limit of FREGATE energy range, so we exclude them here. We also exclude XRF 030528 which has a large error in β . The final HETE-2 sample we considered comprises 7 XRFs, 4 XRRs and 2 GRBs. The p distribution is shown in Figure 2.4 right panel.

2.5 p -distribution for X-ray afterglows

We also determine the distribution of p during the X-ray afterglows. We use a catalog of X-ray afterglows observed by BeppoSAX compiled by De Pasquale et al. (2006) and a catalog of X-ray afterglows observed by Swift (O’Brien et al. 2006). In De Pasquale et al. (2006)’s catalog, 15 X-ray afterglow spectra are fitted with a Galactic-and-extragalactic absorbed single power law. We use 14 out of them for our analysis and exclude GRB 000210 which has an extremely large error in measured β . In O’Brien et al. (2006)’s Swift catalog of 40

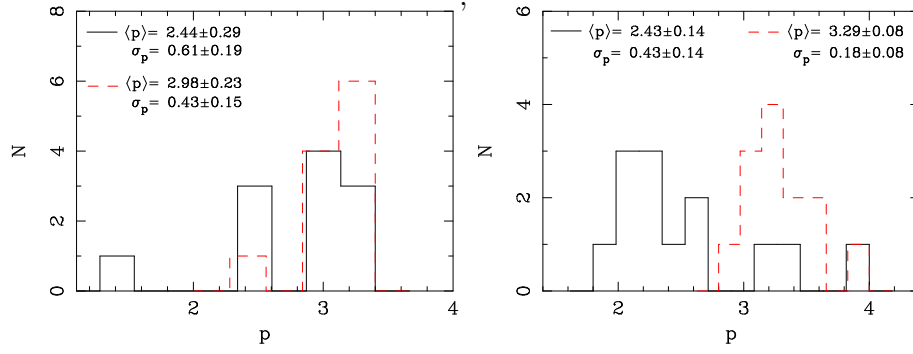


Figure 2.4: *Left*: The distributions of p for 11 GRBs observed by BeppoSAX (Amati et al. 2002); *Right*: The distributions of p for 13 X-ray flashes, X-ray-rich GRBs and GRBs observed by HETE-2 (Sakamoto et al. 2005). *Solid lines*: p is inferred from the higher-energy photon index β by the relation $p = -2\beta - 2$. *Dashed lines*: the narrowest distributions of p using the relation either $p = -2\beta - 2$ or $p = -2\beta - 1$.

X-ray afterglows, we select samples with small errors, $\sigma(\beta_i) < 0.1|\beta_i|$, and discard a sample with extremely large $|\beta|$ ($= 5.5$). We also discard 4 samples with $\beta_i \geq -3/2$ because these β values indicate the X-ray band probably lies between ν_c and ν_m ($\nu_c < \nu_X < \nu_m$), where the asymptotic spectral index is $\beta = -3/2$ and carries no information about p . This gives 28 samples from the catalog.

The p -distributions for the two afterglow samples are shown in Figure 2.5. For the BeppoSAX afterglows, the narrowest distribution is consistent with a δ -function distribution within 1σ errors; for the Swift afterglows, it is not. The smaller estimated width of the parent p -distribution for BeppoSAX afterglows, we suspect, is due to larger errors in photon indices β_i of the BeppoSAX sample, $\langle \sigma_i(\beta) \rangle = 0.26$, than the Swift sample which has $\langle \sigma_i(\beta) \rangle = 0.10$.

2.6 Distribution of p in Blazars and pulsar wind nebulae

2.6.1 Blazars

Blazars are active galactic nuclei with the relativistic jet pointed toward us. The nonthermal spectra of blazars are due to synchrotron or/and inverse Compton emission of relativistic electrons accelerated by shocks within the jet (Blandford & Königl 1979, Sikora et al. 1994).

Donato et al. (2005) present a spectral catalog of six years of BeppoSAX observa-

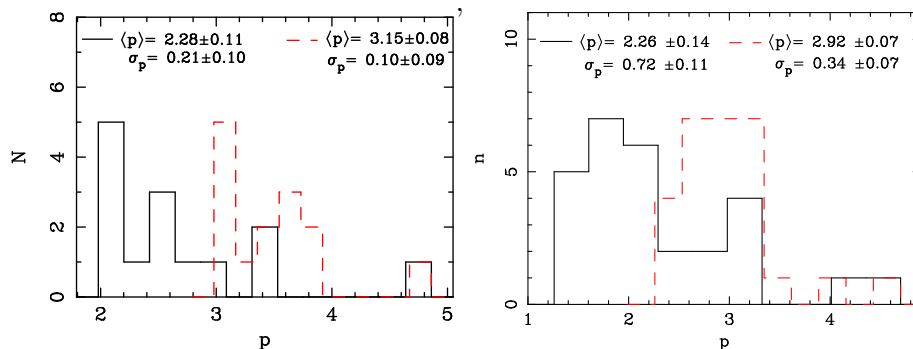


Figure 2.5: The distributions of p for GRB X-ray afterglows. *Left*: 14 afterglows are observed by BeppoSAX, taken from De Pasquale (2006). *Right*: 28 afterglows are observed by Swift, taken from O’Brien et al. (2006). *Solid* lines: p is inferred from the photon index β by the relation $p = -2\beta - 2$. *Dashed* lines: the narrowest distribution of p using the relation either $p = -2\beta - 2$ or $p = -2\beta - 1$.

tions of Blazars at 0.1 - 50 keV. This catalog comprises three classes of blazars, namely low-luminosity sources (High-energy peaked BL Lacs, or HBLs), mid-luminosity sources (Low-energy peaked BL Lacs, or LBLs) and high-luminosity sources (Flat Spectrum Radio Quasars, or FSRQs). The three classes have different locations of synchrotron peak. X-rays from HBLs are likely to be above the peak of synchrotron spectrum, thus have steep X-ray spectra ($\beta < -2$), while FSRQs and LBLs in X-ray band have more contribution from inverse Compton component and thus have flatter spectra.

From this catalog we use 44 spectra of 33 HBLs (some sources have multi-epoch spectra) that are best fitted by single power-laws. The errors of fitted photon indices reported in Donato et al. (2005) are at 90% confidence level which we convert to $1-\sigma$ errors. The distribution of p derived from their photon spectral indices is shown in Figure 2.6. We find that the distribution of p for blazars is not consistent with a δ -function distribution: $\sigma_p = 0.22 \pm 0.03$ after the narrowing.

2.6.2 Pulsar wind nebulae

Power-law nonthermal spectra are also often observed in pulsar wind nebulae (PWNs) of rotation-powered pulsars. The nebular emission is the synchrotron radiation from charged particles heated by the termination shock in relativistic outflow (winds) from the pulsar (see Arons 2002 for a review). Gotthelf (2003) presents a catalog of nine bright Crab-like

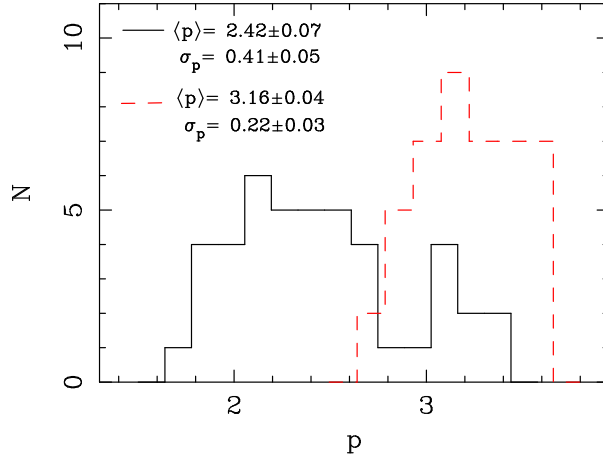


Figure 2.6: The distribution of p for 44 X-ray spectra of 33 blazars. *Solid* line: p is inferred from the photon index β by the relation $p = -2\beta - 2$. *Dashed* line: the narrowest distribution of p using the relation either $p = -2\beta - 2$ or $p = -2\beta - 1$. β is taken from the catalog compiled by Donato et al. (2005).

pulsar systems with Chandra observations and the photon indices of pulsar nebulae, β_{PWN} , and their 90% confidence errors are provided. We derive the distribution of p from β_{PWN} with the β_{PWN} errors converted into 1σ errors and find that $\sigma_p = 0.59 \pm 0.15$, $\langle p \rangle = 1.72 \pm 0.20$ assuming the X-ray band is in the fast cooling regime. After narrowing, the narrowest distribution has $\sigma_p = 0.24 \pm 0.07$, $\langle p \rangle = 2.04 \pm 0.09$.

2.7 Summary and Discussions

Motivated by theoretical calculations and numerical simulations showing that the shock-accelerated electrons in relativistic shocks have a power-law distribution with an universal index $p \simeq 2.2 - 2.3$, we have determined the values of p from γ -ray and X-ray spectra for a number of relativistic sources such as GRBs (prompt emissions and afterglows), blazars and pulsar wind nebulae.

The maximum likelihood estimate of the width of the parent distribution for GRB prompt emission is found to be quite broad, $\sigma_p = 0.51 \pm 0.02$; the probability that the distribution is consistent with a δ -function is extremely small, and therefore this result does not support that there is an universal p .

We have considered the systematic errors in photon index due to spectra fit and

time averaging of spectra and their contributions to the scatter in p distribution. We have shown that those contributions are very small for GRBs and can not explain the scatter in p distribution.

For X-ray afterglows of GRBs, the p -distribution of the BeppoSAX sample can not rule out a possibility that the parent distribution is a δ -function distribution; however, a larger sample of Swift afterglows is inconsistent with a δ -function parent distribution. We point out that the smaller width of parent distribution for the BeppoSAX sample is due to its larger measurement error in β .

Analysis of 44 blazar spectra and 9 pulsar wind nebulae shows that the distributions of p for blazars and pulsar wind nebulae (PWNe) are also broad, not consistent with a δ -function distribution.

Possible situations in which the “universality” of p could break are: (i) The shock is mildly relativistic (cf. Kirk et al. 2000); (ii) The magnetic field is oblique to the shock normal (Baring 2006); (iii) The nature and strength of the downstream magnetic turbulence are varying (Ostrowski & Bednarz 2002, Niemiec & Ostrowski 2004). A non-Fermi acceleration in a collisionless plasma shock was studied by Hededal et al. (2004), in which electrons are accelerated and decelerated instantaneously and locally, by the electric and magnetic fields of the current channels formed through the Weibel two-stream instability. It is not known whether an “universality” of p could hold for this mechanism. The “universality” of p might not happen in non-shock accelerations; for instance, in an alternative model for GRBs (Lyutikov & Blandford 2003), the energy is carried outward via magnetic field or Poynting flux. The particles accounting for the γ -ray emissions are accelerated by magnetic field reconnection which may also produce a power-law spectra of accelerated particles with a variable p (however, this is still poorly understood).

Chapter 3

Scattered Emission from A Relativistic Outflow

3.1 Introduction

Gamma-Ray Bursts (GRBs) are a cosmological phenomenon with a huge energy release, fast variabilities and very complex multi-wavelength light curves. A relativistic outflow is unavoidable in order to explain the fast variability and so called “compactness problem” (see Chapter 1). According to the standard “fireball” model, the outflow from the GRB central engine has a finite duration and can have a wide range in its velocities, thus can be modeled by being made of discrete relativistic shells. These shells are responsible for the observed γ -rays (via internal shocks) and for the afterglow emissions (via external shocks) (cf. Piran 2005). In this picture, if one shell emits γ -rays, some fraction of that emission should be scattered by shells behind, and the scattered emission would arrive at the observer at a different time, with a different flux and possibly at a different photon frequency. Detection of the scattered photons would help us explore the properties of the GRB ejecta and the late outflow.

In this chapter we consider a simple scenario, where only two consecutive shells are present: one shell radiates and the other receives some of this radiation and scatters it. The two shells can have different speeds and the shell that receives and scatters the emission can have an arbitrarily large time delay in its ejection from the central source, but it has

to be behind the emitting shell. An observer detects the primary emission from the first shell and then the scattered emission from the second one at a later time because of the light-travel time. We calculate the ratio between these two emissions' fluxes, the time delay in their arrival, the ratio between their frequencies and the ratio between their durations.

Early GRB X-ray observations by *Swift* have shown a “canonical” behavior that presents a puzzling shallow decay typically lasting for a few hours (e.g. Nousek et al. 2006). This decay phase is poorly understood (see Zhang 2007 for a review of current possible models). We will explore the possibility that this shallower decay could be due to the scattered emission.

The scattering of the GRB prompt emission photons by electrons or dust grains in a dense circum-burst environment has been investigated before (e.g., Esin & Blandford 2000; Madau et al. 2000; Shao & Dai 2007; Heng et al. 2007). The scattering process we consider in this work happens within the GRB outflows, which is a natural outcome of the outflow when it has a finite duration and a variable speed.

We first derive a general formula for the observed flux from a relativistic shell in §3.2. In §3.3 we construct the flux and geometrical relations for a two-shell model. The formulae for the scattering process are developed in §3.4. Then we elaborate the primary and scattered emission relations such as time delay, frequency ratio and time duration ratio in §3.5. We present the main result - the ratio between the scattered and the primary fluxes - in §3.6. The application to the GRB shallower decay data is presented in §3.7. A faster scattering shell case is discussed in §3.8. We also discuss X-ray dim bursts and X-ray-dark short bursts, for which the scattered emission might be easier to detect, in §3.9. Finally, the summary and conclusions are given in §3.10.

3.2 Emission from a relativistic shell

Consider a spherical shell moving relativistically with Lorentz factor (LF) Γ (when the shell is beamed with an opening angle $\geq \Gamma^{-1}$, it still can be considered as being spherical). The surface brightness in the rest frame of the shell is $\epsilon'_{\nu'}$ ($\text{erg s}^{-1} \text{ cm}^{-2} \text{ Hz}^{-1} \text{ sr}^{-1}$), the luminosity distance between the observer and the shell is D_L and the radius of the shell

is R , both of these distances measured in the laboratory frame. The flux density received at a frequency ν by the observer ahead of the shell, f_ν , can be obtained by calculating the specific luminosity of the relativistic shell. The luminosity of the shell is given by $f_\nu(4\pi D_L^2) = \epsilon'_{\nu'}(4\pi R^2)\Gamma(2\pi)$. The last expression includes a factor of Γ , to take into account the “boost” that the photons experience; and a factor of 2π , since we assume that the photons are being emitted isotropically from the shell, in the rest frame of the shell, and we are only interested in the ones reaching the observer. The two expressions yield

$$f_\nu = 2\pi\epsilon'_{\nu'}\Gamma\left(\frac{R}{D_L}\right)^2. \quad (3.1)$$

3.3 Two shells scenario

Consider now two thin shells being ejected with an half opening angle of θ_j from the central engine. Shell 1 is ejected first with LF Γ_1 and, after a delay δt , measured in the laboratory frame, shell 2 is ejected with LF Γ_2 . We assume that shell 1 is emitting photons isotropically in its co-moving frame and is characterized by an angular-independent surface brightness, $\epsilon'_{\nu'}$, on both sides of the shell. In the laboratory frame most of these photons will appear to move in the same direction as shell 1 and reach a distant observer, and a few will move in the opposite direction, encountering shell 2 on their way. These photons will be scattered by shell 2 and then reach the observer. See Figure 3.1 for an illustration. We will use primed quantities to specify the co-moving frame where the quantity is being measured: unprimed corresponds to the laboratory frame, primed ($'$) to the co-moving frame of shell 1, and double primed ($''$) to the co-moving frame of shell 2.

Before proceeding with the detailed calculations about the scattered emission, we provide simple scaling relationships between the observed scattered emission and the observed direct emission from shell 1 by only considering the line-of-sight region.

Let us assume ν is the photon frequency of the direct emission from shell 1. In the shell 1 co-moving frame, the emitted photon frequency is $\nu' \simeq \nu/\Gamma_1$ due to the relativistic Doppler effect (for simplicity we neglect the factor of 2). As seen by shell 2 the photon has a frequency of $\nu'' \simeq \nu'\Gamma_2/\Gamma_1$. If shell 2 is cold, the scattering does not change the photon's

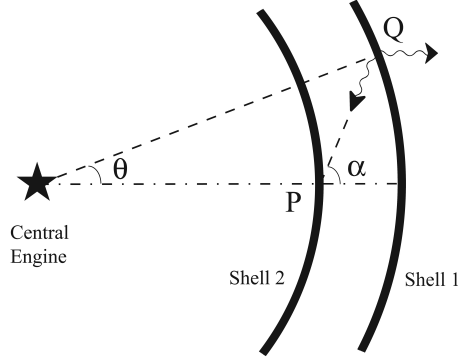


Figure 3.1: A simple two-shell scenario geometry. The diagram shows two photons emitted at the same time from point Q on shell 1. One photon travels to the observer ahead of shell 1, while the other travels back to point P on shell 2. Note that the figure shows shell 1 and the photons at time t and shell 2 at time $t + l$, where l is the light travel time from Q to P .

energy. The observed frequency of the scattered emission is $\nu_s \simeq \nu''\Gamma_2$. Thus the observed frequency ratio between the two emissions is $\nu_s/\nu \simeq (\Gamma_2/\Gamma_1)^2$.

The scattered emission will be observed at a later time, because the scattered photon has traveled an extra distance. This extra distance is equal to $R_1(1 - \beta_2/\beta_1) + \beta_2\delta t$, where R_1 is the distance of shell 1 from the central engine when a photon was emitted from shell 1 toward shell 2, and β_1 and β_2 are shell 1 and shell 2 velocities, respectively (the first part of the expression is due to the difference in the speeds of the shells, and the second part is due to the ejection delay of shell 2). The observed delay of the scattered emission is this separation divided by the speed of light $\approx R_1/(2\Gamma_2^2 c) \approx T(\Gamma_1/\Gamma_2)^2$ for small δt , where T is the observed time of the shell 1 direct emission since the central engine explosion.

If L is the luminosity observed directly from shell 1, the shell 1 co-moving frame luminosity would be $L' \simeq L/\Gamma_1^2$. In the shell 2 co-moving frame, shell 1 has a luminosity of L'' . Using the Lorentz invariance of I_ν/ν^3 we find that the luminosity ratio, L''/L' , is the frequency ratio to the fourth power, or $L''/L' \simeq (\nu''/\nu')^4 \simeq (\Gamma_2/\Gamma_1)^4$. In the shell 2 co-moving frame, $\tau_e L''$ is the luminosity of the scattered emission, where $\tau_e (< 1)$ is the shell 2 electron's optical depth. Then the observed luminosity of the scattered emission is $L_s \simeq \tau_e L'' \Gamma_2^2$. Thus we obtain that $L_s/L \simeq \tau_e (\Gamma_2/\Gamma_1)^6$, which shows that the observed luminosity ratio is strongly dependent on the LF ratio. Since $\nu_s/\nu \simeq (\Gamma_2/\Gamma_1)^2$, this indicates

that the observed specific flux ratio is $f_{\nu,s}^s/f_\nu \simeq \tau_e(\Gamma_2/\Gamma_1)^4$.

3.3.1 Incident flux on shell 2

Now we work on the calculation of the scattered flux on more detail. In order to determine the scattered flux from shell 2 we will first calculate the incident flux from shell 1 at the point of shell 2 that intersects the line of sight between the central engine and the observer - we will call this point P . To do this, we will use the Lorentz invariance of I_ν/ν^3 , where I_ν ($\text{erg s}^{-1} \text{ cm}^{-2} \text{ Hz}^{-1} \text{ sr}^{-1}$) is the specific intensity and ν is the frequency of the photon.

Let us consider a bundle of rays being emitted at an arbitrary point - Q - on shell 1 and directed to the point P (see Figure 3.1). The angle between the line of sight and the line connecting the central engine and Q is θ . The angle between the line of sight and the line connecting P and Q is α . From the Lorentz invariance of I_ν/ν^3 we can obtain the relation

$$\frac{I_\nu}{I''_{\nu''}} = \left[\frac{1}{\Gamma_2(1 + \beta_2 \cos \alpha)} \right]^3, \quad (3.2)$$

where I_ν is the specific intensity of the bundle of rays measured by an observer standing still in the laboratory frame and at the position of point P (note that I_ν is NOT the specific intensity of the emission detected by a distant laboratory-frame observer sitting in front of shell 1); $I''_{\nu''}$ is the specific intensity of the bundle of rays measured in the shell 2 co-moving frame at point P . We can relate I_ν with the specific intensity of the bundle of rays measured in the shell 1 co-moving frame at point Q , $I'_{\nu'}$, as follows

$$\frac{I_\nu}{I'_{\nu'}} = \left\{ \frac{1}{\Gamma_1[1 + \beta_1 \cos(\alpha - \theta)]} \right\}^3. \quad (3.3)$$

We need to obtain a relation between the co-moving specific intensity, $I'_{\nu'}$, and the surface brightness, $\epsilon'_{\nu'}$, of shell 1, both quantities in shell 1 co-moving frame. This relation is given by

$$I'_{\nu'} = \frac{\epsilon'_{\nu'}}{\cos \eta'} \quad (3.4)$$

where η' is the angle measured in the shell 1 co-moving frame between the photon's direction and the normal to the emitting surface (facing shell 2). η' can be determined using the

aberration of light formula (Rybicki & Lightman 1979):

$$\cos \eta' = \frac{\cos(\alpha - \theta) + \beta_1}{1 + \beta_1 \cos(\alpha - \theta)} \quad (3.5)$$

where all the quantities have been defined previously.

Finally, using formulas (2) - (5) one can obtain the incident flux from shell 1 on point P in shell 2 co-moving frame, $f''_{\nu''}$, which is given by

$$f''_{\nu''} = \int I''_{\nu''} \cos \alpha'' d\Omega'' = 2\pi \int I''_{\nu''} \cos \alpha'' \sin \alpha'' d\alpha'',$$

or

$$f''_{\nu''} = \pi \epsilon'_{\nu''} \left(\frac{\Gamma_2}{\Gamma_1} \right)^3 \int \frac{(1 + \beta_2 \cos \alpha)^3 d \sin^2 \alpha''}{[\beta_1 + \cos(\alpha - \theta)][1 + \beta_1 \cos(\alpha - \theta)]^2}, \quad (3.6)$$

where the integral runs from 0 to α''_j – the half opening angle of shell 1 as seen from an observer on point P in shell 2 (the subscript “j” denotes the edge of shell 1).

3.3.2 Light path geometry

In order to solve this last integral, we need to understand the relation between the angles and how they transform in different frames. First, we need to setup the geometry of the problem. The photon that is emitted from point Q at time t travels a distance l and reaches point P on shell 2 at time $t + l$ (here, and throughout this chapter, we use units in which the speed of light is 1). The radius at which the photon was emitted from point Q on shell 1 is $R_1(t)$ and reaches point P on shell 2 at radius $R_2(t + l)$, where $R(t)$ can be obtained by $R(t) = \beta t$ (all these quantities are measured in the laboratory frame). It is important to remember that there is a time delay in the ejection of shell 2, which will be taken into account when using $R_2(t)$. The geometry describing the light path of the photon gives:

$$l \cos \alpha = R_1(t) - R_2(t + l) \quad (3.7)$$

$$l \sin \alpha = R_1(t) \sin \theta, \quad (3.8)$$

from which it can be shown that

$$\tan \alpha = \frac{\theta}{1 - \frac{\beta_2}{\beta_1} + \frac{\beta_2 \delta t}{R_1} - \frac{\beta_2 \theta}{\sin \alpha}}, \quad (3.9)$$

where we use R_1 to denote $R_1(t)$ and we have also used the fact that θ is small, so that $\sin \theta \simeq \theta$. And again, using the *aberration of light* formula we have

$$\tan \alpha'' = \frac{\sin \alpha}{\Gamma_2(\cos \alpha + \beta_2)}. \quad (3.10)$$

Also from (9) and (10) we can get a close form expression for α'' :

$$\tan \alpha'' = \frac{\theta}{\Gamma_2(1 - \frac{\beta_2}{\beta_1} + \frac{\beta_2 \delta t}{R_1})}. \quad (3.11)$$

Equations (10) and (11) allow us to carry out the integral in equation (6). Careful analysis (see Appendix A) shows that the integrand is weakly dependent on α'' and it reduces to a constant of order unity. This simplifies $f''_{\nu''}$ greatly and we obtain:

$$f''_{\nu''} = \pi \epsilon'_{\nu''} \left(\frac{\Gamma_2}{\Gamma_1} \right)^3 \int d\sin^2 \alpha'' = \pi \epsilon'_{\nu''} \left(\frac{\Gamma_2}{\Gamma_1} \right)^3 \sin^2 \alpha''_j \quad (3.12)$$

where α''_j can be obtained from equation (11) by setting $\theta = \theta_j$.

3.4 Scattering from shell 2

3.4.1 Scattered flux

Assuming that shell 2 is “cold” and knowing the flux from shell 1 at point P , we can calculate the scattered flux from shell 2. We will assume that the photons from shell 1 undergo *Thomson scattering* with the electrons on shell 2 and that the scattering is isotropic in the co-moving frame. The surface brightness of shell 2 in its co-moving frame will be given by

$$\epsilon''_{\nu''} = \frac{1}{4\pi} \Sigma_e \sigma_T f''_{\nu''},$$

where Σ_e is the electron surface density and σ_T is the Thomson scattering cross section. To obtain the scattered flux at the scattered frequency that reaches an observer at a luminosity distance D_L one can use equation (1)

$$f_{\nu,s}^s = 2\pi\epsilon''_{\nu''}\Gamma_2\left[\frac{R_2(t_{scat})}{D_L}\right]^2$$

and obtain

$$f_{\nu,s}^s = \frac{1}{2}\tau_e\Gamma_2\left[\frac{R_2(t_{scat})}{D_L}\right]^2 f''_{\nu''} \quad (3.13)$$

where we have $\tau_e = \Sigma_e\sigma_T$, the optical depth for electrons to Thompson scattering. We also have used $R_2(t_{scat})$ to specify that the radius of the second shell needs to be calculated at a later time, t_{scat} , when the scattering occurs¹. Using equation (12) we obtain

$$f_{\nu,s}^s = \frac{\pi}{2}\tau_e\epsilon'_{\nu'}\left(\frac{\Gamma_2^4}{\Gamma_1^3}\right)\left[\frac{R_2(t_{scat})}{D_L}\right]^2 \sin^2 \alpha''_j,$$

which allows us to find a ratio between the scattered flux from shell 2, $f_{\nu,s}^s$, and the direct flux from shell 1, f_ν ,

$$\frac{f_{\nu,s}^s}{f_\nu} = \frac{1}{4}\tau_e \sin^2 \alpha''_j \left[\frac{R_2(t_{scat})}{R_1(t)}\right]^2 \left(\frac{\Gamma_2}{\Gamma_1}\right)^4, \quad (3.14)$$

where we have used equation (1) to immediately get f_ν . It is important to note that these two fluxes arrive at different times. This will be further explained in detail in the next section. Also, the result for $\tau_e > 1$ is the same as that for $\tau_e = 1$.

Recall that before the detailed calculation we estimated the observed specific flux ratio under the line-of-sight approximation. Eq. (14) is consistent to what we estimated earlier, except that the previously ignored shell solid angle term is fully considered here.

¹We approximate the incident flux on point P to the incident flux on any other point on shell 2. The validity of this approximation depends on the magnitude of α''_j . If α''_j is small, the angular size of shell 2 as seen by an observer co-moving with shell 2 at the point where the line of sight intersects with shell 1 - let us call it Λ''_j - is also small, because $\Lambda''_j/\alpha''_j = R_2(t_{scat})/R_1(t) < 1$; then this approximation should be good. For our interested parameter space - determined from the GRB data we are going to use - α''_j is between 0.1 and $\pi/4$ (see §3.7), not very small. Thus the approximation overestimates the scattered flux slightly.

3.4.2 Shell radii

All quantities of the flux ratio are known, except the ratio of the two radii. To obtain it, we will consider a photon emitted on shell 1 that travels along the line of sight to shell 2. The light travel time of this photon is given by equation (7) but using $\alpha = 0$, so that

$$l = R_1(t) - R_2(t + l).$$

Solving for l we obtain

$$l = \frac{R_1(t) - R_2(t)}{1 + \beta_2}. \quad (3.15)$$

The ratio of the radii is given by

$$\frac{R_2(t_{scat})}{R_1(t)} = \frac{\beta_2(t - \delta t + l)}{\beta_1 t},$$

and using equation (15) and the fact that both shells move close to the speed of light, we find

$$\frac{R_2(t_{scat})}{R_1(t)} = \frac{\beta_2}{\beta_1} - \frac{\beta_2 \delta t}{2R_1}. \quad (3.16)$$

With this last equation and equation (11), the flux ratio - given by equation (14) - is fully determined.

3.4.3 Time dependence of scattered emission

For simplicity, let us assume that the emission from shell 1 is constant and time independent: that it is a box function with some finite duration. The time dependence of the scattered emission will be given by: (i) the time evolution of the electrons' optical depth, τ_e , (ii) the opening angle of shell 1 as seen by a co-moving observer on shell 2, α_j'' , and (iii) the radius of shell 2, $R_2(t_{scat})$.

The time dependence of $R_2(t_{scat})$ and α_j'' is weak, provided that the ejection time delay between shells, δt , is small compared to R_1 . This is the case we are interested in,

since if $\delta t \sim R_1$, then δt would be on the order of hours or days. This scenario would invoke a very long lasting activity of the central engine, a scenario that we don't want to address in this chapter. The only time dependence of the scattered emission will be given by the time evolution of τ_e , which goes as $\tau_e \propto R_2^{-2} \propto T^{-2}$.

3.5 Primary and scattered emission relations

3.5.1 Time delay

Let us assume that two photons are emitted from shell 1 at the same time. Photon 1 travels directly to the observer located ahead of shell 1 and arrives at time T_p (p stands for *primary*). Photon 2 travels in the opposite direction, scatters from shell 2 and then travels back to the same observer arriving at a later time T_s (where s stands for *scattered*). What is the time delay, $T_s - T_p$, between the arrival of these two photons?

If we are only interested, as a simplification, in the photons along the line of sight, then this time delay will be given by equation (15). We only need to multiply this expression by 2, to obtain the full time it takes for the photon to travel to shell 2 and then to travel back to shell 1. Then, the time delay is

$$T_s - T_p = 2 \frac{R_1(t) - R_2(t)}{1 + \beta_2}.$$

Further simplification yields

$$T_s - T_p = R_1 \left(1 - \frac{\beta_2}{\beta_1} \right) + \beta_2 \delta t. \quad (3.17)$$

3.5.2 Ratio of frequencies

In this section we will determine the relation between the frequency of a photon emitted from shell 1, ν , and a photon emitted from shell 1 and then scattered by shell 2, ν_s (both quantities measured in the laboratory frame). For this, we will only consider the photons traveling along the direct line of sight between the central engine and the observer.

In the shell 1 co-moving frame, a photon is emitted from shell 1 with frequency ν' .

In the laboratory frame, this frequency is measured as

$$\nu = \nu' \Gamma_1 (1 + \beta_1 \cos \Theta'),$$

where Θ' is the angle between the photon's direction and the x' -axis direction of the shell 1 co-moving frame. Note that the x' -axis of frame K' is always directed to the moving direction of frame K' relative to another inertial frame (K or K''). Since the photon is emitted to the observer ahead of shell 1, $\Theta' = 0$, and the previous equation becomes

$$\nu = \nu' \Gamma_1 (1 + \beta_1). \quad (3.18)$$

Let us now consider a photon emitted in shell 1 and directed to shell 2. The frequency of this photon in the shell 1 co-moving frame is ν' , and in the shell 2 co-moving frame is given by ν'' . They are related by

$$\nu'' = \nu' \Gamma_1'' (1 + \beta_1'' \cos \Theta''),$$

where Γ_1'' (β_1'') is the LF (velocity) of the shell 1 as measured in the shell 2 co-moving frame. These quantities can be expressed in terms of quantities in the laboratory frame as

$$\Gamma_1'' = \Gamma_1 \Gamma_2 (1 - \beta_1 \beta_2), \quad \beta_1'' = \frac{|\beta_1 - \beta_2|}{1 - \beta_1 \beta_2}.$$

If we assume that $\Gamma_1 > \Gamma_2$ (or $\Gamma_1 < \Gamma_2$), in the co-moving frame of shell 2 it will seem that shell 1 is moving away from shell 2 (moving towards shell 2), so that $\Theta'' = \pi$ ($\Theta'' = 0$). Using the last 3 equations, we can determine

$$\nu'' = \nu' \Gamma_1 \Gamma_2 (1 - \beta_1)(1 + \beta_2), \quad (3.19)$$

which holds for both assumptions. The photon will be scattered by shell 2 by Thomson scattering (there will be no frequency change in the co-moving frame of shell 2) and then will travel towards the observer. The scattered frequency can be obtained with

$$\nu_s = \nu'' \Gamma_2 (1 + \beta_2 \cos \Theta'').$$

Setting $\Theta'' \approx 0$, since the photon moves towards the observer, yields

$$\nu_s = \nu'' \Gamma_2 (1 + \beta_2) \quad (3.20)$$

Finally, using equations (18)-(20) the ratio of the scattered frequency to the primary frequency is

$$\frac{\nu_s}{\nu} = \left(\frac{\Gamma_2}{\Gamma_1} \right)^2 \left(\frac{1 + \beta_2}{1 + \beta_1} \right)^2 \approx \left(\frac{\Gamma_2}{\Gamma_1} \right)^2, \quad (3.21)$$

using the fact that both shells travel close to the speed of light. This is consistent with our earlier simple estimation. Therefore, a slower (faster) shell 2 will lower (raise) the frequency of the primary photons.

3.5.3 Ratio of observed durations

Let us assume that shell 1 emits for a finite duration of time, Δt (in the lab frame). An observer located in front of the shell will detect that the radiation from shell 1 lasts for ΔT_p , given by $\Delta T_p = \Delta t(1 - \beta_1)$. The radiation from shell 1 will also travel back to shell 2 and will get scattered, giving a scattered radiation duration of ΔT_s in the observer frame. If the first photon from shell 1 is emitted at time t and the last one at $t + \Delta t$ (in the lab frame), then we can use the time delay equation (17) to find the time delay between the first primary photon and the first scattered photon, and the time delay between the last primary photon and the last scattered photon, respectively. Subtracting these two expressions, we find that

$$\frac{\Delta T_s}{\Delta T_p} = \frac{1 - \beta_2}{1 - \beta_1} \approx \left(\frac{\Gamma_1}{\Gamma_2} \right)^2, \quad (3.22)$$

which means that the observed duration of the scattered emission will be stretched (shortened) by a factor of $(\Gamma_1/\Gamma_2)^2$ for a slower (faster) shell 2.

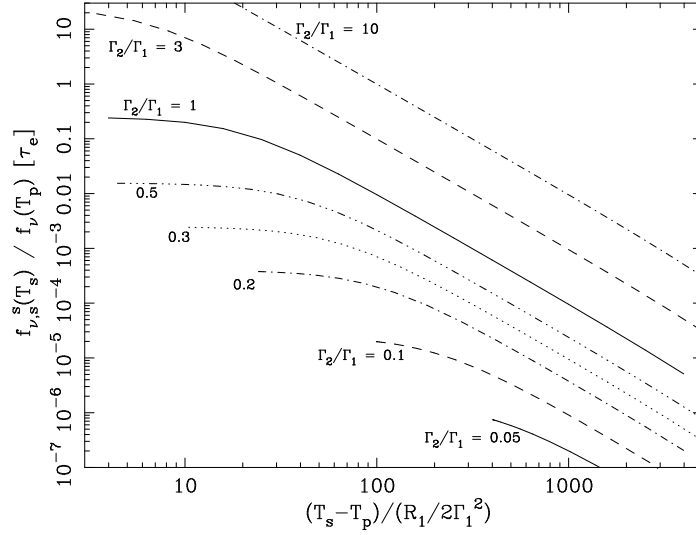


Figure 3.2: The ratio of the flux of the scattered emission to the flux of the primary emission (measured at their respective arrival times and photon energies) as a function of the observed time delay between these two emission components in units of $R_1/(2\Gamma_1^2)$, assuming shell 1 LF $\Gamma_1 = 100$ and shell opening angle $\theta_j = 0.1$. The unknown shell 2 optical depth τ_e is put on the y-axis as an “unit” of the flux density ratio.

3.6 Results

3.6.1 Ratio between scattered and primary fluxes

We want to write equation (14), the ratio of the fluxes, in such a way that we can easily use the available observations to test our theory.

We can use equation (17) to solve for δt , the time delay between the ejection of the two shells. This expression is then substituted into equation (11) to get $\sin^2 \alpha_j''$ and into equation (16) to get the radius ratio. Finally, we obtain the flux ratio in terms of the time delay divided by $R_1/(2\Gamma_1^2)$ as follows:

$$\frac{f_{\nu,s}^s(T_s)}{f_{\nu}(T_p)} = \frac{1}{4}\tau_e \left\{ 1 + \left[\frac{\Gamma_2}{2\Gamma_1^2\theta_j} \frac{(T_s - T_p)}{R_1/2\Gamma_1^2} \right]^2 \right\}^{-1} \left[\frac{1}{2} + \frac{\beta_2}{2\beta_1} - \frac{1}{4\Gamma_1^2} \frac{(T_s - T_p)}{R_1/2\Gamma_1^2} \right]^2 \left(\frac{\Gamma_2}{\Gamma_1} \right)^4. \quad (3.23)$$

We then plot this ratio of two flux densities as a function of the $R_1/(2\Gamma_1^2)$ -normalized time delay (the choice of this normalization will become evident in the next section) for various values of Γ_2/Γ_1 in Figure 3.2. For plotting purposes we assume $\Gamma_1 = 100$ and

$\theta_j = 0.1$. Since the exact value for τ_e is unknown, we choose to scale τ_e into the y-axis of the figure, as an “unit” of the flux density ratio.

Looking at Figure 3.2, we can observe that the theoretical flux ratio curves have two regions (this is very noticeable when $\Gamma_2 < \Gamma_1$). In region I the flux ratio is flat, and in region II the flux ratio is proportional to the square of the inverse of the normalized time delay. If we inspect equation (23), we can separate its two regions by:

$$\frac{f_{\nu,s}^s(T_s)}{f_{\nu}(T_p)} = \begin{cases} \frac{\tau_e}{4} \left(\frac{\Gamma_2}{\Gamma_1} \right)^4 & \text{if } \frac{T_s - T_p}{R_1/2\Gamma_1^2} \leq \frac{2\Gamma_1^2\theta_j}{\Gamma_2} \quad (\text{Region I}) \\ \tau_e \Gamma_2^2 \theta_j^2 \left(\frac{T_s - T_p}{R_1/2\Gamma_1^2} \right)^{-2} & \text{if } \frac{T_s - T_p}{R_1/2\Gamma_1^2} > \frac{2\Gamma_1^2\theta_j}{\Gamma_2} \quad (\text{Region II}) \end{cases}$$

These two regions will be used in our applications section. For now, they just provide a simpler theoretical model. Notice that the $\Gamma_2 > \Gamma_1$ curves are dominated by region II, while the $\Gamma_2 < \Gamma_1$ curves have a combination of both regions. For the latter, the maximum scattered flux is given by region I.

These results show that the scattered flux from a slower shell is small, falls at a lower energy than the primary photon’s energy and its total duration is larger than that of the primary emission. If we have a faster shell, then the scattered flux from it could be either larger or smaller than the primary flux, depending on its ejection time delay, δt . If δt is larger (smaller) than the total observed duration of the primary emission, then the scattered emission would appear at late times (would be part of the primary emission). In any case, the energy of the scattered photons would be larger than that of the primary ones, and the total duration of the scattered emission would be smaller than that of the primary emission, so that the scattered emission would appear as a short bright flash.

3.6.2 Hot shell 2

In the last sections we assumed *Thomson scattering*, but we should also look at the possibility that shell 2 could be hot, so the scattering mechanism at work would be *inverse Compton*. Shell 2 electrons could be hot in the following scenario. Consider that shell 2 is ejected after shell 1 and undergoes particle heating, by either internal shocks or magnetic dissipation, at a radius smaller than the radius where shell 1 produces γ -ray photons. Shell

2 would experience adiabatic expansion and would cool, but the electrons could still be hot by the time that the γ -ray photons from shell 1 reach them. The shell 2 electrons might also cool via radiation, but the chances still exist that the radiative cooling is very inefficient, for instance, when the radiation mechanism is synchrotron-self-inverse-Compton instead of pure synchrotron for the same observed typical photon energy, so that the electron cooling time could be comparable to the delay between the electron heating and the scattering.

The main difference in the formulas previously derived will be in the ratio of the frequencies of the primary and the scattered emission. Equation (21) is modified to include the inverse Compton boost to the photon energy:

$$\frac{\nu_s}{\nu} = \left(\frac{\Gamma_2}{\Gamma_1}\right)^2 \gamma_e^2, \quad (3.24)$$

where γ_e is the electrons' thermal Lorentz factor. The theoretical flux density ratio previously derived will not be changed in this new scenario.

Let us now calculate the isotropically equivalent total energy in the shell 2 hot electrons. For this, we need to calculate the isotropically equivalent total number of electrons in the shell from their optical depth

$$N_e = 4\pi R_2^2 \frac{\tau_e}{\sigma_T}.$$

In the present scattering scenario, we have $R_2 \approx R_1$ (we'll prove this in section §3.7). R_1 can be estimated from the γ -ray variability time scale: $R_1/(2\Gamma_1^2)$ (explained in detail in §3.7). Then the total energy in the hot electrons of shell 2 is given by

$$E_e = N_e m_e c^2 \Gamma_2 \gamma_e = 16\pi \left(\frac{\Gamma_2}{\Gamma_1}\right) \Gamma_1^5 \gamma_e m_e c^4 \left(\frac{R_1}{2\Gamma_1^2 c}\right)^2 \frac{\tau_e}{\sigma_T}, \quad (3.25)$$

where c is the speed of light.

Table 1: . Our sample of 10 GRBs which show clearly an X-ray shallower decay component and the relevant data. Basic data are from O'Brien et al. (2006).

GRB	050315	050319	050713A	050713B	050714B	050803	050814	050819	050822	050915B
F_{BAT}^a										
$(10^{-8} \text{ erg cm}^{-2} \text{ s}^{-1})$	3.2	0.5	3.8	3.2	1.1	2.4	1.2	0.9	2.5	8.6
β_{BAT}^b	1.2	1	0.6	0.5	2	0.5	1	1.6	1.5	1
$F_{\nu=100\text{keV}}(T_{90})^c$										
$(10 \mu\text{Jy})$	4	0.8	12	6	0.6	4.8	2	1	3.2	16
$F_{\nu=10\text{keV}}(T_{90})^d$										
$(10 \mu\text{Jy})$	63	8	48	19	60	15	20	40	101	160
T_{90}^e										
(s)	96	150	130	130	50	90	144	36	105	40
$\frac{R_1}{2\Gamma_1^2}^f$										
(s)	30	40	20	130	50	90	144	36	30	40
t_{end}^g										
(10^4 s)	1	3.2	1	4	5	2	≥ 6	2	1.3	5
$F_{XRT}(t_{end})^h$										
$(10^{-11} \text{ erg cm}^{-2} \text{ s}^{-1})$	0.8	0.8	1.2	1	0.5	1	≤ 0.05	0.04	0.7	0.09
β_X^i	1.5	2	1.3	0.7	4.5	0.7	1.1	1.2	1.6	1.5
$F_{\nu=1\text{keV}}(t_{end})^j$										
(μJy)	1.2	1.1	2.4	1	0.16	1	≤ 0.06	0.04	1.2	0.1
$\frac{t_{end}}{R_1/(2\Gamma_1^2)}^k$	330	800	500	308	1000	222	≥ 417	556	433	1250
$\frac{F_{\nu=1\text{keV}}(t_{end})}{F_{\nu=100\text{keV}}(T_{90})}$	0.03	0.137	0.02	0.017	0.026	0.021	≤ 0.003	0.004	0.037	0.0006
$\frac{F_{\nu=1\text{keV}}(t_{end})}{F_{\nu=10\text{keV}}(T_{90})}$	0.0019	0.0138	0.005	0.0052	0.0003	0.0066	≤ 0.0003	0.0001	0.0012	0.00006

^aMean BAT flux.

^bBAT spectral index.

^cBAT flux density at 100 keV at the end of the γ -ray emission.

^dBAT flux density at 10 keV at the end of the γ -ray emission.

^eDuration of the γ -ray emission.

^fSimply T_{90} for those bursts with one smooth or two overlapped pulses; for those “spiky” bursts, i.e., those with multiple, separated pulses, we use the duration of the last pulse.

^gEnding time of the X-ray shallow decay.

^hXRT flux at the end of the shallow decay.

ⁱXRT spectral index.

^jXRT flux density at 1 keV at the end of the shallow decay.

^kObserved time delay between the primary and the scattered emissions in units of $R_1/(2\Gamma_1^2)$. See §3.7.

3.7 Application to the shallow decay component in GRB early X-ray afterglows

In this section we compare the γ -ray burst and X-ray afterglow data with the results of the last section to find out if the shallow decay in X-ray “canonical” afterglow light curves can be due to the scattered emission from the shell(s) following the γ -ray shell. We first consider simply the Thomson scattering mechanism, then we turn to consider the inverse Compton scattering where the electrons in the scattering shell have highly relativistic thermal energy.

3.7.1 Thomson scattering

Data set

From a *Swift* GRB early X-ray afterglow catalog presented in O’Brien et al (2006), we choose a sample of 10 bursts all of which show clearly a “canonical” behavior that includes a shallow decay component. We apply our simple scenario to these bursts, and assume that: (1) the last γ -ray photon that was emitted from shell 1 traveled directly to the observer (primary emission); (2) at the same time and from the same site on shell 1, another photon traveled to shell 2, was scattered, and eventually became the last X-ray photon of the shallow decay phase (scattered emission). Therefore, we will use the ratio of the flux density at X-ray energy at the end of the shallow decay and the flux density at γ -ray energy at the end of the γ -ray emission. Theoretically, this ratio should fit our equation (14) if the shallow decay were to have its origin in the scattered emission scenario.

For the γ -ray photons, the catalog in O’Brien et al. (2006) only gives a mean BAT flux. We use this mean flux as an approximation to the flux at the end of γ -ray emission; the flux density at a specific photon energy is obtained using the BAT spectral index β_{BAT} ($f_\nu \propto \nu^{-\beta_{BAT}}$). For the X-ray photons, we use the XRT flux at the end of the shallow decay and the X-ray spectra index β_X ($f_\nu \propto \nu^{-\beta_X}$) to obtain the flux density at a specific photon energy.

In our theory R_1 is an unknown parameter, but we should be able to extract it from the available data: $R_1/(2\Gamma_1^2)$ is the γ -ray burst duration T_{90} for FREDs (fast rise and exponential decay) - those bursts whose light curves are made of one smooth or two

overlapped pulses; and for bursts with multiple spikes in light curves, $R_1/(2\Gamma_1^2) < T_{90}$. Note that $R_1/(2\Gamma_1^2)$ is equal to the curvature time scale - the delay between two photon's arrival times, one emitted from shell 1's visible edge and the other from the center of shell 1's visible region. Thus, the γ -ray variability time scale, if we assume it is mainly determined by the curvature time scale, would be a good approximation for $R_1/(2\Gamma_1^2)$. Therefore, we look up the γ -ray light curves from the Swift archive²; for FREDs, $R_1/(2\Gamma_1^2)$ is simply T_{90} , but for those spiky bursts, we use the duration of the *last* pulse. The data obtained for our sample of 10 bursts has been organized in Table 1.

Comparison between observations and theory predictions

For the X-ray shallow decay $\Gamma_2/\Gamma_1 = 1$ is a limiting case, since for $\Gamma_2/\Gamma_1 > 1$: (i) the scattered emission from the γ -rays would fall at a higher energy, not in the X-rays, according to equation (21), and (ii) would have a smaller duration than the γ -rays duration according to equation (22), which is not what it is observed - the shallow decay in X-ray light curves typically extends up to 10^4 s.

In Figure 3.3, we plot our 10 GRBs sample data and the results of our theoretical calculations for two cases. For the first case, the 10 data points use the XRT flux at 1 keV (scattered emission) and the BAT flux at 100 keV (primary emission), which corresponds to $\Gamma_2/\Gamma_1 = 0.1$ according to equation (21). For the time delay, we use $(T_s - T_p) \approx t_{end}$, where t_{end} is the end time of the shallow decay - we do this because $T_{90} \ll t_{end}$. For $R_1/(2\Gamma_1^2)$, we use the method described in the last subsection. These values are also listed in Table 1.

In the same figure, for the second case, the 10 data points use the XRT flux at 1 keV (scattered emission) and the BAT flux at 10 keV (primary emission). This corresponds to $\Gamma_2/\Gamma_1 = 1/\sqrt{10} \approx 0.3$, according to equation (21). We consider this case to see if the shallow decay might be produced by the scattering of the low energy tail of the γ -ray emission. Since in this case shell 2 is faster than in the first case described above, the time delay in the ejection of the shells will be larger.

The normalized time delay for the sample has a range of $2 \times 10^2 < (T_s - T_p)/(R_1/2\Gamma_1^2) < 2 \times 10^3$. For fiducial parameter values $\Gamma_1 = 100$, $\Gamma_2 = 10$ and $\theta_j = 0.1$, using equations

²http://heasarc.gsfc.nasa.gov/docs/swift/archive/grb_table/

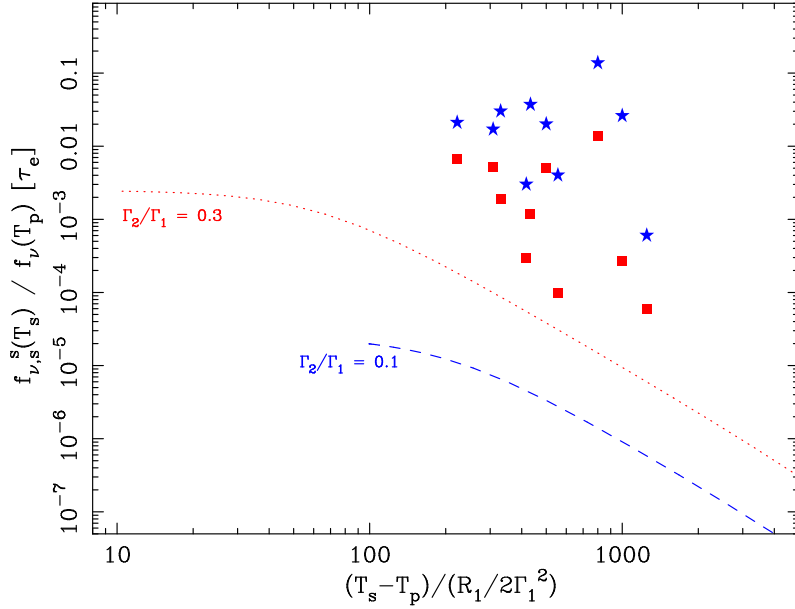


Figure 3.3: Similar to Figure 3.1 but with the GRB sample data added. The stars (squares) are our GRB sample data using the ratio between the XRT flux density at the end of the shallow X-ray decay at 1 keV and the mean BAT flux density at 100 keV (10 keV). The dashed (dotted) line is the result of our theoretical calculation.

(11) and (17), this range has a constraint on α_j'' : $0.1 < \tan \alpha_j'' < 1$. Since this angle is not very small, the approximation of the homogeneous incident flux on shell 2 that was used in deriving the scattered flux formula in §3.3 will slightly overestimate the observed scattered flux.

Results

Figure 3.3 shows that the observed flux ratios of the sample are generally $(10^3 - 10^4)\tau_e^{-1}$ times larger than the theoretical expectation. The discrepancy would be a factor of $\sim 10^4 - 10^5$ for a modest value of $\tau_e \sim 0.1$. This indicates that the emission of the shallow decay is too luminous to be interpreted simply by the scattering within the two shell scenario.

The same figure shows a smaller discrepancy between the sample data and the theoretical curve for a case where shell 2 is slightly faster but still not exceeding the γ -ray shell's speed. Using a modest value of $\tau_e \sim 0.1$ would make this discrepancy to be $\sim 10^2$.

3.7.2 Inverse Compton scattering in shell 2

Comparison between observations and theory predictions

To compare the fluxes of the X-ray shallow decay with the theoretical expectation of the inverse Compton scattering scenario, we fix the scattered frequency, $\nu_s = 1$ keV. With equation (24) we can determine the frequency of the primary emission. The flux ratio data points in Figure 3.3 have to be changed because the frequency ratio is changed. The flux in the γ -ray band follows $f_\nu \propto \nu^{-\beta_{BAT}}$. With this, we can now determine that the data points in Figure 3.2 will be multiplied by a factor of $[(\Gamma_2/\Gamma_1)^2 \gamma_e^2 \nu_\gamma / \nu_X]^{-\beta_{BAT}}$ to account for the inverse Compton scattering effect, where ν_γ and ν_X are the γ -ray and X-ray photon frequencies, respectively, at which the flux densities are used in the data points of Figure 3.3.

Since γ_e is an unknown quantity we cannot determine where these new points would lie on a plot analogous to Figure 3.3. For this reason, we ask: what is the value of γ_e necessary to lower all data points to the theoretically expected curve? To answer, let us fix the value of the Lorentz Factor ratio, $\Gamma_2/\Gamma_1 = 0.1$ — this is a reasonable value according to equation (22), since the γ -ray duration usually lasts $\sim 10^2$ s and the shallow decay extends to $\sim 10^4$ s.

The required values for γ_e are presented in Table 3.2. We present two different values for each burst. We use the BAT spectral index (subscript c) and an average between the BAT and XRT spectral indices (subscript e), respectively. We do this because we are extrapolating the γ -ray flux to energies below the observed BAT band and it is unknown if the BAT spectrum will behave as a single power law in this region.

Electrons' energy in shell 2

We calculate E_e for each burst in our sample using equation (25). The results are presented in Table 3.2, adopting $\Gamma_1 = 10^2$, $\Gamma_2/\Gamma_1 = 0.1$ and $\tau_e = 0.1$. Note that we have corrected $R_1/(2\Gamma_1^2)$ for the cosmological time dilation effect. Two values of energies from the two values of γ_e obtained in the last subsection are given in the table.

Note that from equations (16) and (17) one can see that $R_2/R_1 = 1/2 + \beta_2/(2\beta_1) -$

Table 3.2: Calculated values for the required γ_e and total electron energy of shell 2 to obtain the theoretical expected flux ratio. The calculations were done with two different spectral indices: the BAT spectral index and the average between the BAT spectral index and the XRT spectral index.

GRB	Redshift ^a	$R_1/(2\Gamma_1^2)$ ^b	γ_e ^c	E_e ^d	γ_e ^e	E_e ^f
		(s)	$[\tau_e^{-\frac{1}{2\beta}}]$	(erg)	$[\tau_e^{-\frac{1}{2\beta}}]$	(erg)
050315	1.95	10	34	5×10^{52}	23	3×10^{52}
050319	3.24	9.4	316	5×10^{53}	46	5×10^{52}
050713A		5.3	1364	1.4×10^{54}	95	5×10^{52}
050713B		34	2404	1.5×10^{56}	657	3×10^{55}
050714B		13	13	2×10^{52}	5	7×10^{51}
050803		24	1931	6×10^{55}	547	1×10^{55}
050814	5.3	23	25	2×10^{53}	22	2×10^{53}
050819		9.5	10	1×10^{52}	13	1.5×10^{52}
050822		8	21	1.6×10^{52}	19	1.4×10^{52}
050915B		10.5	33	6×10^{52}	17	3×10^{52}

^aReferences for known redshifts: GRB 050315: Kelson & Berger (2005); GRB 050319: Fynbo et al. (2005); GRB 050814: Jakobsson et al. (2006). For bursts without measured redshift, we use the mean redshift $z=2.8$ of the Swift GRB redshift distribution (Jakobsson et al. 2006).

^bCosmological time dilation corrected curvature variability time scale; it is equal to the $R_1/(2\Gamma_1^2)$ in Table 1 divided by $(1+z)$.

^cRequired shell 2 electron thermal LF using β_{BAT} as the spectral index.

^dIsotropically equivalent total energy of electrons with γ_e calculated in the last previous column for $\tau_e = 0.1$.

^eRequired shell 2 electron thermal LF using $(\beta_{BAT} + \beta_X)/2$ as the spectral index.

^fIsotropically equivalent total energy of electrons with γ_e calculated in the last previous column for $\tau_e = 0.1$.

$(T_s - T_p)/(2R_1) \simeq 1 - (T_s - T_p)/(R_1/2\Gamma_1^2)/(4\Gamma_1^2)$. In our data sample $(T_s - T_p)/(R_1/2\Gamma_1^2) \leq 10^3$. Therefore, the approximation made in the derivation of equation (25), that $R_2 \approx R_1$ for $\Gamma_1 \sim 10^2$, is valid.

Results

Table 3.2 shows that the isotropically equivalent total energy carried by the electrons of a hot shell 2 is large, $\sim 10^{52-56}$ erg. If we take into account the cooling of the electrons via adiabatic expansion and/or radiation, the initial total energy when the electrons were just accelerated is even bigger. The optical depth, τ_e , would certainly decrease the total energy

but only by a small fraction. The prompt emission from those electrons in shell 2 would arrive at about the same time as the scattered emission, and the two emission components would have similar durations because both durations are $\propto 1/\Gamma_2^2$. Depending on the ejecta properties, e.g., the ratio of the shell 2 energy to the shell 1 energy, the shell 2 prompt emission might dominate the scattered emission in the light curve. If that is true, the shell 2 prompt emission might be a possible origin of the late X-ray flares in bursts for which both the flares and the shallower decay are present.

3.8 Faster shell 2

In the previous section we assumed a slower shell 2. What if shell 2 is faster than shell 1? Based on the formulae we have, if $\Gamma_2 > \Gamma_1$, the scattered emission from γ -rays would fall in higher energies, e.g., \sim MeV, not in the X-rays, and have a shorter duration than the γ -rays.

It is shown in Figure 3.2 that, in the $\Gamma_2 > \Gamma_1$ cases, the scattered emission is very bright though it decreases with increasing time delay. If the scattered emission spectrum mimics the power law form of the primary emission spectrum, at some time delay significantly larger than the duration of the primary emission, the lower-energy-extrapolated scattered flux is close to or even brighter than the prompt γ -rays. According to Figure 3.2, for $\Gamma_2/\Gamma_1 \simeq 3$ (corresponding to $\nu_s/\nu \simeq 10$ according to equation (21)) and a selected observed time delay $(T_s - T_p)/(R_1/2\Gamma_1^2) \simeq 100$ (which corresponds to an ejection delay $\delta t \sim 10^3$ s), $f_{\nu,s}^s(T_s) \approx 0.1[\tau_e]f_\nu(T_p)$. Extrapolating the scattered flux density from ν_s to ν , we have $f_\nu^s(T_s) = (\nu_s/\nu)^{\beta_{BAT}} \times 0.1[\tau_e]f_\nu(T_p) \approx f_\nu(T_p)[\tau_e]$ for $\beta_{BAT} \approx 1$. For a smaller observed time delay, the flux is even greater. That means we should have seen a lagged very short γ -ray flash at $\sim 10^2 - 10^3$ seconds after the burst, provided that $\tau_e \approx 1$. This case cannot happen because the observations have never showed this feature. Even though the flux of the scattered emission is smaller for a larger observed time delay, in order for the delayed scattered γ -ray flash to indeed happen but below the BAT flux limit, shell 2 must have an extremely large ejection time delay $\delta t \geq$ a few $\times 10^3$ seconds (cf. equation 17) which is very difficult to explain in terms of the central engine activity. For $\tau_e \ll 1$, the

$\Gamma_2 > \Gamma_1$ case could have happened but the flux would be too small to be detected.

One possible case of $\Gamma_2 > \Gamma_1$ is that the shell 2 ejection delay δt is small and shell 2 has moved very close to shell 1 when the scattering happens so that the observed time delay of the scattered emission is comparable or smaller than the duration of the primary emission. The scattered emission in the BAT energy range will become part of the observed prompt γ -ray emissions in time. High energy (\geq MeV) observations (e.g., by *Fermi*) during the burst may be able to determine the existence of this case.

3.9 X-Ray dim or dark GRBs

In §3.7, our calculations show that the scattered flux is much lower than the observed X-ray shallow decay flux. If the scattering indeed happens, then the resultant emission must have been buried in the shallow decay. Thus, in order for the scattered emission to be detected, not only the shallow X-ray decay component must be absent, but also the normal external forward shock component must be extremely weak or absent. In rare cases Swift does observe X-ray afterglows without a shallow decay and without the normal forward shock decay ($\alpha_X \sim 1 - 1.3$), which we call *X-ray dim GRBs*. They show instead a very steep flux decay ($\alpha_X \geq 3$) and are thought to be located in extremely low density regions. The steep decay component can be explained by the large angle emission (Kumar & Panaitescu 2000). GRB 050421 and GRB 051210 are two examples (Godet et al. 2006; La Parola et al. 2006). Note that GRB 051210 is of the short burst class which, according to its compact binary progenitor model, is more probable to occur in a low density environment. At late times, however, when the large angle emission is low enough, neither burst shows any sign of re-brightening atop the steep power-law decay.

Another case of interest is the existence of *X-ray dark GRBs*: short bursts (GRB 050906 and GRB 050925) that show no X-ray afterglow detection, only upper limits at ≈ 100 s (Nakar 2007). It is also believed that these bursts took place in extremely low density environments.

X-ray dim and dark GRBs provide a great opportunity to put into work the theory presented in this chapter. If we assume that there is a late ejecta behind the γ -ray producing

source, then we can try to constrain its LF by looking at these bursts. Since their afterglow emission is so weak (or not present), we can ask the question: what are the constraints on the LF of the late ejecta, so that the scattered emission is present in X-ray dim and dark GRBs, but doesn't exceed the actual flux observations or upper limits? We will devote this section to answer this question.

We'll start by using the data from *Swift*'s BAT and XRT observations as follows:

$$\frac{f_{\nu,s}^s(T_s)}{f_{\nu}(T_p)} \leq \frac{f_{\nu,s}^{XRT}(T_s)}{f_{\nu}^{BAT}(T_{90})} = 0.01 \frac{f_{1keV}^{XRT}(T_s)}{f_{100keV}^{BAT}(T_{90})} \left(\frac{\Gamma_1}{\Gamma_2}\right)^2$$

where we have selected $\nu = 100$ keV, but we have made no assumption on the value of ν_s only that it should obey equation (21). We have also assumed $\beta_X = 1$, which is consistent with *Swift* observations.

With the previous inequality and using the two previously defined regions of the flux ratio (§3.6), we can find constraints on the LF ratio. In region I, we find:

$$\frac{\Gamma_2}{\Gamma_1} \leq \min \left\{ 20 \left(\frac{T_s - T_p}{R_1/2\Gamma_1^2} \right)^{-1} \theta_{j,-1} \Gamma_{1,2}, 1.26 f_{X\gamma}^{1/6} \tau_e^{-1/6} \right\} \quad (3.26)$$

and in region II:

$$20 \left(\frac{T_s - T_p}{R_1/2\Gamma_1^2} \right)^{-1} \theta_{j,-1} \Gamma_{1,2} < \frac{\Gamma_2}{\Gamma_1} \leq 0.1 f_{X\gamma}^{1/4} \left(\frac{T_s - T_p}{R_1/2\Gamma_1^2} \right)^{1/2} \theta_{j,-1}^{-1/2} \Gamma_{1,2}^{-1/2} \tau_e^{-1/4}, \quad (3.27)$$

where we have used $f_{X\gamma} \equiv f_{1keV}^{XRT}(T_s)/f_{100keV}^{BAT}(T_{90})$ and the convention $Q_x = Q/10^x$ has been adopted.

After presenting these last two conditions, we should return to the physical picture. The initial assumption we made is that the scattered emission should be present independently of the burst's data and its region. This means that the LF of the late ejecta could be very small, so that its contribution to the flux would be also minuscule. Therefore, we should discard the lower limit on equation (27). Now, we want to constrain the LF of the late ejecta from above; we are interested in knowing what's its maximum. The maximum value between the two upper limits of equations (26) and (27) will be the best and more

conservative value to choose:

$$\frac{\Gamma_2}{\Gamma_1} \leq \max \left\{ \min \left\{ \begin{array}{l} 20 \left(\frac{T_s - T_p}{R_1/2\Gamma_1^2} \right)^{-1} \theta_{j,-1} \Gamma_{1,2} \\ 1.26 f_{X\gamma}^{1/6} \tau_e^{-1/6} \end{array} \right\}, \begin{array}{l} 0.1 f_{X\gamma}^{1/4} \left(\frac{T_s - T_p}{R_1/2\Gamma_1^2} \right)^{1/2} \theta_{j,-1}^{-1/2} \Gamma_{1,2}^{-1/2} \tau_e^{-1/4} \end{array} \right\}$$

Now we are ready to consider the 4 bursts mentioned at the beginning of this section and obtain the constraints for the LF of the late ejecta.

Using the last X-ray detection of GRB 051210 (La Parola et al. 2006) and the upper limit of GRB 050421 (Godet et al. 2006), both at $\sim 10^3$ s, we can obtain the ratio between the XRT flux density at 1 keV (scattered emission) and the BAT flux density (Chincarini et al. 2007) at 100 keV (primary emission), $f_{X\gamma}$. Following the procedure outlined in §3.7, the values for $(T_s - T_p)/(R_1/2\Gamma_1^2)$ are also obtained³. We can do exactly the same for the *X-ray dark short GRBs*, using the upper limits of GRB 050906 and GRB 050925 at ≈ 100 s (Pagani et al. 2005; Beardmore et al. 2005; Nakar 2007). With $f_{X\gamma}$ and the normalized time delay, we find the following constraints:

$$\frac{\Gamma_2}{\Gamma_1} (\theta_{j,-1} \Gamma_{1,2})^{1/2} \tau_e^{1/4} \lesssim \begin{cases} 0.15 & \text{for GRB 050906 and 050925} \\ 0.48 & \text{for GRB 050421} \\ 0.78 & \text{for GRB 051210} \end{cases}$$

The upper limits for the *X-ray dark short GRBs* provide the best constraints, since the upper limits in their X-ray flux are very strict. These results imply that, for $\tau_e = 1$, $\Gamma_1 = 100$ and $\theta_j = 0.1$, the late ejecta is very slow $\Gamma_2 \lesssim 15$, but it could be faster if τ_e decreases.

³When following §3.7 to determine the normalized time delay, there is some uncertainty determining the width of the pulses since the data shows statistical noise. For GRB 050421, two possible values for the normalized time delay were obtained hence two constraints for the LF ratio were derived. The value reported here is the more conservative one.

3.10 Summary and Conclusions

We have investigated a scenario of photons scattering by electrons within a relativistic outflow. The outflow is composed of discrete shells. One front shell emits radiation, observed as the GRB's prompt γ -ray photons. Some fraction of the radiation is incident backwards to the shell(s) behind, and is scattered isotropically in the local rest frame. The scattered emission arrives at the observer at a later time, T_s , and at a different photon energy, ν_s , that are determined by the LF ratio of the two shells and the time delay of the ejection of the second shell. We calculated the flux density ratio, i. e., the flux density of the delayed scattered emission to that of the front shell's primary emission, as a function of the normalized arrival time delay and the assumed LF ratio.

The calculated flux density ratio are compared with observations using a sample of *Swift* GRB X-ray afterglows which show a distinct shallower decay component in their light curves, with the motivation to see if the scattering scenario could be the origin of the shallower decay. The results are negative. For Thomson scattering, the flux density of the scattered emission is about $10^{3-4}\tau_e^{-1}$ times lower than that of the shallower decay component, where τ_e is the scattering shell's electron optical depth.

We also consider the inverse Compton scattering scenario in which the electrons in the scattering shell is hot. We find that, in order for the scattered emission flux to be bright enough to match the shallower decay component, the isotropic equivalent of the total energy carried by the hot electrons is large, $\sim 10^{52-56}$ erg. The prompt emission from the scattering shell appears at the same time as the scattered emission and with a similar duration.

In the cases where shell 2 is faster than shell 1, when extrapolated to the BAT energy band, the scattered flux can be as bright as the emission from shell 1. The delay of the scattered emission is determined by the ejection delay of shell 2. When the ejection delay of shell 2 is much larger than the duration of the primary emission, the scattered emission would appear as a late short γ -ray/MeV flash. For a small ejection delay of shell 2, the scattered emission would become part of the observed prompt emission. The fact that no late short γ -ray/MeV flash is detected does not support the existence of a late faster shell.

Lastly, we study the possibility of detection of the scattering emission in two X-ray

dim GRBs - that only show a very steep flux decay and do not show either a X-ray shallow decay nor the normal forward shock component - and in two X-ray dark short GRBs - that show no X-ray afterglow detection at ~ 100 s. Assuming that there is slower moving ejecta material behind the fast γ -ray producing shell in these bursts, we find upper limits for the Lorentz factor of the late slower material. More sensitive observations of X-ray dark short GRBs could provide stronger constraints on the presence and properties of slower moving material accompanying the fast γ -ray jet in GRBs.

Almost simultaneous to the appearance of this work, Panaitescu (2007) presents a similar work on the scattering of the GRB early emission photons by a late outflow. Both work present the same physics and the main formulae are consistent. The main differences are that (i) we have considered the scattering within the relativistic outflow and the photons to be scattered are the prompt γ -ray photons, whereas Panaitescu (2007) considers the scattering of the afterglow forward shock photons by a late relativistic outflow, and (ii) Panaitescu (2007) has considered a faster second shell to be able to explain features like the “shallow decay” and the X-ray flares, whereas our focus is mostly on a slower second shell.

Chapter 4

Scattered X-ray Emission by Dust Grains near GRB Sites

4.1 Introduction

Chapter 1 has reviewed the generic behaviour in X-ray afterglows of GRBs discovered by Swift: firstly steep decline, followed by a shallow decay, then by a “normal” decay. The intervening shallow decay, sometimes called the ‘plateau’, is the most puzzling feature of the X-ray light curve (LC). The most straightforward interpretation is a late steady energy injection into the external shock. However, this interpretation implies a steady, late activity of the central engine – lasting as long as a day – which poses a challenge to the models of the central engine. There is a long list of alternative models for the plateau phase, but none of them satisfy all the observational constraints.

An attractive possibility was suggested by Shao & Dai (2007) regarding the origin of the X-ray plateau. If the long-duration GRB progenitors are massive stars, it is very likely that dust exists in the vicinity of the GRB site since it is in a star forming region. The X-ray photons from the GRB and its afterglow can be scattered in small angles by the dust near the line-of-sight to the GRB, as analogous to the halo emissions of other X-ray sources (e.g., Smith & Dwek 1998). The GRB prompt emission scattered off the dust has been considered earlier by Esin & Blandford (2000) and Mészáros & Gruzinov (2000). Aside from the scattering by the dust local to the GRB site, Miralda-Escudé (1999) considered

the scattering of the X-rays from the GRB afterglows by the dust in the intervening galaxies along the line-of-sight to the GRB, but the flux turns out to be very low and difficult to detect for that case. Depending on the distance of the local dust region to the GRB site, a delayed emission component from the scattering can show up in the afterglows. Shao & Dai (2007) and Shao et al. (2008) used this scenario to interpret the plateau phase in the X-ray afterglow LC as to be the scattered prompt X-rays by the dust located at about ten to a few hundred pc from the GRB site. The scattering happens preferentially within a characteristic scattering angle θ_c which is dependent on the photon energy E and the dust grain size. At larger angles the differential scattering cross section of the dust grains decays steeply. Therefore the scattering within θ_c gives rise to a plateau phase whose duration is determined by θ_c and the distance of the dust region to the GRB site. Larger angle scattering produces a $F(t) \propto t^{-2}$ decay following the plateau. This model does not need to invoke a long steady central engine activity. In addition, since the scattering only works in the X-ray band, the lack of a simultaneous break in optical LC does not pose a problem for this model.

The purpose of this work is to carefully investigate the output of this dust scattering model - in terms of the spectral and temporal properties of the scattered emission - and to compare it with the data. The chapter is structured as follows. We first calculate and quantify the softening expected from the dust scattering model in Section 4.2. Then, we search in the data for evidence in favour of the model including the spectral evolution in the plateau and post-plateau phases for a sample of GRBs in Section 4.3 and 4.4. An expected difference in hard X-ray and soft X-ray LCs is discussed in Section 4.5. We calculate and discuss the optical extinction for the dust in Section 4.6. Our conclusion and further discussion are presented in Section 4.7. Throughout this chapter the spectral index β and the time decay index α of the emission flux are defined as in $f_\nu(t) \propto \nu^{-\beta} t^{-\alpha}$.

4.2 Spectral softening in dust echo emission

We first derive the temporal and spectral properties of the scattered emission or the ‘echo’ (hereafter we use ‘echo’ and ‘scattered emission’ interchangeably) by the dust in the simplest

geometry where the dust is concentrated in a thin layer (or a dust “screen”) near the GRB, following Shao & Dai (2007). Then we consider a generalised geometry where the dust is distributed in an extended zone.

Let us consider a dust “screen” located at a distance R from the GRB source. This dust screen does not have to enclose entirely the GRB source, as long as its angular size with respect to the GRB site is larger than the characteristic scattering angle θ_c (see below). The grains in the dust have a size distribution $dN(a)/da \propto a^{-q}$ within a range (a_-, a_+) , where a is the grain size, q is the distribution index and $N(a)$ is the column density of all grains with size $\leq a$. In this work we use these typical values $a_- = 0.025 \mu\text{m}$, $a_+ = 0.25 \mu\text{m}$, and $q = 3.5$ inferred from the observations (Mathis et al. 1977; Mauche & Gorenstein 1986; Draine 2003). We found that adopting other typical values did not change our main results. Consider a GRB source with a fluence per unit energy $S(E)$ [$\text{erg cm}^{-2} \text{ keV}^{-1}$] at X-ray photon energy E . Since the GRB source duration (~ 10 s) is much shorter than the plateau, it can be considered as being instantaneous.

The flux of the dust scattered emission per photon energy, per grain size, at time t can be estimated by

$$F_{E,a}(t) = \frac{S(E)}{t} \tau[E, a, \hat{\theta}(t)], \quad (4.1)$$

where $\tau[E, a, \hat{\theta}(t)]$ is the scattering optical depth per grain size a , to the photon with energy E and at the scattering angle $\hat{\theta}(t)$; $\hat{\theta}(t)$ is given by the geometrical relation $t = R\theta^2/(2c)$.

The angular part of the optical depth can be separated out from τ by

$$\tau[E, a, \hat{\theta}(t)] = 2\tau_a(E) j_1^2[\hat{x}(E, a, t)], \quad (4.2)$$

where $\tau_a(E)$ is the total optical depth per grain size a and to the photon energy E ; $j_1(x) = \sin(x)/x^2 - \cos(x)/x$ is the spherical Bessel function of the first order which describes the scattering-angle dependence of the cross section, and $\hat{x} = 2\pi Ea\theta/(hc)$ is the scaled scattering angle where h is the plank constant and c is the light speed (Overbeck 1965; Alcock & Hatchett 1978). Via the geometrical relation, \hat{x} can be expressed in terms of E , a and t :

$$\hat{x} = \frac{2\pi}{hc} \sqrt{\frac{2ct}{R}} Ea. \quad (4.3)$$

$j_1^2(x)$ increases as $\propto x^2$ from $x = 0$ to $x \simeq 1.5$ and then drops rapidly as $\propto x^{-2}$ for $x > 1.5$. Therefore, at a given photon energy E , the echo flux LC first appears as a plateau, then transitions to a decay as steep as $\propto t^{-2}$. The transition time, which corresponds to a characteristic scattering angle θ_c and in turn to $\hat{x} \simeq 1.5$, would be given by

$$t_c = 4.5 \times 10^4 \left(\frac{E}{1\text{keV}} \right)^{-2} \left(\frac{R}{100\text{pc}} \right) \left(\frac{a}{0.1\mu\text{m}} \right)^{-2} \text{ s.} \quad (4.4)$$

We see from Eq. (4) that the duration of plateau is very sensitive to the photon energy: the plateau at higher energies ends much earlier than that at lower energies. Thus the overall echo emission must experience strong spectral softening. Note that if the echo is observed within a finite energy range, such as in the XRT band (0.3 - 10 keV), the softening must have begun long before the end of the plateau, because the overall plateau ending time is determined by t_c of the softest photon while the softening begins at t_c of the hardest photon; the ratio of the two times is the ratio of the photon energies reversed and squared, e.g., a factor of 1000 for the XRT band.

The dependence of $\tau_a(E)$ on energy and grain size is

$$\tau_a(E) = \tau_0(E = 1\text{keV}, a = 0.1\mu\text{m}) \left(\frac{E}{1\text{keV}} \right)^{-s} \left(\frac{a}{0.1\mu\text{m}} \right)^{4-q}; \quad (4.5)$$

in the Rayleigh - Gans approximation, $s = 2$ (van de Hulst 1957; Overbeck 1965; Hayakawa 1970; Alcock & Hatchett 1978; Mauche & Gorenstein 1986).

The echo emission spectrum at an observer time t is obtained by

$$F_E(t) = \int_{a-}^{a+} F_{E,a}(t) da \propto \frac{S(E)E^{-s}}{t} \int_{a-}^{a+} a^{4-q} j_1^2[\hat{x}(E, a, t)] da. \quad (4.6)$$

The LC can be obtained by integrating $F_E(t)$ over a desired energy bandpass.

The softening can be seen from Eq. (6) as follows. Since $\hat{x} \propto t^{1/2} E a$, at some given time t , \hat{x} might be > 1.5 for the hard photons and < 1.5 for the soft photons, while the intermediate photon energy that defines and separates the “soft” and the “hard” corresponds to $\hat{x} \approx 1.5$ and it decreases with time. For hard photons, $j_1^2(\hat{x}) \propto \hat{x}^{-2}$. Taking E out of the integral in Eq. (6) gives $F_E(t) \propto S(E)E^{-s-2}$, so the spectral index is increased

by 4 for $s = 2$. For soft photons, $j_1^2(\hat{x}) \propto \hat{x}^2$, so $F_E(t) \propto S(E)E^{-s+2}$ and the spectral index is unchanged for $s = 2$. Therefore, the softening happens first in the high energy part of the spectrum, and then propagates toward the lower energies with time, until the spectrum in the whole bandpass is softened - this is also when the plateau of the overall LC approaches to its end - with a change of the overall spectral index $\Delta\beta = 4$ with respect to the source spectrum (cf. Figure 4.2 below). This change in β should be easy to detect if the echo emission dominates the plateau.

We calculate the LCs of the dust echo in the XRT band for a variety of dust parameter values and the echo spectrum at different times. They are exactly the same as those obtained by Shao & Dai (2007) in their Figure 4.3 and Figure 4.4 and thus confirm their results and the analytical scalings derived above.

4.2.1 Extended dust zone

In the vicinity of GRBs, the dust zone may extend over a large distance. To study the difference in the echo emission properties of an extended dust zone and of a thin dust layer, we consider in this subsection a power-law dust distribution over a distance range $[R_-, R_+]$ with the dust number density profile $n(R) \propto R^{-\delta}$, where R is the distance to the source. The grain properties, e.g., size distribution, are assumed to be independent of R . For ease of calculation, we divide the extended dust zone into a series of N discrete thin dust layers ($N \geq 30$; a change of N does not affect the results), located progressively further from the GRB with equal separation in the $\log(R)$ scale. The scattered flux and its spectrum at any given time is the sum of the contributions from all dust layers at that time.

Figure 4.1 shows the LC of the scattered emission from an extended dust zone for varied sets of parameters. It can be seen that the ending time of the plateau is mainly determined by the location of the inner boundary of the dust zone. This is not surprising because the density of the dust is decreasing with radius thus the scattering LC arises mainly from the inner rim of the dust zone. Figure 4.2 shows the spectra of the scattered emission at different times, from which the softening is evident. The LCs in Figure 4.1 and the spectra in Figure 4.2 are almost same as the ones for a single dust layer model (cf. the *thin solid* line in Figure 4.1 and Shao & Dai (2007)'s results in their Figure 3 and 4), which

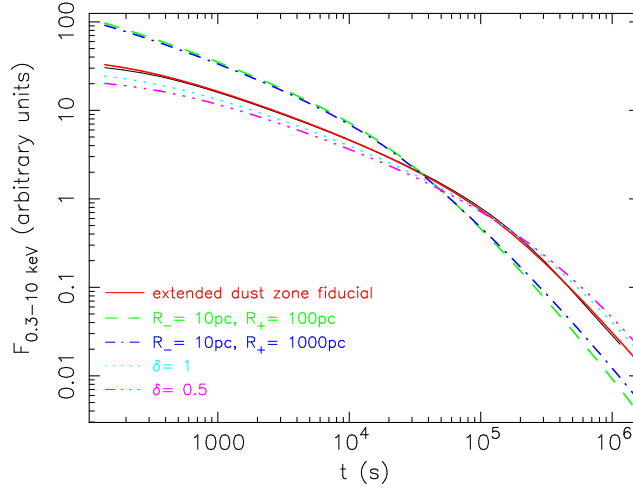


Figure 4.1: The flux light curve in the XRT band of the echo emission from an extended dust zone with a distance range $[R_-, R_+]$. The *thick solid* line (*red* in electronic version) is for the fiducial values used for the parameters of the dust spatial distribution model: $R_- = 50$ pc, $R_+ = 500$ pc, $\delta = 2$. The parameter values for the dust grain properties (same for all the curves) are $a_- = 0.025 \mu\text{m}$, $a_+ = 0.25 \mu\text{m}$, $q = 3.5$, and $s = 2$. The parameter values listed in the legends are the only ones that are changed each time. The assumed source spectrum is a flat power law with a high energy cut-off: $S(E) \propto E^0 \exp(-E/100\text{keV})$. For comparison, the LC from a single dust screen located at $R = 100$ pc with the same total optical depth is also shown here as the (*black*) *thin solid* line.

shows that the generalisation of the model to an extended dust zone does not change much the temporal or spectral behavior of the scattered emission.

We also calculate the overall spectral index in the XRT band at each observer time and the instantaneous decay index of the LC, which are shown in Figure 4.3. Note that, due to the softening, the echo spectrum during the plateau is no longer a single power law function (see Figure 4.2). Thus we calculate a “pseudo” spectral index $\beta_{0.3-10}$ using the flux densities at the two ends of the XRT band, 0.3 keV and 10 keV, respectively, to illustrate the extent of softening with respect to the source spectrum.

The results show that the dust echo emission must experience significant spectral softening; the spectral slope increased by $\Delta\beta \approx 3$ from the early phase of the plateau to the end of the plateau. A more realistic extended dust zone model brings no notable change to this property.

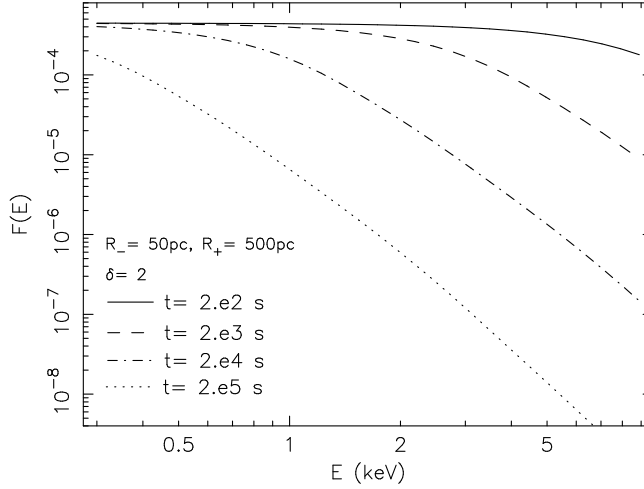


Figure 4.2: The spectrum of the echo emission from an extended dust zone at different observer times. The propagation of the softening toward the low energies is evident. The model parameter values are the same as the fiducial ones in Figure 4.1. The assumed source spectrum is a flat power law with a high energy cut-off: $S(E) \propto E^0 \exp(-E/100\text{keV})$. The change of the spectral index due to the softening is found to be insensitive to the source spectral index.

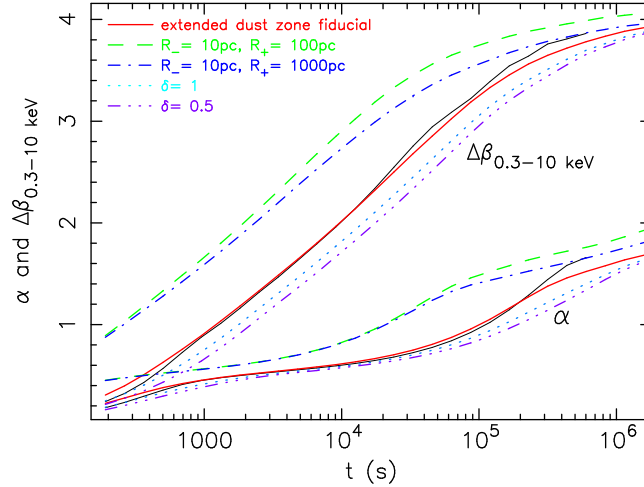


Figure 4.3: The instantaneous flux decay index α (defined as $F_{0.3-10\text{keV}}(t) \propto t^{-\alpha}$) and the spectral softening $\Delta\beta = \beta_{0.3-10\text{keV}} - \beta_0$ for the echo emission from an extended dust zone, where $\beta_{0.3-10\text{keV}} = \log[F_E(0.3\text{keV})/F_E(10\text{keV})]/\log(10/0.3)$ is the two-point spectral index and β_0 is the source emission spectral index. In the cases plotted here we use $\beta_0 = 0$. By changing the values for β_0 , e.g., to $\beta_0 = 1, -0.5$ or -1 , we find that the calculated $\Delta\beta$ is insensitive to β_0 . Each pair of lines for α and $\Delta\beta$ of the same line style correspond to a same set of model parameter values. The *thick solid* lines (*red* in electronic version) are for the same fiducial model parameter values used in Figure 4.1. For comparison, the α and $\Delta\beta$ for the single dust screen model with the same parameter values as that in Figure 4.1 are also shown as the *thin solid* lines (*black* in electronic version).

4.3 Search for spectral evidences in the data

In this section we describe our search for the statistical evidence in the X-ray data during the plateau that can support the dust scattering model. There are two pieces of evidence that we are looking for. First, if the plateau is due to the prompt X-rays scattering off the dust, in the early phase of the plateau when the spectral softening has not yet begun, the spectral index of the scattered emission must be the same as that of the prompt X-rays. Thus we expect to see in the data a correlation between the spectral index of the plateau, which we denote as β_a here, and that of the prompt X-rays. There are two complications to note. (1) For the prompt emission, usually the X-ray spectral index is unavailable so we have to use the one for the prompt γ -rays, β_γ , to represent it; in some cases the X-ray slope might be shallower than the γ -ray slope by 1/2 due to a cooling break. (2) The published spectral index for the plateau is usually measured from the photon counts integrated over the whole plateau duration, therefore this spectrum might be softer than at the beginning of the plateau. Nevertheless, a mild trend of the correlation in the data should still be expected.

The second evidence is based on the strong softening predicted by the model as was demonstrated in Figure 4.2 - 4.3, which show a strong evolution of the spectral index during the plateau and until its end. Thus, if the model is correct, the distributions of the spectral index during the plateau, β_a , for a sample should be significantly smaller than that measured in the post-plateau phase, denoted as β_{ad} .

4.3.1 Sample

A sample of GRBs showing X-ray plateaus with sufficient spectral and temporal information is needed to check for these two evidences. Willingale et al. (2007) analysed 107 Swift XRT detected GRB afterglows and found 80% of the bursts show a plateau in the X-ray LC. Out of the 80% of total bursts sample, 54 have both spectral indices before and after the end of plateau available. We further reduced the sample down to 26 bursts; we rejected those bursts that had one of the following properties: (1) the temporal decay slope $\alpha > 0.8$, too steep to be defined as a “plateau”; (2) XRT coverage is very sparse or long gaps exist

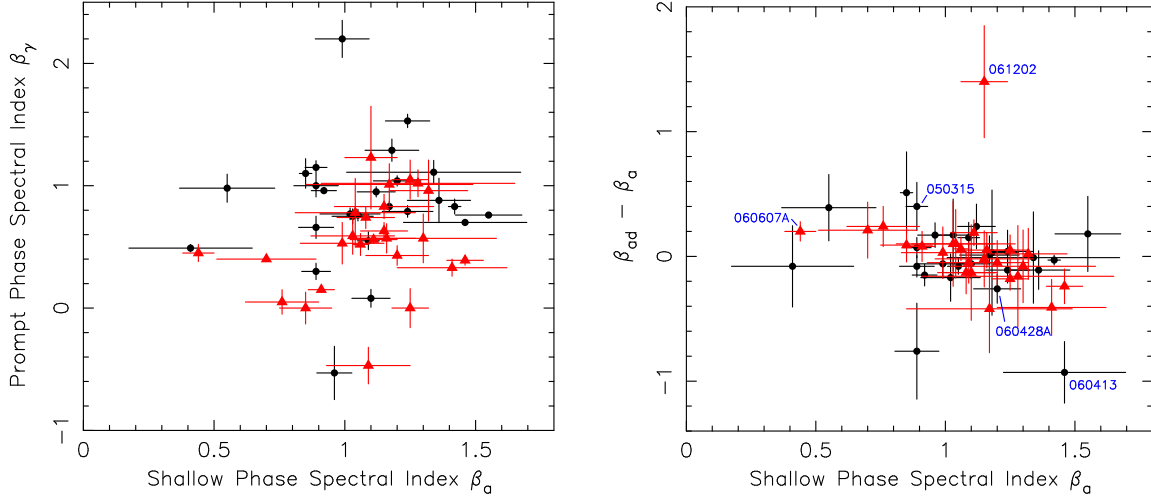


Figure 4.4: **Left:** The prompt phase BAT spectral index β_γ vs. the shallow phase XRT spectral index β_a . **Right:** The change in the spectral index $\beta_{ad} - \beta_a$ vs. β_a , where β_{ad} is the spectral index of the decay after the end of the shallow phase. Several individual cases of GRBs which show evidence of spectral softening or hardening are labeled. The spectral index β is defined as $f_\nu \propto \nu^{-\beta}$. The error bars are 1- σ errors. The sample is selected from Willingale et al. (2007) (*filled circles*, and in *black* color in electronic version) and Liang et al. (2007) (*filled triangles*, and in *red* color in electronic version).

during the plateau; (3) the “plateau” is actually due to one or more flares. We have also included 24 bursts from the sample of Liang et al. (2007) that satisfy the above criteria.

4.3.2 Results

We plot β_γ vs. β_a and the difference between β_{ad} and β_a vs. β_a in Figure 4.4. No clear correlation between β_γ and β_a is seen, which disfavors the dust model. Generally β_a is softer than β_γ . This is consistent with the expected softening during the plateau. However, if it was the softening that could have weakened or broken the expected correlation, there must be a bigger scatter in β_a than in β_γ . The data shows the contrary: β_a is in the range of 0.5 - 1.5 where β_γ is in -0.5 - 1.5. Thus the comparison between β_a and β_γ is inconsistent with the model expectation.

Moreover, no dominant softening trend in the spectral index is seen from the plateau to the post-plateau phase; bursts with smaller β_a show slight softening and those with larger β_a show slight hardening. Most of the bursts show zero spectral change across the end of the plateau within 1- σ measurement error. Only three bursts show evidence of spectral

softening - two bursts at $2\text{-}\sigma$ level (GRB 050315: $\Delta\beta= 0.4$; GRB 060607A: $\Delta\beta= 0.2$) and one burst at $3\text{-}\sigma$ level (GRB 061202: $\Delta\beta= 1.4$). There are also two bursts showing spectral hardening - one at $2\text{-}\sigma$ level (GRB 060428A: $\Delta\beta= -0.26$) and one at $3\text{-}\sigma$ level (GRB 060413: $\Delta\beta= -0.93$). Those individual cases are marked in the right panel of Figure 4.4.

The two results – no correlation between β_γ and β_a and no clear difference between β_a and β_{ad} , also reported in Willingale et al. (2007) and Liang et al. (2007) – are inconsistent with the expectations of the dust scattering model.

4.4 Time history of the spectral during the plateau

The model predicts a significant spectral evolution from the beginning (~ 200 s after the burst) to the end of the dust echo plateau. The spectral index shows a monotonic increase by $\Delta\beta \approx 3\text{--}4$. If the X-ray plateau is indeed due to or dominated by the dust echo emission, the strong spectral softening can be very easily detected in the XRT data. To compare the data with this expectation, we look closely at the time resolved spectral information during the plateau for the best observed GRBs.

To determine whether there is any dominant trend of spectral evolution during the plateau phase, we compile a sample of 21 GRBs with well defined plateau phases, excellent time coverage and good signal-to-noise ratios. For details of how the X-ray light curves used in this work were produced, see Evans et al. (2007). This sample is listed in Table 4.1.

For each GRB, the overall XRT LC is considered to be composed of two components. The first one is the very rapid decay just following the γ -rays. The second component is the plateau and the subsequent normal power-law decay. Both components are well fitted by the same functional form as introduced by Willingale et al. (2007). We define T_1 – the time of transition from the first to the second component – as the time when the two components are equal; this is a good measure of the start of the plateau. T_2 is the end of the plateau and the start of the final power-law decay.

We plot the hardness ratio, as defined by the ratio of the photon counts in 1.5 - 10 keV and 0.3 - 1.5 keV bands, for each time interval of coverage during the plateau phase. We find that all the hardness ratio changes through the plateau phase are quite small and,

for the bursts with the largest change the hardness ratios are getting harder (near the start of plateau), not softer. The ones that get softer do so only slightly. This confirms the findings by Butler & Kocevski (2007).

We measure the spectral index taking into account photo-absorption at lower X-ray energies. We use the absorbed-power-law fit to the spectrum of the early XRT data - mainly the steep decline phase in the LC, which contains most of the photon counts - to determine the neutral H column density given as a combination of two components - the Galactic column and a host intrinsic one. Then we use this neutral H absorption model to convert the measured hardness ratio in the plateau into the spectral index with an appropriate error.

For many GRBs the time coverage during the plateau is rather patchy. Thus we select a time window which includes the plateau and takes into account the coverage. Sometimes it has to include data before T_1 and after T_2 so that the behaviour across the plateau is well constrained. The evolution of the spectral index over the selected time window is fitted as a linear function of the logarithmic time. Extrapolating the best fit function to both sides of the window gives the spectral indices β_1 and β_2 at T_1 and T_2 , respectively. These are the best estimates of the spectral index at the start and the end of the plateau.

Figure 4.5 shows a few examples of the β -evolution during the plateau. The observed β -evolutions for our sample are tabulated in Table 4.1. None of the afterglows show a notable softening over the plateau. Most show zero evolution of β , with very small uncertainty. A few show a small, marginally significant, hardening. For the examples shown in Figure 4.5, we also add in the lower panels of Figure 4.5 the expected β -evolutions from the dust scattering model. A few model parameters (R , q and s) were set free to change and then were optimised in each example in order to best reproduce the observed plateau and post-plateau LC. The expected β is systematically larger than the observed one even at the beginning of the plateau phase, because the softening has already begun there. The expected strong evolution in β distinctly differs from the stableness of the observed β during the plateau.

To summarise this section, though the dust scattering model can nicely fit the LCs of plateau and post-plateau decay (see also Shao et al. 2008), the expected large value and strong evolution of the spectral index sharply contradict the data.

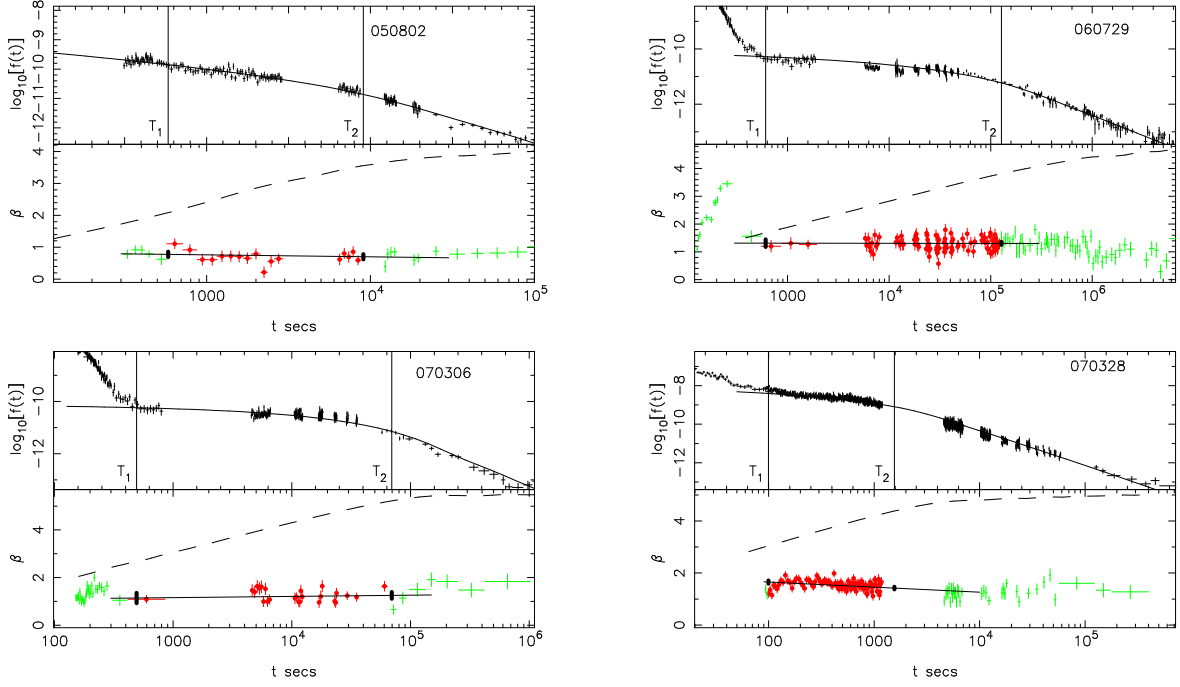


Figure 4.5: The X-ray LC and the time history of the spectral index β for four examples of GRBs with plateaus and the corresponding expectations from the dust scattering model. In the **upper** panel for each example, T_1 and T_2 mark the beginning and the end of the plateau phase, respectively. The plateau phase and the post-plateau decay LC is mimicked by the dust scattered emission through adjusting the parameters (R , q and s) of a single dust screen model (using an extended dust zone model does not change the result), shown as the *solid* line. In the **lower** panel for each example, the time-resolved β are plotted as filled circles inside the $[T_1, T_2]$ window and as crosses outside the window. A linear function of $\log(t)$, as shown by the *solid straight* line, is fitted to the time history of β within the $[T_1, T_2]$ window. The fit extrapolation at T_1 and T_2 gives β_1 and β_2 , respectively, as marked by the filled bars. The *dashed* lines are the expected β -evolutions for the dust models that were optimised in the upper panels.

Table 4.1: The spectral indices at the beginning and at the end of the X-ray plateaus for a sample of GRBs. From a larger sample of GRBs showing well defined plateau phases, only those with high signal-to-noise ratio and long time coverage in the plateau are selected. T_1 marks the transition of the LC from the prompt component to the plateau component. T_2 marks the end of the plateau and the transition to the final power-law decay. β_1 and β_2 are given by the extrapolation of a function fit to the evolution of the spectral index of available data within a window defined by T_1 and T_2 . The error in β is at 90% confidence level.

GRB	T_1 (10^2 s)	β_1	T_2 (10^4 s)	β_2	χ^2/n_{dof}
050315	4.0	1.24 ± 0.17	2.48	0.99 ± 0.08	44.9/29
050319	6.6	0.95 ± 0.14	4.65	0.88 ± 0.13	20.6/17
050401	7.9	0.88 ± 0.06	0.75	0.90 ± 0.10	81.2/51
050713B	7.2	0.87 ± 0.08	2.79	0.93 ± 0.15	16.9/19
050802	5.8	0.78 ± 0.09	0.90	0.70 ± 0.09	31.1/27
050803	2.9	0.76 ± 0.11	0.078	0.62 ± 0.21	9.11/9
060306	4.6	1.34 ± 0.14	0.80	1.31 ± 0.15	20.9/12
060502A	4.6	1.26 ± 0.22	1.78	0.94 ± 0.17	9.4/7
060510A	0.92	1.03 ± 0.22	1.30	1.02 ± 0.09	26.2/23
060607A	8.4	0.96 ± 0.12	5.57	0.83 ± 0.13	28.5/38
060614	22	1.03 ± 0.19	11.5	0.81 ± 0.11	27.8/22
060729	6.1	1.31 ± 0.14	12.7	1.31 ± 0.06	143.8/114
060813	0.32	1.03 ± 0.30	0.047	0.82 ± 0.11	19.5/19
060814	12	0.69 ± 0.11	1.90	0.68 ± 0.09	46.4/31
061121	2.0	1.12 ± 0.11	0.24	0.96 ± 0.10	20.3/27
061222A	1.6	1.36 ± 0.19	0.158	1.26 ± 0.10	49.9/26
070129	14	1.58 ± 0.28	2.78	1.18 ± 0.14	14.0/12
070306	4.9	1.15 ± 0.22	6.95	1.25 ± 0.14	43.4/28
070328	1.0	1.65 ± 0.06	0.16	1.42 ± 0.05	151.4/107
070420	2.1	1.27 ± 0.23	0.37	0.87 ± 0.12	16.9/15
070508	0.69	0.77 ± 0.08	0.10	0.63 ± 0.05	107.1/93

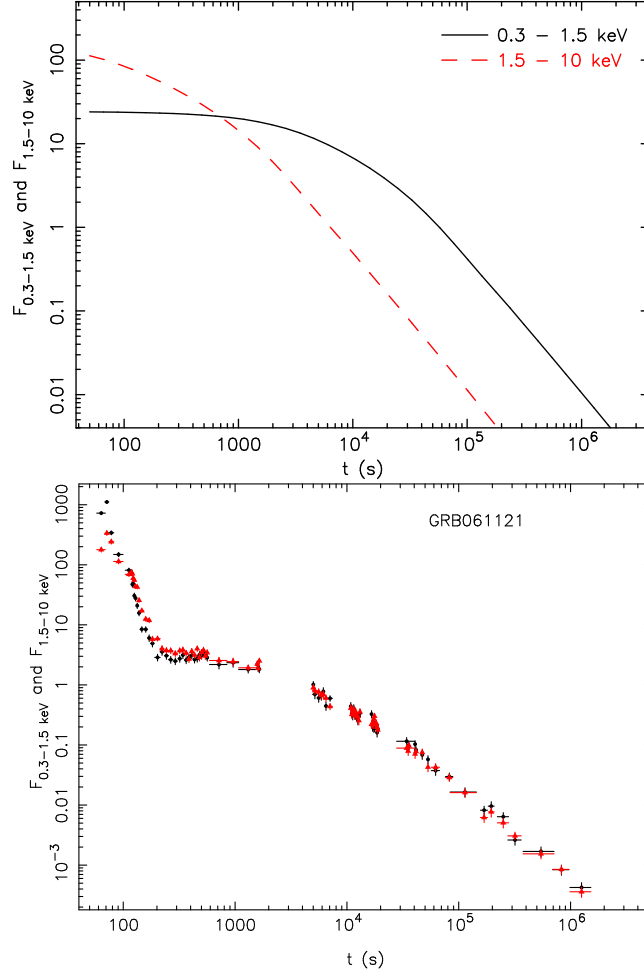


Figure 4.6: The LCs in the soft and the hard X-ray channels, respectively, as predicted by the dust echo model and observed in GRBs. **Top:** The LCs of the echo emission from an extended dust zone model. The values of the model parameters R_- and R_+ are chosen such that the echo emission 0.3 - 10 keV LC best mimics the plateau of GRB061121. Other model parameters are the same as the fiducial ones in Figure 4.1. **Bottom:** The LCs of a typical GRB ‘plateau’ in 0.3 - 1.5 keV (*squares*) and 1.5 - 10 keV (*triangles*), respectively. The early rapid decay at $t < 200$ s of the observed LC does not belong to the plateau phase and it is thought to be of a different origin.

4.5 X-ray LCs in soft and hard energy channels

Another prediction from the dust scattering model is the different temporal behaviours of the LCs in low and high energy channels. This can be seen from equation (4): observations carried out at photon energy E should see the end of the plateau at $t_c \propto E^{-2}$. This feature is demonstrated in the top panel of Figure 4.6 where we calculated the LCs of scattered emission from an extended dust zone in 0.3 - 1.5 keV and 1.5 - 10 keV, respectively. It shows that the soft X-ray LC has a more extended plateau than the hard X-ray one.

We find that for all bursts in our sample of plateau GRBs, the temporal behaviours in soft vs. hard X-ray LCs look identical. As an example, the bottom panel of Figure 4.6 shows the soft vs. hard X-ray LCs of GRB 061121 which has a long, dense time coverage and the best photon statistics among all bursts in the sample (Page et al. 2007). The soft and hard X-ray LCs for this burst are identical. This feature rules out the dust scattering model for the plateau.

4.6 Optical extinction due to the dust

The dust grains which scatter the X-ray photons will also cause extinction in the optical band. This can provide an additional constraint for the dust scattering model. Thus we estimate the extinction in V Band, A_V , caused by the dust required for the model and compare it with A_V derived directly from optical observations.

Predehl & Schmitt (1995) found an empirical relation between the X-ray dust scattering optical depth $\tau(E)$ and A_V for the X-ray halos of 24 galactic X-ray point sources:

$$\tau(E) = 0.06A_V(E/1\text{keV})^{-2}, \quad (4.7)$$

where $\tau(E)$ is obtained from modelling the X-ray halo surface brightness distributions with dust grain properties similar to the fiducial ones we used in our calculations. Draine & Bond (2004) derived a similar relation based on a dust model developed by Draine (2003):

$$\tau(E) = 0.15A_V(E/1\text{keV})^{-1.8}. \quad (4.8)$$

Table 4.2: The fiducial host rest frame optical depth at $E = 1$ keV required by the dust scattering model and the associated rest frame visual extinction for a sub-sample of GRBs with well observed shallow X-ray decays. The fluence and spectral data are from Liang et al. (2007). $A_V^{(1)}$ is given via equation (7) and $A_V^{(2)}$ via equation (8). References to the GRB redshifts: 050315 - Kelson & Berger (2005); 050319 - Jakobsson et al. (2006); 050401 - Fynbo et al. (2005); 050803 - Bloom et al. (2005); 060210 - Cucchiara et al. (2006); 060714 - Jakobsson et al. (2006); 060729 - Thoene et al. (2006); 060814 - Thoene et al. (2007). $z = 2$ is assumed for GRBs without known z .

GRB	S_γ^*	β_γ	S_X^*	β_X	z	τ_0	$A_V^{(1)}$	$A_V^{(2)}$
050128	45	0.5	3.7	0.87		25	414	162
050315	28	0.28	11	1.06	1.95	1.83	30	12
050319	8	0.25	1.3	1.00	3.24	8.4	140	56
050401	140	0.15	9.3	0.91	2.9	12	200	79
050713B	82	0.0	3.3	0.85		6.4	108	42
050803	39	0.05	6.0	0.76	0.42	0.5	8.4	3.4
050822	34	0.0	4.1	1.29		1.7	29	12
060210	77	0.52	10	1.06	3.91	39	650	260
060714	30	0.99	1.5	1.15	2.71	385	6.5×10^3	2.6×10^3
060729	27	0.86	20	1.35	0.54	2.6	43	100
060813	55	-0.47	7.3	1.09		0.22	3.6	1.4
060814	150	0.56	6.9	1.11	0.83	18	308	124
070129	31	1.05	1.5	1.25		315	5×10^3	2×10^3

* In units of 10^{-7} erg cm $^{-2}$.

Note that Eq. (4.7) is for the dust in the Milky Way (MW), while for GRB hosts most absorption fits tend to favour the Small Magellanic Cloud (SMC) extinction law (e.g., Schady et al. 2007; but see the discussion below toward the end of this section). It was shown that the difference between the the MW and SMC extinction laws can be well reproduced in a model by adjusting the relative abundances of graphite and silicate grains, while leaving all other dust properties fixed; in this case A_V and $\tau(E)$ at $E \geq 7$ eV are both the same for these two environments (Pei 1992). Thus it is viable to apply Eq. (4.7) to GRB hosts.

The above relations are for quantities in the rest frame of the source. If the source is at cosmological distances, like GRB hosts, we have to take into account the cosmological redshift of the photon energy when calculating $\tau(E)$ and A_V from the observed quantities. The dust scattering optical depth, $\tau_0 = \tau(E = 1\text{keV})$, in the rest frame of the GRB host at a redshift z can be estimated by

$$S_{X,1} \approx (1+z)^{-2} \tau_0 S_{\gamma,1}, \quad (4.9)$$

where $S_{\gamma,1} = S_{\gamma}(E = 1\text{keV})$ is the specific fluence extrapolated from the Burst Alert Telescope (BAT) total fluence during the burst to 1 keV, $S_{X,1} = S_X(E = 1\text{keV})$ is the specific fluence at 1 keV during the plateau phase, both measured in the observer's frame. There is a factor of $(1+z)^{-2}$ because the ratio $(S_{X,1}/S_{\gamma,1})$ is actually equal to the host rest-frame $\tau(E)$ at $E = (1+z)$ keV and $\tau(E) \propto E^{-2}$ (cf. Eq. 4.5).

We select a sub-sample of GRBs which have good XRT temporal coverage during the afterglow phase from the sample of Liang et al. (2007) that provided S_{γ} and S_X for those bursts. Then τ_0 is calculated and the associated A_V is inferred from τ_0 via Eq. (7) and (8). The sample and the results are listed in Table 4.2. Almost in all cases (except for two) τ_0 is > 1 and some even have $\tau_0 > 10$, which means this model requires that only a very tiny fraction of photons with energy of 1 keV in the host rest frame can escape the dust without scattering. None of the sub-sample have $A_V < 1$ and 85% of them have $A_V > 10$.

In comparison, Schady et al. (2007) determined A_V for 6 GRB afterglows from the Ultraviolet and Optical Telescope (UVOT) to XRT Spectral Energy Distributions (SEDs), with A_V ranging from 0.1 to 0.7. These extinctions are significantly smaller than that

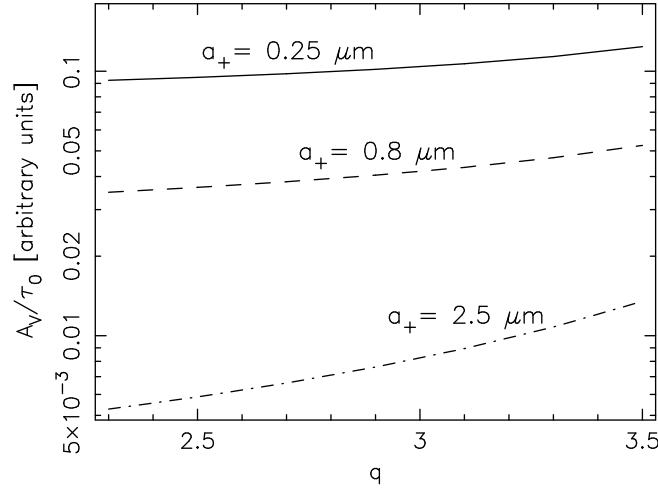


Figure 4.7: The dependence of the ratio A_V/τ_0 of the dust on the grain size distribution parameters a_+ and q . The dust is assumed to have a grain size distribution $dN(a)/da \propto a^{-q}$ within the grain size range $[a_-, a_+]$, where $N(a)$ is the column density of all grains with size $\leq a$.

expected from the dust scattering model. Note that a considerable fraction (1/4 - 1/3) of the plateau X-ray afterglows have bright optical counterparts (Figure 2 of Liang et al. 2007).

But a cautiousness has to be taken regarding the A_V determinations above. There are some recent studies that show the dust properties of GRB hosts does not resemble those of any galaxy in our neighborhood. In particular, Chen et al. (2006), Perley et al. (2008) and Li et al. (2008) have found for some GRBs the modeled extinction curve is “gray”, i. e., much flatter than any of the templates (MW, SMC, the Large Magellanic Cloud). Since our determination of A_V has used the $A_V - \tau_0$ relations appropriate for these template-type dust, these findings are likely to raise uncertainties in the determined A_V .

The dust grain size distribution is usually described by a power law with an index q and within a range of grain size (a_-, a_+) . A “gray” extinction curve could be due to a flatter grain size distribution (smaller q) or a larger a_+ , as suggested by Li et al. (2008). We calculated A_V and τ_0 independently for a dust model with the composition resembling the SMC and the “gray” type that these authors have found for some GRBs, to see the dependence of their ratio on the grain size distribution parameters. The A_V is calculated

by the following equation (Weingartner & Draine 2001)

$$A_V = (2.5\pi \log e) \int_{a_-}^{a_+} a^2 Q_{ext}(a, \lambda_V) \frac{dN(a)}{da} da, \quad (4.10)$$

where Q_{ext} is the extinction efficiency factor, usually a function of grain size and photon energy. Draine & Lee (1984) calculated $Q_{ext}(a, \lambda)$ for graphite and silicate grains. Since the GRB dust environments are described either by SMC or “gray” type extinction curve (Shady et al. 2007; Li et al. 2008), for both of which a good dust composition model needs silicate only (Pei 1992; Li et al. 2008), we use $Q_{ext}(a, \lambda)$ for silicate only. The dust scattering optical depth can be calculated by $\tau_0 = \int_{a_-}^{a_+} \tau_a(E = 1\text{keV}) da$, where $\tau_a(E)$ is given by Eq. (4.5). Note that the normalizations of A_V and τ_0 are unimportant here because we are looking at only their dependences on a_+ and q .

The ratio of A_V/τ_0 for varying a_+ and q is shown in Figure 4.7. We find that A_V/τ_0 is only slightly dependent on q – A_V/τ_0 decreases by factor of ~ 2 for q changing from 3.5 to 2.6; but A_V/τ_0 is more sensitive to a_+ – it decreases by a factor of ~ 10 when a_+ changes from $0.25 \mu m$ to $2.5 \mu m$. Even after taking these effects into account, the A_V we obtained for our GRB sample are still very large (for one half of the sample, $A_V \gtrsim 10$). One of the real problems with the dust scattering model for the X-ray plateau phase is that it requires $\tau_0 \geq 10$ for one half of our sample (see Table 4.2), which seems physically unreasonable.

Thus, the dust scattering model is not a viable explanation for the X-ray plateaus because of the large extinction in the optical band it predicts but not observed.

4.7 Conclusion and Discussion

We have shown that in the dust scattering model the scattered X-ray emission must experience strong softening spectral evolution, with a significant change of the spectral index in 0.3 - 10 keV of $\Delta\beta \sim 2 - 3$ from the emerging of the plateau to its end. However, for a sample of GRBs with X-ray plateaus and with good quality data, no softening spectral evolution during the plateau phase is found, and in a few cases even traces of slight hardening are seen.

The change of β according to the model does not depend on the spectral index of the

source emission. The Rayleigh - Gans approximation is used in this work to calculate the scattering cross section of the dust grain. It was claimed that this approximation tends to overestimate the scattering efficiency below 1 keV, typically by a factor of 4 at 0.5 keV and a factor of 2 at 1 keV, mainly due to the absorption of the soft X-ray photons by the K and L shell electrons in the dust grain (Smith & Dwek 1998), and that could change the spectral slope at the soft end (< 1 keV) and counteract against the softening (Shao et al. 2008). But we argue that this effect does not alleviate the expected softening, because the discrepancy between the real scattering cross section and the Rayleigh - Gans approximation caused by this effect, which is mainly below 1 keV, must have been largely accounted for by the required neutral H absorption in the routine power-law fit to the plateau spectra. The XRT spectral index is mainly determined by the photons with energy above 1 keV which is not affected by this effect. Moreover, this effect is time independent while the softening we consider is a strongly time dependent behaviour. Dust destruction by the GRB prompt emission is of very little relevance here because it happens within a distance smaller than the location of the dust considered in this work (e.g., Waxman & Draine 2000). Thus the Rayleigh - Gans approximation is sufficiently accurate for the effect considered in this work.

The dust scattering model also predicts very different temporal behaviours in the soft X-ray vs. hard X-ray LCs; the plateau lasts longer in soft X-rays. But this feature is not found in the data. Furthermore, the large scattering optical depth of the dust required by this model in order to explain the X-ray plateaus leads to extremely large extinction in optical - $A_V \gtrsim 10$. This is inconsistent with the observed extinctions for GRBs.

We conclude that the dust scattering model, though very attractive, can not explain the X-ray plateaus seen in most GRB afterglows. Although it is very likely that dust exists near the site of GRBs, and will scatter some fraction of the prompt and afterglow X-rays, this scattered emission is not a dominant contributor to the observed X-ray plateau. For those cases where an achromatic break at the end of the plateau is seen, a late, steady energy injection to the external shock is a more likely mechanism for producing the observed X-ray plateau, though it may not be able to work well for the cases with chromatic breaks.

Chapter 5

Prompt Optical Emission Constraints GRB's Emission Site

5.1 Introduction

Although the Gamma-Ray Burst (GRB) was discovered about 50 years ago first through its prompt γ -ray emission, large uncertainties still remain in understanding the prompt emission site, namely, the distance of the emission site from the explosion centre R , with controversial evidence. There are three possible sites discussed in the literature. One is the standard internal-shock site which depends on the fluctuation time scale δt seen in GRB light curves (e.g., Rees & Mészáros 1994, see Piran 2005, Mészáros 2006 for reviews). It can have a large range of $R \sim \Gamma^2 c \delta t \sim 10^{13} - 10^{15}$ cm because δt and Γ vary largely from burst to burst. The second is the photospheric radius at $10^{11} - 10^{12}$ cm at which the prompt emission arises as a combination of the photosphere thermal emission and a Comptonized component above it, the latter being induced by some energy dissipation process below and above the photosphere (e.g. Rees & Mészáros 2005; Ryde et al. 2006; Thompson et al. 2007). The third one is a large radius ($> 10^{14}$ cm) as is supported by the Swift XRT data (Lazzati & Begelman 2005; Lyutikov 2006; Kumar et al. 2007) and Fermi data of GRB 080916C (Abdo et al. 2009; Zhang & Pe'er 2009), possibly due to magnetic dissipation (e.g., Lyutikov & Blandford 2003).

The rapidly responding ability of a few GRB-dedicated ground or space based optical

telescopes, e.g., ROTSE (Akerlof et al. 2003), RAPTOR (Vestrand et al. 2002), TORTORA (Racusin et al. 2008) and the UVOT (Roming et al. 2005) on aboard the Swift satellite, has enabled the time-resolved detection of bright prompt optical emission before the γ -rays die off, for about a dozen of GRBs. Five of these GRBs, i.e., 041219A (Vestrand et al. 2005), 050820A (Vestrand et al. 2006), 051111 (Yost et al. 2007a), 061121 (Page et al. 2007) and 080319B (Racusin et al. 2008), show a temporal correlation between the strongly variable optical flux and the γ -ray pulses, which suggests that the optical emission most likely shares the same dynamical process that is responsible for the highly variable γ -ray emission. While the other four bursts have optical flux densities below or marginally consistent with the extrapolations from the low-energy power law of the γ -ray spectra, the optical flux density in GRB 080319B exceeds the γ -ray extrapolation by 4 orders of magnitude (Racusin et al. 2008; Kumar & Panaitescu 2008), suggesting that for this burst alone the optical emission has a spectral origin different from that of the γ -rays.

In this work, for the four GRBs – 041219A, 050820A, 051111 and 061121 – we assume that the prompt optical and the γ -ray emissions are components belonging to the same synchrotron radiation continuum of a group of hot electrons. Based on this assumption, the self-absorption frequency of the synchrotron electrons, ν_a , which causes a break in the long-wavelength part of the continuum, can be determined or constrained by studying the optical-to- γ -ray spectral energy distribution (SED)¹. Since ν_a is dependent on the properties of the prompt emission source, such as the distance of the emission site from the explosion centre R , the bulk Lorentz factor (LF) Γ and the magnetic field B of the source, from ν_a we can determine or make constraints on R for these bursts, using information on Γ and B obtained in other ways. This is the main goal of this work. Since the prompt optical and γ -ray components in GRB 080319B are most likely of different spectral origins because of its peculiar SED shape, our approach is not applicable to this burst.

On the other hand, for some other long GRBs the rapid response of the dedicated ROTSE telescope has returned only upper limits of the optical flux density during the prompt phase (Yost et al. 2007b). Another goal of this work is to get constraints on R for these optically “dark” bursts and to study whether the prompt optical non-detection is

¹The significance of self-absorption frequency was highlighted by Doi et al. (2007) who used the varying location of ν_a to interpret the diversity in the prompt optical / γ -ray temporal correspondence.

caused by a heavier self-absorption due to a closer emission site to the explosion centre.

In this chapter, we first derive analytically ν_a in terms of R , Γ , B and the emission properties in Section 5.2. The arguments that support our assumption of one synchrotron continuum component for both optical and γ /X-ray are given in Section 5.3. We derive in Section 5.4 the constraints on R through ν_a explicitly, by determining the location of ν_a in the optical-to- γ -ray SED and considering all possible spectral regimes. We apply this method to a prompt optical detection GRB sample and a prompt optical non-detection sample which are described in Section 5.5. The results are presented in Section 5.6. Finally the conclusion and discussions are given in Section 5.7.

5.2 Determining the self-absorption frequency

The GRB high energy emission spectrum is characterized by a smoothly joint broken-power-law form (Band et al. 1993). Thus the relativistic electrons responsible for the GRB prompt emission due to either synchrotron or synchrotron self-inverse Compton (SSC) radiation are in a piece-wise two-power-law energy distribution:

$$N(\gamma) \propto \begin{cases} \gamma^{-p_1}, & \text{if } \gamma_m < \gamma < \gamma_p, \\ \gamma^{-p_2}, & \text{if } \gamma > \gamma_p, \end{cases} \quad (5.1)$$

where $N(\gamma)$ is such defined that $N(\gamma)d\gamma$ is the number density of electrons with energy in the interval of γ to $(\gamma + d\gamma)$, and γ_m is the minimum energy of these relativistic electrons (for convenience we omit the factor $m_e c^2$ in the electron energy $\gamma m_e c^2$ throughout the text when electron energy is mentioned).

Note that although this distribution set-up is phenomenologically based on the two-power-law shape of the high energy radiation spectrum observed in GRBs, it has specific physical meanings. Within the shock acceleration scenario, newly accelerated electrons with a minimum energy γ_i and a power-law energy distribution are continuously injected. These electrons lose energy through radiative cooling, and the instantaneous electron spectrum steepens above a critical energy γ_c . All the electrons with energy larger than γ_c radiate away their energy within a time shorter than the dynamical time. When $\gamma_i < \gamma_c$, our notation

corresponds to $\gamma_m = \gamma_i$ and $\gamma_p = \gamma_c$. When $\gamma_c < \gamma_i$, the cooling causes a flatter power law between γ_c and γ_i , even though the newly accelerated electrons are injected in the energy range above γ_i . For this case one has $\gamma_m = \gamma_c$ and $\gamma_p = \gamma_i$. In summary within the shock acceleration scenario one has $\gamma_m = \min(\gamma_i, \gamma_c)$ and $\gamma_p = \max(\gamma_i, \gamma_c)$. More generally, one can also have a scenario that invokes continuous heating and cooling of electrons (e.g. that envisaged in the reconnection models), and γ_p then reflects the intrinsic break in the steady state electron spectrum. In any case, our treatment is generic, which does not depend on the concrete particle acceleration mechanism and the origin of γ_p .

The broken power-law electron energy spectrum naturally gives rise to a piece-wise power law photon spectrum as commonly observed:

$$f_\nu \propto \begin{cases} \nu^{\beta_1}, & \text{if } \nu_m < \nu < \nu_p, \\ \nu^{\beta_2}, & \text{if } \nu > \nu_p, \end{cases} \quad (5.2)$$

where f_ν is the observed flux density (in units of mJy), ν_m and ν_p are the observed characteristic emission frequencies of the electrons with energy γ_m and γ_p , respectively, and ν_p is usually the peak frequency of the νf_ν spectrum. The low-energy power law ν^{β_1} does not extend to low frequency indefinitely. Without synchrotron self absorption, the spectral index below ν_m changes to 1/3, regardless of whether $\gamma_i < \gamma_c$ or $\gamma_c < \gamma_i$. Below a certain frequency $\nu_a \ll \nu_p$, the synchrotron self absorption starts to play a significant role – at frequencies lower than ν_a the emitted photons are thermalized with the electrons. The self-absorption frequency ν_a is such defined that at this frequency the self-absorption optical depth $\tau_{sa}(\nu_a) = 1$.

Let us determine ν_a for an emitting GRB ejecta moving with a Lorentz factor (LF) Γ at a distance R from the center of the explosion. In the ejecta comoving frame (hereafter the quantities measured in this frame are marked with the prime sign), ν'_a can be determined by equating the un-absorbed source surface flux density, $F'_{\nu'_a}$, at ν'_a to a blackbody surface flux density with temperature T' in the Rayleigh-Jeans regime (see Appendix B for the

derivation; also see Sari & Piran 1999, Li & Song 2004, McMahon et al. 2006):

$$2kT'\frac{\nu_a'^2}{c^2} = C(\beta_1)F_{\nu_a'}' = \begin{cases} C_1(\beta_1)F_{\nu_p'}'\left(\frac{\nu_m'}{\nu_p'}\right)^{\beta_1}\left(\frac{\nu_a'}{\nu_m'}\right)^{\frac{1}{3}}, & \text{for } \nu_a' < \nu_m', \\ C_2(\beta_1)F_{\nu_p'}'\left(\frac{\nu_a'}{\nu_p'}\right)^{\beta_1}, & \text{for } \nu_m' < \nu_a' < \nu_p', \end{cases} \quad (5.3)$$

where $T' = \max(\gamma_a, \gamma_m)m_e c^2/k$, γ_a is the energy of electron whose characteristic emission frequency is ν_a' , and k is the Boltzmann constant. The numerical factors C_1 and C_2 are functions of β_1 only whose values range from 1.2 to 4.5 and from 1.2 to 7.0, respectively, for the range of observed β_1 values, but they have been neglected in previous works while we include them here.

Transforming the frequency to that measured in the observer's frame gives $\nu_a = \nu_a'\Gamma/(1+z)$, where z is the redshift of the GRB host galaxy. Measuring in the host comoving frame, the source has an isotropic luminosity of $4\pi R^2\Gamma^2 F_{\nu_p'}'\nu_p'$. This luminosity is also given by $4\pi D_L^2 f_{\nu_p}\nu_p$, where D_L is the luminosity distance of the GRB and f_{ν_p} is the observed peak flux density. Thus we have $F_{\nu_p'}' = f_{\nu_p}(D_L/R)^2/[\Gamma(1+z)]$. After applying these relations, Eq. (3) becomes

$$\begin{cases} \frac{C_1}{2}f_{\nu_p}\left(\frac{\nu_m}{\nu_p}\right)^{\beta_1}\left(\frac{\nu_a}{\nu_m}\right)^{\frac{1}{3}} &= m_e\gamma_m\nu_a^2\left(\frac{R}{D_L}\right)^2\frac{(1+z)^3}{\Gamma}, \\ &\text{for } \nu_a < \nu_m; \\ \frac{C_2}{2}f_{\nu_p}\left(\frac{\nu_a}{\nu_p}\right)^{\beta_1} &= m_e\gamma_a\nu_a^2\left(\frac{R}{D_L}\right)^2\frac{(1+z)^3}{\Gamma}, \\ &\text{for } \nu_m < \nu_a. \end{cases} \quad (5.4)$$

After substituting the electron's energy γ using the following relation between γ and the photon frequency ν ,

$$\gamma = \begin{cases} \left(\frac{2\pi m_e c}{eB}\right)^{\frac{1}{2}}\left(\frac{1+z}{\Gamma}\right)^{\frac{1}{2}}\nu^{\frac{1}{2}}, & \text{for synchrotron,} \\ \left(\frac{2\pi m_e c}{eB}\right)^{\frac{1}{4}}\left(\frac{1+z}{\Gamma}\right)^{\frac{1}{4}}\nu^{\frac{1}{4}}, & \text{for SSC,} \end{cases} \quad (5.5)$$

the self-absorption frequency is calculated as: for synchrotron

$$\nu_a = \begin{cases} \left(\frac{C_1}{2}\right)^{\frac{3}{5}} \times 10^{14.6-\frac{6}{5}\beta_1} f_{\nu_p}^{\frac{3}{5}} \nu_{p,19}^{-\frac{3}{5}\beta_1} \nu_{m,17}^{\frac{3}{5}\beta_1-\frac{1}{2}} \\ \quad \times \left(\frac{D_{L,28}}{1+z}\right)^{\frac{6}{5}} \left(\frac{\Gamma_{300}}{1+z}\right)^{\frac{9}{10}} B_5^{\frac{3}{10}} R_{14}^{-\frac{6}{5}} \text{ Hz} \\ \quad \text{if } \nu_a < \nu_m; \\ \left(\frac{C_2}{2}\right)^{\frac{1}{2.5-\beta_1}} \times 10^{\frac{38.5-19\beta_1}{2.5-\beta_1}} f_{\nu_p}^{\frac{1}{2.5-\beta_1}} \nu_{p,19}^{\frac{-\beta_1}{2.5-\beta_1}} \\ \quad \times \left(\frac{D_{L,28}}{1+z}\right)^{\frac{2}{2.5-\beta_1}} \left(\frac{\Gamma_{300}}{1+z}\right)^{\frac{1.5}{2.5-\beta_1}} B_5^{\frac{1}{5-2\beta_1}} R_{14}^{\frac{-2}{2.5-\beta_1}} \text{ Hz} \\ \quad \text{if } \nu_m < \nu_a < \nu_p \end{cases} \quad (5.6)$$

and, for SSC

$$\nu_a = \begin{cases} \left(\frac{C_1}{2}\right)^{\frac{3}{5}} \times 10^{15-\frac{6}{5}\beta_1} f_{\nu_p}^{\frac{3}{5}} \nu_{p,19}^{-\frac{3}{5}\beta_1} \nu_{m,17}^{\frac{3}{5}\beta_1-\frac{7}{20}} \\ \quad \times \left(\frac{D_{L,28}}{1+z}\right)^{\frac{6}{5}} \left(\frac{\Gamma_{300}}{1+z}\right)^{\frac{3}{4}} B_5^{\frac{3}{20}} R_{14}^{-\frac{6}{5}} \text{ Hz} \\ \quad \text{if } \nu_a < \nu_m; \\ \left(\frac{C_2}{2}\right)^{\frac{1}{2.25-\beta_1}} \times 10^{\frac{35-19\beta_1}{2.25-\beta_1}} f_{\nu_p}^{\frac{1}{2.25-\beta_1}} \nu_{p,19}^{\frac{-\beta_1}{2.25-\beta_1}} \\ \quad \times \left(\frac{D_{L,28}}{1+z}\right)^{\frac{2}{2.25-\beta_1}} \left(\frac{\Gamma_{300}}{1+z}\right)^{\frac{1.25}{2.25-\beta_1}} B_5^{\frac{1}{9-4\beta_1}} R_{14}^{\frac{-2}{2.25-\beta_1}} \text{ Hz} \\ \quad \text{if } \nu_m < \nu_a < \nu_p. \end{cases} \quad (5.7)$$

In the results above, the flux density, e.g., f_{ν_p} , is in units of mJy, $\Gamma = 300 \times \Gamma_{300}$ and the convention $Q = Q_n \times 10^n$, e.g., $\nu = \nu_{19} \times 10^{19}$ Hz and $B = B_5 \times 10^5$ Gauss, is used for other quantities; the same notations will be used in the rest of the chapter. In the following, our discussion will be based on the synchrotron radiation only. But for the use of reference the expression of ν_a for SSC is also given here.

5.3 The one-spectral-component assumption

In this work, we make an assumption that for the two samples (see Section 5.5 for a description of the sample selection criteria) studied, the optical and γ /X-ray photons belong to a same synchrotron continuum spectrum generated by a same group of hot electrons. This assumption is based on the following three considerations. First, GRB prompt γ /X-ray emission is often interpreted as synchrotron radiation of a group of non-thermal electrons.

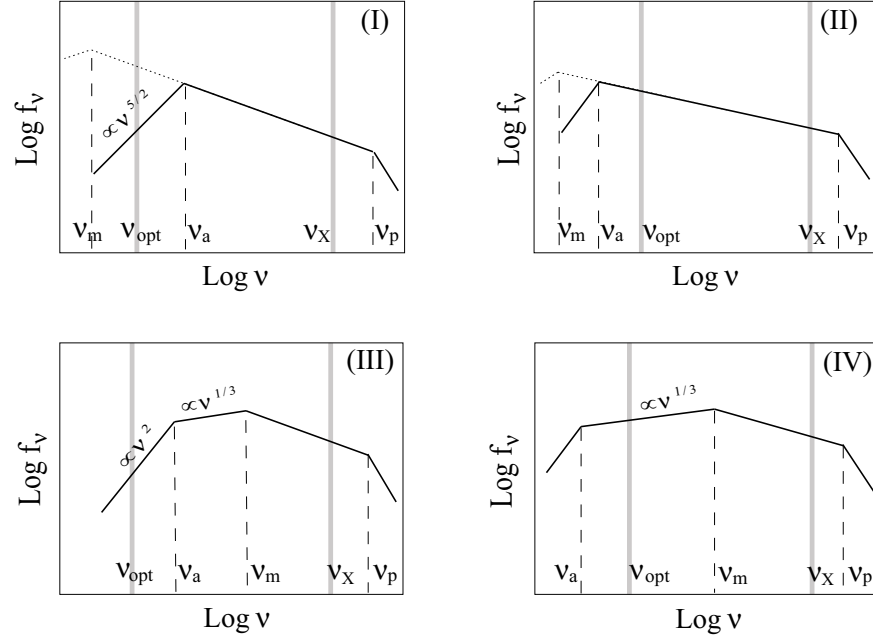


Figure 5.1: The four cases of the broad-band synchrotron spectrum of the GRB prompt emission discussed in the text. The broken power law shape around ν_p is phenomenologically derived from the observed γ -ray spectrum in GRBs; for its possible theoretical origins see Section 5.2. ν_a is the self absorption frequency. The dotted line in the two top panels is the low energy part of the spectrum when the self absorption is not considered. The two grey vertical bars mark the positions of ν_{opt} and ν_X , respectively. $\nu_X = 0.3$ keV is the lower end of the Swift XRT band pass.

If that is the case, the synchrotron spectrum *must* have a continuum extending to the low-frequency regime up to the optical band, presumably with a gentle slope of $f_\nu \propto \nu^{1/3}$ unless it has a self-absorption break. Secondly, the optical flux density is expected to always lie below or near the extrapolation from the γ -ray spectrum. This is generally consistent with observations in our sample (see Section 5.5 below and Figure 5.2). Finally, a temporal correlation between the optical flux variation and the γ -ray light curve (LC) is observed for the four GRBs in the our sample, suggesting the two components likely have the same dynamical origin. This is the major supporting evidence for our assumption.

We notice that there are other scenarios on prompt γ /optical emission that have been discussed in the literature. These include the synchrotron + SSC model (Kumar & Panaitescu 2008; Racusin et al. 2008), the models invoke different emission radii for optical and γ -ray emissions (Li & Waxman 2008; Fan et al. 2009), and the model invokes two shock regions at a same emission radius (Yu et al. 2009). These models are relevant to GRB 080319B, which clearly requires a separate spectral component to interpret the prompt optical emission. For most other bursts studied in this work, although these models are not ruled out, they are not demanded by the data. Our simple one-component model is adequate to interpret these bursts, and we will hereafter adopt this one-component assumption.

5.4 Deriving R constraints from ν_a and SED

Let us consider the synchrotron emission as the prompt emission mechanism. Depending on the locations of ν_m and ν_a , the ratio of the optical flux density to the flux density at ν_p is given for four different spectral cases by

$$\frac{f_{\nu_{opt}}}{f_{\nu_p}} = \begin{cases} \left(\frac{\nu_a}{\nu_p}\right)^{\beta_1} \left(\frac{\nu_{opt}}{\nu_a}\right)^{\frac{5}{2}}, & \text{if } \nu_m < \nu_{opt} < \nu_a - \text{case I,} \\ \left(\frac{\nu_{opt}}{\nu_p}\right)^{\beta_1}, & \text{if } \nu_m < \nu_a < \nu_{opt} - \text{case II,} \\ \left(\frac{\nu_m}{\nu_p}\right)^{\beta_1} \left(\frac{\nu_a}{\nu_m}\right)^{\frac{1}{3}} \left(\frac{\nu_{opt}}{\nu_a}\right)^2, & \text{if } \nu_{opt} < \nu_a < \nu_m - \text{case III,} \\ \left(\frac{\nu_m}{\nu_p}\right)^{\beta_1} \left(\frac{\nu_{opt}}{\nu_m}\right)^{\frac{1}{3}}, & \text{if } \nu_a < \nu_{opt} < \nu_m - \text{case IV.} \end{cases} \quad (5.8)$$

Figure 5.1 illustrates these four spectral cases. There is also a variation of case III (let us call it case III.5): $\nu_{opt} < \nu_m < \nu_a$, for which the flux density ratio is $f_{\nu_{opt}}/f_{\nu_p} =$

$(\nu_a/\nu_p)^{\beta_1}(\nu_m/\nu_a)^{5/2}(\nu_{opt}/\nu_m)^2$. We will come back to this case later and show that it is almost exactly the same as case III. In some GRBs simultaneous observations of prompt X-ray and γ -ray emissions are made. The X-ray spectrum corrected for the photo-absorption in the soft end always nicely matches the power law extrapolated from γ -ray spectrum below ν_p , without a need to invoke a break (e.g. Cenko et al. 2006; Romano et al. 2006; Page et al. 2007). This requires that both ν_a and ν_m be smaller than $\nu_X = 0.3$ keV, the lower end of the Swift XRT band pass. We take this as a constraint in our analyses.

We aim to constrain R based on the spectral information, such as f_{ν_p} , $f_{\nu_{opt}}$ and β_1 , using ν_a as a proxy. We know from Section 5.2 that ν_a is expressed in terms of f_{ν_p} , ν_m and R . So for each spectral case, we substitute the appropriate ν_a expression into the flux density ratio equation or into the constraint on ν_a implied by the definition of that spectral case (Eq. 8), and then get the R constraints.

For case I, substituting ν_a and letting $\nu_{opt} = 5 \times 10^{14}$ Hz (for R band), we have

$$R_{14} = 7.5 \times \left(\frac{C_2}{2}\right)^{\frac{1}{2}} f_{\nu_{opt}}^{\frac{1}{2}} \frac{D_{L,28}}{(1+z)} B_5^{\frac{1}{4}} \left(\frac{\Gamma_{300}}{1+z}\right)^{\frac{3}{4}}. \quad (5.9)$$

There is also a justification criterion due to the case definition $\nu_a > \nu_{opt}$, where ν_a is directly determined from the flux density ratio in Eq. (8) by

$$\nu_a = 10^{(19 - \frac{12.2}{2.5 - \beta_1})} \left(\nu_{p,19}^{-\beta_1} \frac{f_{\nu_p}}{f_{\nu_{opt}}} \right)^{\frac{1}{2.5 - \beta_1}} \text{ Hz}. \quad (5.10)$$

For case II, the flux density ratio does not depend on ν_a and hence on R . One justification criterion for this case is that the spectral slope from the optical to the X- or γ -rays has to be consistent with β_1 , i.e., $\beta_{opt-X/\gamma} = \beta_1$. Another criterion due to the case definition is $\nu_a < \nu_{opt}$. Substituting with the expression of ν_a , the latter gives

$$R_{14} > 7.5 \times \left(\frac{C_2}{2}\right)^{\frac{1}{2}} \times (2.2)^{\beta_1} \times 10^{-2.5\beta_1} \times \nu_{p,19}^{-\frac{\beta_1}{2}} f_{\nu_p}^{\frac{1}{2}} \frac{D_{L,28}}{(1+z)} B_5^{\frac{1}{4}} \left(\frac{\Gamma_{300}}{1+z}\right)^{\frac{3}{4}}. \quad (5.11)$$

For case III, when substituting the appropriate ν_a expression in Eq. (6) into the flux

density ratio relation, it gives the expression of R in

$$R_{14} = 2.0 \times \left(\frac{C_1}{2}\right)^{\frac{1}{2}} \nu_{m,17}^{-\frac{1}{4}} f_{\nu_{opt}}^{\frac{1}{2}} \frac{D_{L,28}}{(1+z)} B_5^{\frac{1}{4}} \left(\frac{\Gamma_{300}}{1+z}\right)^{\frac{3}{4}}. \quad (5.12)$$

We find for case III.5 that the R expression — obtained by substituting the appropriate ν_a expression into Eq.(8) — is exactly the same as Eq. (12) except that C_1 is replaced with C_2 . We find the ratio C_2/C_1 lies in the range of (1, 1.6) for $\beta_1 = (-1.4, 0)$ (see in Appendix B).

According to the definition of case III, $\nu_{opt} < \nu_m < \nu_X$. Plugging this constraint of ν_m into Eq. (12) and its counterpart equation for case III.5, it gives

$$2.1 \times \left(\frac{C_1}{2}\right)^{\frac{1}{2}} f_{\nu_{opt}}^{\frac{1}{2}} \frac{D_{L,28}}{(1+z)} < R_{14} B_5^{-\frac{1}{4}} \left(\frac{1+z}{\Gamma_{300}}\right)^{\frac{3}{4}} < 7.5 \times \left(\frac{C_2}{2}\right)^{\frac{1}{2}} f_{\nu_{opt}}^{\frac{1}{2}} \frac{D_{L,28}}{(1+z)}. \quad (5.13)$$

Note that in writing this constraint we already combined the one for case III with the one for case III.5. It is done by using C_1 in the lower limit and C_2 in the upper limit, such that the combined constraint is conservative. From now on we expand the case III definition to be $\nu_{opt} < \min(\nu_a, \nu_m)$ so that it includes case III.5.

Two last pieces of constraining information for case III are from ν_a , i.e., $\nu_a(f_{\nu_p}, \beta_1, R) < \nu_X$ and $\nu_a(f_{\nu_p}, \beta_1, \nu_m, R) > \nu_{opt}$, where we use the expressions for ν_a given in Eq. (6); the first ν_a expression is for the situation of $\nu_m < \nu_a$ and the second for the situation of $\nu_a < \nu_m$. The first constraint gives

$$R_{14} B_5^{-\frac{1}{4}} \left(\frac{1+z}{\Gamma_{300}}\right)^{\frac{3}{4}} > \left(\frac{C_2}{2}\right)^{\frac{1}{2}} \times (0.85)^{1+\beta_1} \times 10^{-1.75-\beta_1} f_{\nu_p}^{\frac{1}{2}} \nu_{p,19}^{-\frac{\beta_1}{2}} \left(\frac{D_{L,28}}{1+z}\right). \quad (5.14)$$

The ν_a expression in the second constraint, $\nu_a > \nu_{opt}$, contains ν_m which can be expressed in terms of $f_{\nu_{opt}}$ and R from the R -expression for this spectral case. After substituting for ν_m , the second constraint gives

$$R_{14} B_5^{-\frac{1}{4}} \left(\frac{1+z}{\Gamma_{300}}\right)^{\frac{3}{4}} > \left(\frac{C_1}{2}\right)^{\frac{1}{2}} \times 2.0 \times \left[2.4 \times 10^{\beta_1} \left(\frac{f_{\nu_{opt}}}{f_{\nu_p}}\right)^{\frac{1}{2}} \nu_{p,19}^{\frac{\beta_1}{2}}\right]^{\frac{1}{2/3-2\beta_1}} f_{\nu_{opt}}^{\frac{1}{2}} \frac{D_{L,28}}{(1+z)}. \quad (5.15)$$

Here the constraint $\nu_a > \nu_{opt}$ gives a lower limit of R , contrary to what is inferred from the

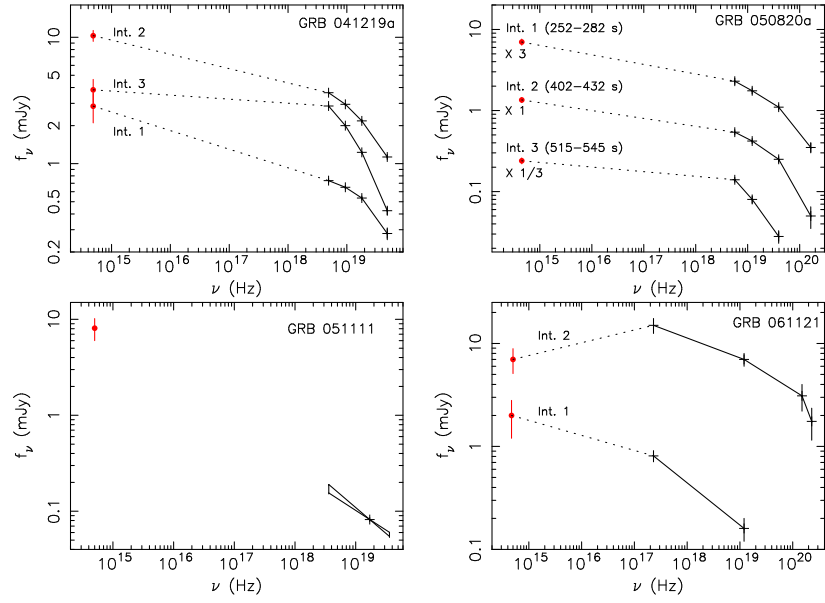


Figure 5.2: Observed optical to γ /X-ray broadband spectra for the 4 GRBs in our prompt optical detection sample. The dotted line is a line connecting the optical and the lowest energy γ /X-ray data points. For GRB 051111, only one γ -ray data point is shown, superposed with the single-power-law fitted spectral index and its confidence range. Adapted from Vestrand et al. (2005), Vestrand et al. (2006), Yost et al. (2007a) and Page et al. (2007), respectively.

conventional relation between ν_a and R . It is because in this subtle occasion ν_a depends not only on R but also on ν_m , and ν_m is expressed in terms of the optical flux density and R , hence the combined R -dependence of ν_a is positive.

The final constraint for case III should be the overlapping region among those three constraints obtained.

For case IV, ν_m can be obtained from the flux density ratio relation by

$$\nu_{m,17} = \left[6 \times 10^{2\beta_1} \left(\frac{f_{\nu_{opt}}}{f_{\nu_p}} \right) \nu_{p,19}^{\beta_1} \right]^{\frac{1}{\beta_1 - 1/3}}, \quad (5.16)$$

whose value will be used to justify the case definition $\nu_{opt} < \nu_m < \nu_X$. Another constraint from the case definition is $\nu_a(f_{\nu_p}, \beta_1, \nu_m, R) < \nu_{opt}$. Substituting with the ν_m expression, this gives

$$R_{14} B_5^{-\frac{1}{4}} \left(\frac{1+z}{\Gamma_{300}} \right)^{\frac{3}{4}} > \left(\frac{C_1}{2} \right)^{\frac{1}{2}} \times 2.0 \times \left[2.4 \times 10^{\beta_1} \left(\frac{f_{\nu_{opt}}}{f_{\nu_p}} \right)^{\frac{1}{2}} \nu_{p,19}^{\frac{\beta_1}{2}} \right]^{\frac{1}{2/3 - 2\beta_1}} f_{\nu_{opt}}^{\frac{1}{2}} \frac{D_{L,28}}{(1+z)}. \quad (5.17)$$

Notice that two contrary constraints, $\nu_a > \nu_{opt}$ in case III and $\nu_a < \nu_{opt}$ in case IV, give exactly the same constraints on R . This is because the ν_a expression in both cases contains R and ν_m , but in case III ν_m is a strong function of R , $\propto R^{-4}$, while in case IV ν_m is a function of the flux density ratio only. Thus in case III the R -dependence is reversed between two sides of the inequality relation $\nu_a > \nu_{opt}$.

To summarize, the overall constraints on R are: Eq. (9) for case I, Eq. (11) for case II, Eq. (13-15) for case III and Eq. (17) for case IV. In addition, when they are available, the calculated ν_a or ν_m must satisfy the case definitions.

If the optical flux density has only an upper limit, the above R -constraints must be taken with a conservative point of view wherever $f_{\nu_{opt}}$ is involved. Let $f_{\nu_{opt}}$ represent the measured upper limit. For case I, Eq. (9) will give an upper limit for R . For case II, Eq. (11) remains. For case III, Eq. (13) is left with only the upper limit of R , Eq. (14) remains and Eq. (15) is useless. For case IV, Eq. (16) gives a lower limit of ν_m which can be used to justify the case definition; Eq. (17) is useless. But we recall that Eq. (17) is obtained by substituting the ν_m expression into the definition constraint $\nu_a(f_{\nu_p}, \beta_1, \nu_m, R) < \nu_{opt}$. Here, instead of using the ν_m expression, we plug in the upper boundary of ν_m : $\nu_m < \nu_X$, then a

new lower limit of R is obtained for case IV:

$$R_{14}B_5^{-\frac{1}{4}}\left(\frac{1+z}{\Gamma_{300}}\right)^{\frac{3}{4}} > \left(\frac{C_1}{2}\right)^{\frac{1}{2}} \times 0.94 \times (0.85)^{\beta_1} \times 10^{-\beta_1} f_{\nu_p}^{\frac{1}{2}} \nu_{p,19}^{-\frac{\beta_1}{2}} \left(\frac{D_{L,28}}{1+z}\right). \quad (5.18)$$

5.5 GRB data sample

Now we turn to the real GRB data to which our method developed above can be applied. First we construct a small sample of GRBs whose prompt optical emission is not only detected but is also variable and temporally correlated with the γ -rays. Excluding GRB 080319B that requires a new spectral component for optical emission, we identify four of GRBs in the sample, all belonging to the long-duration class. Three of them show complex fluctuations in their prompt γ -ray and optical LCs while the fourth is a single, smoothly peaked event, so we utilize multiple time intervals for each of the three. The emission properties of each time interval are listed in Table 1.

GRB 041219A is a very long ($T_{dur} \sim 500$ s) burst and has multiple peaks in γ -ray LC. It has three optical detection intervals; the first two are correlated with the first γ -ray peak and the third with the second γ -ray peak (Vestrand et al. 2005).

GRB 050820A is a similar one except that it has denser optical temporal coverage. Its optical LC is decomposed into two components : a smooth component with fast rise and power-law decay, and a strongly variable component superposed on it (Vestrand et al. 2006). The smooth component is well accounted for by the early afterglow due to the GRB outflow interacting with the ambient medium. The variable component is found to correlate with the γ -ray peaks, suggesting it has the same origin as the γ -rays. In Table 1 the optical emission properties for this burst are for the residual optical component after subtracting the smooth component.

GRB 051111 has a single FRED (fast rise and exponential decay) peak in γ -rays lasting ~ 90 s. The first optical observation starts at 30 s after the burst trigger when the γ -ray LC began to decay (Yost et al. 2007a). The prompt optical LC (before the γ -rays die off) decays more steeply than that of the later optical afterglow emission. The prompt optical emission has an excess above the back extrapolation of the later optical afterglow component. It has a decay slope statistically compatible with that of the γ -ray LC, and

its flux density is also compatible with the spectral extrapolation of the γ -rays (Yost et al. 2007a). This is good evidence that the prompt optical excess has the same origin as the γ -rays. We use the flux density of the excess - not the total - optical emission in the first optical observation time interval.

GRB 061121 has two separate γ -ray peaks. The last peak was caught by XRT, UVOT and ROTSE, and it appears in LCs in all bands (Page et al. 2007). We use the emission properties of two time intervals of the last peak, one during the rising phase, and the other just at the peak.

We show the SEDs for all time intervals of the 4 GRBs in Figure 5.2 using the data adapted from their original publications. Two SEDs show almost no break between the optical and the γ -rays (corresponding to the theoretical spectrum case II) or a break very close to the optical. In all other cases, at least one break is needed between the optical and the γ -rays bands. The break(s) could be ν_a , ν_m , or both.

Besides this first data sample for optical detections, we also define a second data sample which is composed of those optically “dark” GRBs during the prompt phase. This sample is adopted from Yost et al. (2007a), who reported the bursts whose prompt phase was observed by ROTSE but only upper limits on the optical flux were retrieved. Each burst has either a single or multiple time intervals of ROTSE exposure during the prompt phase. For bursts with multiple optical time intervals, we use the interval which has the smallest measurement error in the γ -ray flux density f_{ν_p} - usually the interval that has the brightest γ -ray flux. The only exception is GRB 061222A, for which three time intervals are used. This is because all the three intervals are located at the brightest part of the γ -ray LC. They all have small errors in f_{ν_p} , and the instantaneous γ -ray spectral index β_1 are available for all three intervals. The motivation of selecting this sample is the following: Even if there is no direct detection of prompt optical emission, one can speculate the existence of a prompt optical emission component that tracks the γ -ray LCs, which is the spectral extension of the prompt γ -ray spectrum into the optical band. The flux level of this component must be fainter than the upper limit set by the ROTSE observations. We want to check whether inferred R constraints of this sample is consistent with the sample with optical detection, and whether the non-detection of optical emission of this sample is

due to stronger synchrotron self absorption associated with a smaller R .

5.6 Results

We apply the constraints on R derived in Section 5.4 to the first sample with prompt optical detections. The results for all four broad-band spectral cases are listed in Table 1. For most bursts in the sample, case II can be immediately ruled out because usually $\beta_{opt-X} > \beta_1$. Case IV is also ruled out for some bursts because the calculated ν_m is $\gg 0.3$ keV. For GRB 041219A, case I can be ruled out for its first time interval because the case definition is not satisfied by the calculated ν_a . Actually this interval is consistent with case II, i.e., the optical intensity is consistent with the simple power-law extrapolation from the γ -ray spectrum.

We plot the permitted R -ranges for each observation time interval in the sample for all possible spectral cases as floating bars in Figure 5.3. The observed optical to γ -ray SED restricts ν_a from being much larger than ν_{opt} . Accordingly, the results in Figure 5.3 give a constraint on the emission site for most time intervals of this sample: $R \geq$ a few $\times 10^{14} \Gamma_{300}^{3/4} B_5^{1/4}$ cm. For two time intervals (041219A Int. 3 and 050820A Int. 3) in the sample, some spectral cases can be ruled out, thus the R -constraint can be pinned down to $R \approx (10^{14} - 10^{15}) \Gamma_{300}^{3/4} B_5^{1/4}$ cm.

Similar results for the sample with only prompt optical upper limits are plotted in Figure 5.4. In about half (6/13) of the sample a heavy self absorption, i.e. large ν_a , is needed to account for the optical deficit, corresponding to the spectral case I and III, which implies a constraint of $R < 10^{15} \Gamma_{300}^{3/4} B_5^{1/4}$ cm. For the remaining half (7/13) of the sample, a spectral break at ν_m which is below ν_X but is much larger than ν_{opt} alone can give rise to the required deficit in optical, while ν_a can keep being smaller than ν_{opt} , corresponding to case IV. Thus for this half of the sample, we can provide no constraint on ν_a and hence on R .

Comparing Figure 5.4 with Figure 5.3, we find that there are always overlapping regions between the permitted R -ranges for the two samples. Therefore we can *not* draw any statistically significant distinction between these two samples as regards the constraints

Table 1: Constraints on the emission site radius for GRBs in which a prompt optical component temporally correlated with the γ -ray emission is present. f_{ν_p} and β_1 are the BAT flux density and the BAT spectral index, respectively; they are determined directly from the same time interval as that of the optical observation. A $H_0 = 71$, $\Omega_\Lambda = 0.73$, $\Omega_M = 0.27$ universe is assumed. For GRBs without a known redshift, $z = 2$ is assumed. The “\” symbol means the SED is apparently inconsistent with, or the derived ν_a or ν_m violates, the spectral case definition, thus the corresponding spectral case is ruled out. Spectral case (II) is ruled out for the most of the sample because β_1 is much steeper than $\beta_{opt-X/\gamma}$.

time int. (s)	z	$f_{\nu_{opt}}$ (mJy)	ν_p (10^{19} Hz)	f_{ν_p} (mJy)	β_1	Ref.*	R ($10^{14} \Gamma_{300}^{3/4} B_5^{1/4}$ cm)				ν_a (eV) (I)	ν_m (eV) (IV)
							(I)	(II)	(III)	(IV)		
041219A	203 - 275	3	1	0.65	-0.16		8.7	> 9.0	(8.1, 8.7)	> 8.1	2	2.2
	288 - 318	10	1	3	-0.32	1	18.4	\	(8.0, 18.4)	> 8.0	4	40
	330 - 403	4	1	2	-0.64		14.4	\	(3.5, 14.4)	> 3.0	12	660
050820A	252 - 282	7.3	1.6	0.56	-0.3		15.5	> 20	(12, 15.5)	> 12	2.4	4.7
	402 - 432	1.3	1.6	0.4	-0.3	2	6.5	\	(2.8, 6.5)	> 2.8	4	42
	515 - 545	0.25	2.6	0.13	-0.7		3.7	\	(0.9, 3.7)	> 0.6	18	1700
051111	32 - 32	8.2	1.7	0.08	-0.48	3, 4	18	> 22	(14.5, 18)	> 14.5	2.3	3.2
061121	56 - 56	1.8	1.2	0.14	-0.42	5	7.8	\	(4.1, 7.8)	> 4.1	3.5	19
	76 - 76	7	1.2	7	-0.21		13	\	(4.7, 13)	> 4.7	4.3	97

* 1: Vestrand et al. (2005); 2: Vestrand et al. (2006); 3: Yost et al. (2007a); 4: Hill et al. (2005); 5: Page et al. (2007).

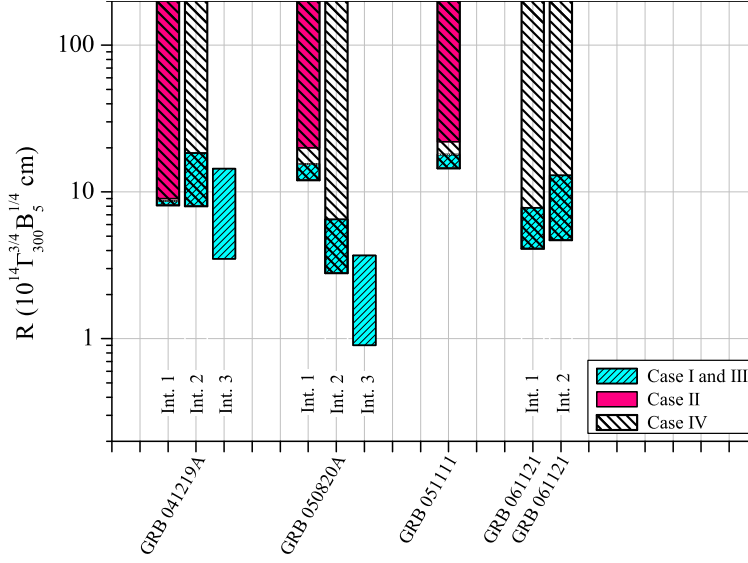


Figure 5.3: The constraints on the emission radii for four GRBs with prompt optical detections. For 3 bursts of the sample, more than one time intervals per burst are used. Based on the emission spectral information of individual bursts or time intervals, spectral case II and IV, respectively, are already ruled out for minor parts of the sample. See details in Table 1.

on their emission sites.

5.6.1 The dependence of results on Γ and B

Strictly speaking, the constraint on R is dependent on the source LF Γ and the magnetic field strength B . Independent determinations of Γ and B for each GRB in our sample are not easy. So in this work we adopt the theoretically anticipated values in the standard internal-shock model: $\Gamma \approx 300$, $B \approx 10^5$ G. In the following we will justify these adopted values based on the available information of the GRBs in our sample.

Constraints on Γ

Recently Molinari et al. (2007) inferred $\Gamma \approx 400$ for two GRBs by directly observing the deceleration time of the GRB outflow. This value is in agreement with what we adopt. In addition, here we present some attempts to estimate Γ for each GRB in our first sample (with optical detections) using three independent arguments, which suggests that the choice

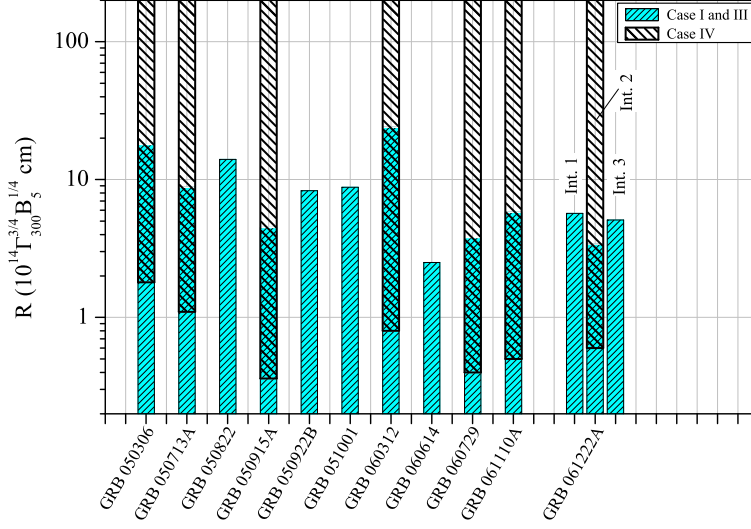


Figure 5.4: The constraints on the emission radii for GRBs without prompt optical detection. GRB 061222A has three time intervals that have information available for our calculation. Based on the emission spectral information, spectral case II is already ruled out for the whole sample, and spectral case IV is ruled out for about half of the sample. For eight bursts without known redshift, $z = 2$ is assumed.

Table 5.2: The Γ constraints from the requirement that the photon annihilation optical depth $\tau_{\gamma\gamma} < 1$. A $H_0 = 71$, $\Omega_\Lambda = 0.73$, $\Omega_M = 0.27$ universe is assumed. For the GRB without known redshift, $z = 2$ is assumed.

GRB	time int. (s)	z	δT (s)	N_1^*	α	e_{max} (MeV)	$e_{max,an}$ (Γ_2^2 MeV)	Ref.*	Γ
041219A	203 - 275	(2)	15	0.15	1.80	0.2	1450	1	> 56
	288 - 318	(2)	5	0.56	1.75	0.2	1450		> 93
	330 - 403	(2)	2	0.10	2.15	0.2	1450		> 49
050820A	252 - 282	2.6	15	0.30	2.52	1.2	168	2	> 53
	402 - 432	2.6	15	0.063	2.00	0.5	403		> 53
	515 - 545	2.6	10	0.015	1.96	0.25	806		> 41
051111	32 - 32	1.55	8	0.035	1.48	0.15	2680	3	> 65
061121	76 - 76	1.3	1	2.7	< 2.9	1.4	359	4	> 53

* In units of $\text{s}^{-1}\text{cm}^{-2}\text{MeV}^{-1}$.

* 1: Vestrand et al. (2005); 2: Cenko et al. (2006); 3: Yost et al. (2007a); 4: Page et al. (2007).

Table 5.3: The Γ constraints derived from the deceleration time t_{dec} constraints for ISM and Wind medium, respectively. A $H_0 = 71$, $\Omega_\Lambda = 0.73$, $\Omega_M = 0.27$ universe is assumed. For the GRB without known redshift, $z = 2$ is assumed. For GRB 041219A the inferred t_{dec} -constraint is very loose, partly because of a lack of X-ray afterglow observation, and also because the early infrared light curve ($t \leq 6 \times 10^3$ s) is highly variable, possibly of internal shock origin, which makes it difficult to infer t_{dec} to be these earlier times. In the cited reference for GRB 061121, only $E_{\gamma,iso}$ is given, without giving the γ -ray fluence.

GRB	z	t_{dec} (s)	F_γ^*	$E_{\gamma,iso}$ (10^{53} erg)	Ref.*	Γ ($\eta_{\gamma,0.2}^{-1/8} n^{-1/8}$)	Γ ($\eta_{\gamma,0.2}^{-1/4} A_*^{-1/4}$)
041219A	(2)	$< 3 \times 10^4$	15.5	15.2	1	> 73	> 33
050820A	2.6	< 500	5.3	8.3	2, 3	> 337	> 81
051111	1.55	< 100	0.39	0.24	4	> 349	> 46
061121	1.3	< 200	–	2.8	5	> 352	> 70

* γ -ray fluence, in units of 10^{-5} erg cm^{-2} .

* 1: Vestrand et al. (2005); 2: Vestrand et al. (2006); 3: Cenko et al. (2006); 4: Yost et al. (2007a); 5: Page et al. (2007).

of $\Gamma \approx 300$ is reasonable.

(1) The variability time scale argument. For the standard scenario in which the variability time scale is that of the central engine and that the ejecta form a conical jet with opening angle much larger than $1/\Gamma$, the observed variability time scale should be at least the angular spreading time. This gives the constraint

$$\Gamma > 41[R_{14}(1+z)/\delta T]^{1/2}, \quad (5.19)$$

where δT is the observed variability time scale, defined as the rising or decaying time scale of the pulses in the LC. From the data we find that δT is $\approx 1 - 15$ s for our sample. The Γ -constraint from this argument is rather weak compared with the other two constraints described below.

(2) The photon annihilation opacity argument. A GRB releases a huge amount of energy ($\sim 10^{53}$ erg isotropically) in terms of high energy photons from a small volume, which are subject to the photon-photon annihilation (e.g. Baring & Harding 1997; Lithwick & Sari 2001). Suppose e_{max} is the maximum photon energy detected in the burst, the fact that a single power-law or a piece-wise power-law spectrum is detected for most GRBs up

to e_{max} implies that the optical depth of photon-photon pair production $\tau_{\gamma\gamma}$ for the photons of energy e_{max} is smaller than unity. $\tau_{\gamma\gamma}$ is related to the total number of photons and the size of the emission region, the latter of which can be expressed in terms of Γ and δT within the internal shock model. Thus this requirement can impose a lower limit on Γ within the internal shock model. More generally the opacity argument can give a constraint in the $R - \Gamma$ space (Gupta & Zhang 2008; Murase & Ioka 2008; Zhang & Pe’er 2009). Our following treatment applies to the internal shock model that is commonly discussed in the literature.

The minimum photon energy at which the photons are able to annihilate with photons of energy e_{max} is:

$$e_{max,an} = \frac{(\Gamma m_e c^2)^2}{e_{max}(1+z)^2}. \quad (5.20)$$

The power-law form spectrum just below e_{max} is described as in

$$N(e) = N_1 \left(\frac{e}{\text{MeV}} \right)^{-\alpha}, \quad (5.21)$$

where e is the detected photon energy, $N(e)$ – in units of $[\text{s}^{-1}\text{cm}^{-2}\text{MeV}^{-1}]$ – is the number of photons detected per unit time per unit area per unit energy at e , N_1 is equal to $N(e)$ at $e = 1$ MeV, and α is the photon index.

We followed the formulae of Lithwick & Sari (2001) in their Limit A case to calculate the lower limit of Γ due to $\tau_{\gamma\gamma} < 1$ for our optical detection sample. The results, as well as the observational properties that are used, are summarized in Table 5.2. Note that for all bursts in the sample, $e_{max,an} \gg e_{max}$ for reasonable values of Γ (e.g., $\sim 10^2$). Thus our calculation has implicitly assumed that the power-law form spectrum detected below e_{max} would actually extend well beyond e_{max} and up to $e_{max,an}$, which is usually below the detector’s limited bandpass. More rigorous calculations require the knowledge of the spectral shape below peak energy of the spectrum (Gupta & Zhang 2008). However, the optical depth is much more sensitive to Γ than the spectral indices, and the derived Γ constraint is not significantly modified by performing the more rigorous treatment. The above treatment is adequate to serve our purpose.

(3) The deceleration time constraint. In the well established external shock model

for GRB afterglows (e.g., Mészáros & Rees 1997; Sari, Piran & Narayan 1998; Chevalier & Li 2000; see Piran 2005 for a review), the onset of afterglow marks the time, as known as the deceleration time t_{dec} , when one half of the total kinetic energy of the GRB outflow E_k is deposited to the shocked circumburst medium. The afterglow light curve should rise before t_{dec} and decay in a power law with time after t_{dec} (e.g., Molinari et al. 2007). The deceleration time t_{dec} is determined by E_k , outflow bulk LF Γ and the density of the circumburst medium, either a constant density medium [interstellar medium (ISM)] or a wind-like medium [$\rho(R) = A \times R^{-2}$]:

$$t_{dec} = \begin{cases} \left(\frac{3E_{k,iso}}{64\pi n m_p c^5 \Gamma^8} \right)^{1/3} (1+z), & \text{for ISM,} \\ \frac{E_{k,iso}(1+z)}{16\pi A c^3 \Gamma^4}, & \text{for Wind,} \end{cases} \quad (5.22)$$

where n is the proton number density of the ISM medium, and $A = 5 \times 10^{11} A_* \text{ g cm}^{-1}$ is the Wind medium density normalization parameter. The isotropic equivalent kinetic energy $E_{k,iso}$ can be related to the isotropic energy release in γ -ray radiation $E_{\gamma,iso}$ by an energy conversion efficiency factor $\eta_\gamma = E_{\gamma,iso}/E_{k,iso}$.

The afterglow observations (X-rays and optical) for our sample show either a power law decay starting from the earliest observation interval or, a long-lasting shallow decay followed by a normal power law decay. It suggests that the afterglow onsets should be earlier than the start of the single power law decay or the start of the shallow decay. One can use the first observation data in the decaying afterglow phase to constraint the deceleration time to be earlier than the observational epoch (e.g., Zhang et al. 2006). From the data, we find the deceleration time $t_{dec} < 3 \times 10^4 \text{ s}$ for GRB 041219a, and $t_{dec} < 100 - 500 \text{ s}$ for the other 3 GRBs (050820a, 051111, 061121). Assuming $\eta_\gamma = 0.2$, $n = 1 \text{ cm}^{-3}$ and $A_* = 1$, we find: for ISM, $\Gamma > 73$ for 041219a, $\Gamma \gtrsim 350$ for the other 3 GRBs; for Wind, $\Gamma > 33$ for 041219a, $\Gamma \gtrsim 50$ for the other 3. The results are summarized in Table 5.3. We have checked of the compliance with closure relationships predicted by the external shock models for these bursts during the afterglow phase. It turns out that two (GRB 050820A and 061121) out of the 4 GRBs are consistent with and in favour of the ISM environment scenario, while the other two are consistent with both scenarios and can not discriminate between them.

To summarize, with the available data, one can only constrain but cannot determine Γ of the GRBs in our sample. On the other hand, all three constraints derived from the data are consistent with $\Gamma = 300$ adopted in our calculations. In particular, the Γ -constraint derived from the argument (3), which is the most stringent one among the three arguments, indicate that the assumed value of $\Gamma = 300$ is reasonable.

Constraints on B

The B value in the emission region is a function of R . There are two possible origins of the magnetic field in the emission region. The first component is the global magnetic field entrained by the ejecta from the central engine. Let's assume $B \sim 10^{14}$ G at the central engine, a typical value for a fast rotating magnetar or a fast rotating black hole accretion disk system - the two most plausible GRB central engine candidates. The B value drops as R^{-2} with R up to the light cylinder, and then drops as R^{-1} thereafter (Goldreich & Julian 1969). Given that the central rotating source has a radius of $R_* \sim 10^6$ cm and a rotation period of $P \sim 1$ ms, at a radius $R \sim 10^{14}$ cm, the field that is carried within the outflow has a strength of $B \approx 2 \times 10^5 B_{*,14} R_{*,6}^2 P_{ms}^{-1} R_{14}^{-1}$ G.

The second B component is a random field generated *in-situ* in the emission region, likely in a relativistic shock via the Weibel instability (Medvedev & Loeb 1999). This random field also follows the same R -dependence and is of the same order as the engine-related B component if ϵ_B - the ratio of the post-shock magnetic energy density to the total energy density - is not too small (Zhang & Mészáros 2002).

One can also briefly estimate the local field strength by relating the GRB γ -ray peak photon energy, typically ~ 0.1 MeV, with the synchrotron characteristic frequency, $\nu_p = eB\gamma^2\Gamma/[2\pi m_e c(1+z)]$, where γ is the typical energy of electrons. In the internal-shock model, $\gamma = \epsilon_e f(p)(m_p/m_e)\theta_p$, where ϵ_e is the ratio of the electron energy density over the total thermal energy density in the post-shock fluid, $f(p) = (p-2)/(p-1)$ and p is the electron energy spectral index. The parameter θ_p is the fractional energy gain of a proton passing the shock which depends only on the relative LF between the fluids downstream and upstream. For internal shocks, θ_p is *not* dependent on the shell bulk LF Γ and is of the order of unity. For $\epsilon_e = 0.3$ and $p = 3$, we have $\gamma \approx 300$. Thus the required B value can be

estimated as $B \approx 5 \times 10^5 \Gamma_{300}^{-1} \gamma_{300}^{-2} (\frac{1+z}{2})$ G.

The three crude estimates are marginally consistent with each other. We have taken $B = 10^5 B_5$ G as the typical value throughout the text. Of course a large uncertainty exists due to our lack of understanding on the field properties, but it is reconciled by the very weak dependence of R on B (1/4 power).

5.6.2 Comparison with results from an alternative modelling approach

Kumar & McMahon (2008) developed a general method of modelling GRB's γ -ray emission properties. Their method considers the synchrotron and the SSC emission, respectively, as the radiation mechanism, takes into account the radiative cooling of electrons, and uses observed emission properties (such as the peak flux density and the pulse duration) to search for the allowed space of the model parameters such as R and Γ . Here we also apply their method for the synchrotron case to our optical detection sample using their code, and compare the results with ours. We add a new constraint into the module that controls the allowed model parameter space, which is that the optical flux density calculated from the model has to match the observed one within a $\pm 50\%$ range.

To use this detailed modelling method, we have to specify which standard synchrotron spectral regime a GRB emission interval is in. The spectral indices (β_1) of the optical detection sample in Table 1 have a variety of values around $-1/2$, based on which we classify the sample into 4 categories and apply the detailed modelling method accordingly. (1) For those time intervals that are most probably consistent with the $\beta_1 = -1/2$ regime (051111 and 061121 int. 1), this method gives $R \approx 10^{14} - 10^{16}$ cm. (2) For those possibly consistent with both $\beta_1 = -1/2$ and $\beta_1 = -(p-1)/2$ where $p > 2$ (041219A int. 3 and 050820A int. 3), the method in the $\beta_1 = -1/2$ regime gives $R \approx 10^{14} - 10^{15}$ cm, while in the $\beta_1 = -(p-1)/2$ regime it gives no allowed R -space — but if we relax the $f_{\nu_{opt}}$ constraint, it gives $R \approx 10^{17} - 10^{18}$ cm. (3) For those possibly consistent with both $\beta_1 = -1/2$ and $\beta_1 = -(p-1)/2$ where $1 < p < 2$ (041219A int. 2, 050820A int. 1 and 2), the method in the $\beta_1 = -1/2$ regime gives $R \approx 10^{14} - 10^{15}$ cm; however, the code provided by the authors is not applicable when $p < 2$. (4) The last category are those inconsistent with $\beta_1 = -1/2$ but probably consistent with $\beta_1 = -(p-1)/2$ if $1 < p < 2$ (041219A int. 1 and 061121 int.

2) for which the code is not applicable.

Overall, we find that for the major part of the optical detection sample where the detailed modelling method (Kumar & McMahon 2008) is applicable the allowed spaces for R from this method are about $10^{14} - 10^{16}$ cm. This is approximately consistent with the findings from our approach that R is \geq (a few $\times 10^{14} - 10^{15}$) $\Gamma_{300}^{3/4} B_5^{1/4}$ cm for most of the intervals in the sample, and $10^{14} \Gamma_{300}^{3/4} B_5^{1/4}$ cm $< R < 10^{15} \Gamma_{300}^{3/4} B_5^{1/4}$ cm for the remaining two intervals in the sample.

5.7 Conclusion and Discussions

Based on the assumption that the prompt optical and γ -ray emissions belong to the same synchrotron continuum of a group of hot electrons, we make constraints on the location of the prompt emission site for a sample of GRBs whose prompt optical emission is detected to temporally tracking the γ -ray LCs, by determining the location of ν_a in their SED. Our analysis shows that for most of the intervals in this sample the distance of the prompt emission site from the explosion centre R is \geq (a few $\times 10^{14} - 10^{15}$) $\Gamma_{300}^{3/4} B_5^{1/4}$ cm, and for the remaining two intervals, the emission site is $(10^{14} - 10^{15}) \Gamma_{300}^{3/4} B_5^{1/4}$ cm away from the explosion centre.

The dependence of the distance constraint on the GRB outflow LF Γ is not negligible. On the other hand, various indirect observational constraints on Γ point to $\Gamma \geq 300$ (e.g. Molinari et al. 2007; and even $\Gamma \geq 600$ for GRB 080916C, Abdo et al. 2009). The derived observational constraints on Γ for bursts of this sample (Section 5.6.1) are consistent with such an inference. In our work, we take $\Gamma = 300$ as a typical value. A higher Γ would only make the above distance constraint even larger. Our knowledge of the local magnetic field strength B is less certain, although the R -dependence of B is weak. Several crude estimates of B based on the synchrotron radiation mechanism for GRB prompt emission suggest $B \sim 10^5$ G at $R \sim 10^{14}$ cm. This typical value has been adopted in our calculations.

The R -constraint we obtained is inconsistent with the photospheric emission model in which the prompt emission arises at the photosphere radius of $10^{11} - 10^{12}$ cm (Rees & Mészáros 2005; Ryde et al. 2006; Thompson et al. 2007). This result alone can not

discriminate between the fireball internal shock model and the magnetic outflow model. By comprehensive modeling the GRB prompt γ -rays and early X-rays, Kumar et al. (2007) concluded a prompt emission site of $R \sim 10^{15} - 10^{16}$ cm, which is supported by their further general modeling of the γ -ray emission properties (Kumar & McMahon 2008). A large R is derived for GRB 080916C through the pair opacity constraint (Abdo et al. 2009; Zhang & Pe’er 2009)² and for GRB 080319B through the synchrotron self-absorption constraint (Racusin et al. 2008) and the SSC scattering optical depth constraint (Kumar & Panaitescu 2008). In summary, a large prompt emission distance from the central engine seems to be supported by three independent approaches, respectively, i.e. in γ /X-rays (e.g., Lazzati & Begelman 2005; Lyutikov 2006; Kumar et al. 2007), in GeV γ -rays (Abdo et al. 2009; Zhang & Pe’er 2009), and in the optical band (this work).

We have also studied a sample of GRBs with prompt optical non-detections. Applying the same technique, we do *not* find any inconsistency between their R constraints and those of the optical detection sample. This result is inherited from the findings by Yost et al. (2007b) that no distinction in distributions of β_1 and $\beta_{opt-\gamma}$ can be drawn between the optically dark GRBs and the GRBs with optical detections. However, this is only because the currently limited instrumental sensitivity prevents a distinction from being drawn. Deeper observations in the future in the optical band would provide further information regarding whether the optical deficit is due to a heavier synchrotron self-absorption in these bursts.

5.7.1 Multi-color information for the low-energy spectrum

If multi-color photometry near the optical band exists for the same time interval during the prompt phase, it would provide the local spectral index near the optical band (provided that the extinction correction is properly made). This would be helpful to identify the spectral case the data satisfy. For example, the spectral indices near optical differ by $\Delta\beta = 5/3$ between the cases III and IV, and by $\Delta\beta = 1/2$ between the cases I and III. Unfortunately, this kind of observational information is unavailable for all the time intervals of the optical detection sample we have considered in Table 1. The hope is that future multi-band prompt

²Although both work obtained large R , the inference of R in Abdo et al. (2009) is based specifically on the internal shock model while Zhang & Pe’er (2009) gave a more model-independent constraint on R .

optical detections may be able to break the spectral case degeneracy and to tighten the R -constraint.

5.7.2 Limitations of the method

Our method is based on the assumption that the optical emission is emitted from the same group of electrons that produce the γ -rays in the same site via the same synchrotron radiation. This *one component* assumption has some supports (see Section 5.3) but certainly is not conclusive.

There are three other scenarios that have been discussed in the literature (mostly motivated by interpreting GRB 080319B). The first one invokes two emission zones for optical and γ -rays. For example, in the internal-shock-model based residual collision scenario proposed by Li & Waxman (2008), the shells with high LF contrast in a GRB outflow collide first and merge at smaller radii, producing the γ /X-rays. Later those merged shells with low LF contrasts would collide mildly at later times and larger radii, giving rise to optical emission. Alternatively, if the outflow is neutron rich, the proton shells tend to collide at smaller radii to power γ /X-rays, while the free neutrons only decay at large radii and the decay products would be collided by later injected faster proton shells and power optical emission at larger radii (Fan et al. 2009). In both scenarios, it is expected that the observed optical pulse peak emission time is delayed by $R_{opt}/2\Gamma^2c$ with respect to the γ -ray pulse peak emission time, which may be in principle tested if the data quality is high. These models however do not naturally predict a smooth extension of γ -ray spectrum to the optical band without distinct spectral features. Although they cannot be ruled out by the data in our sample, they are more complicated than our one-zone model.

Secondly, our analysis is not applicable in the following scenario (Yu et al. 2009): a pair of shocks (reverse shock and forward shock) arise when two shells collide in the internal-shock model; different populations of electrons are accelerated in each of the two shocks and the two populations have different typical electron energies and different shock-generated magnetic strengths. The characteristic synchrotron frequencies are different - the forward shock produces the optical emission, while the reverse shock produces the γ -ray emission. These two emissions are two spectrally independent components but are

temporally correlated because the heating of the two electron populations arises from the same dynamical process. Although this model may interpret the peculiar SED shape of GRB 080319B whose prompt optical flux density exceeds the extrapolation from the γ -ray spectrum by 4 orders of magnitude, it is unclear whether it can work properly for the bursts in our optical detection sample.

Finally, the synchrotron + SSC scenario (Kumar & Panaitescu 2008; Racusin et al. 2008) has been proposed to interpret GRB 080319B. For our sample, there is no need to introduce a second distinct spectral component. We consider only pure synchrotron radiation in deriving constraints on R , although we have given the ν_a estimation for SSC radiation whose value is similar to ν_a for synchrotron. In principle, it is possible that the observed emission from optical to γ -rays is dominated by SSC. If this is the case, our approach of constraining R by calculating ν_a may give results somewhat different from the synchrotron case for the same sample of bursts. We did not carry out the analysis for the SSC case because the detailed shape of the SSC spectra is much more complicated than the synchrotron one. Note that our approach assumes that the optical and the γ -rays are from the same group of electrons due to the same radiation mechanism. In the SSC scenario this approach is applicable only if the SSC component dominates a large spectral band from the γ -ray down to the optical and the synchrotron component has to lie well below the optical band. This is usually not expected in the SSC models (e.g. Piran et al. 2009). In any case, if SSC is involved in interpreting any part of the spectrum in our sample, then our analysis is no longer applicable.

Chapter 6

Late Jet in GRBs

6.1 Introduction: late jet and a multi-component GRB stellar explosion

As was reviewed in Chapter 1, two recently discovered GRB features point to the emergence of a late outflow (jet) after the main γ -ray producing outflow has died. The first is the X-ray flares observed at a few $\times 10^2 - 10^3$ s (as late as $10^4 - 10^5$ s in some cases) after the prompt burst; the second is the shallowly decaying component in the overall X-ray light curve. On the other hand, there is a handful cases for which an associated supernova (SN) was confirmed (also see Chapter 1 for details). This strongly favors that GRBs originate from massive star explosions. If the GRB happens approximately at the same time as the SN explosion, it is a natural outcome that when the late jet comes out of the central engine, it will catch up and run into any explosive remnant on its way. This is the scenario we will investigate in this chapter.

There is another motivation for looking at this scenario. In those cases where we don't see a SN spectroscopically or photometrically in the optical band, we can still hope to explore the existence and properties of the SN accompanying the GRB by looking at the interaction of a late jet with the SN remnant and the emission from it. It is likely that every long-duration GRB has a SN accompanying it but some extrinsic and/or intrinsic bias might have hindered the optical detection of the SN component (Woosley & Bloom 2006).

A late jet provides a chance to test this picture in the cases where the ordinary SN features are not easy to detect.

Given the evidences for the existence of a late jet and the physical association of SN and GRBs, one expects a number of different interactions between the following four components in a GRB event (see Figure 6.1 for an illustration): (i) A highly relativistic ($\Gamma \sim 300 - 1000$) narrow jet along the rotation axis with an opening angle ~ 0.1 radian that produces the main GRB event; (ii) A nearly spherically symmetric SN ejecta moving with speed $\sim 10^4 \text{ km s}^{-1}$; (iii) A cocoon fireball created by the passage of the main GRB jet through the star; (iv) A late relativistic jet responsible for the late X-ray flares after the end of the main GRB. See Woosley & Heger (2006) for a detailed version of the multi-component GRB scenario. Also see Wheeler et al. (2000) for a similar but more detailed model which relates various energetic phenomena such as SN, GRB and magnetar in a single stellar explosion.

We will investigate the interactions of a late jet which might have a similar Lorentz factor (LF) and opening angle to those of the main GRB jet, with the expanding SN ejecta and the cocoon. We assume that the SN ejecta and the main GRB jet are launched from the central source at about the same time ¹. Wheeler et al. (2002) described a similar stellar collapsing scenario where a delayed relativistic jet from the eventually formed black hole catches up and collides with an earlier proto-pulsar toroidal field generated mildly relativistic jet as an origin of the γ -ray burst. Ghisellini et al. (2007) firstly considered the collision between a jetted fireball from an intermittent GRB central engine and a stationary cocoon as an alternative to the standard internal shock scenario, but with higher efficiency. Here we are not attempting to explain how a relativistic jet is formed and a γ -ray burst is produced from the relativistic jet or how an accompanying SN is generated, rather we are trying to constrain the physical properties of the late jet, SN ejecta and the cocoon by calculating the emissions from their interactions, and to verify the general picture of GRB-SN connection.

We will use the following fiducial values for a variety of model parameters. For the

¹The observational constraint is that GRB and SN occur within ~ 1 day (e.g., Woosley & Bloom 2006). SN explosion theories estimate that the SN shock breaks out at a few tens of seconds after the core rebound (e.g., Janka et al. 2007 and references therein); this time scale is small compared to the delay of the late jet ($t_F \geq 10^2 \text{ s}$).

late jet, a total energy $E_j \sim 10^{51}$ erg, opening angle $\theta_j \sim 0.1$ radian, LF $\Gamma_j \sim 100$, a delay respective to the launching of the main GRB jet, cocoon and SN ejecta (in our picture the three are launched at more or less the same time) $t_F \sim 10^2$ s, and a duration $t_{dur} \sim 10^2$ s; for the SN ejecta, we use an isotropic-equivalent mass $M_{SN} \sim 10 M_\odot$ and speed $V_{SN} \sim 10^9$ cm s $^{-1}$; for the cocoon, we use an energy $E_c \sim 10^{51}$ erg, a terminal LF $\Gamma_c \sim 10$ and an opening angle $\theta_c \sim 0.6$ radian. Nevertheless an appropriate range of numerical values is assigned to each parameter in the real calculation (e.g., E_j could be two orders of magnitude larger or smaller than the fiducial one, cocoon speed could be sub-relativistic and t_F could be as large as $10^4 - 10^5$ s).

The late jet will run into the SN ejecta first (at a distance $\sim 10^{11}$ cm; see Figure 6.2a), and then catches up and run into the cocoon – if it successfully crosses the ejecta – at a larger distance ($\sim 10^{12} - 10^{14}$ cm; see Figure 6.2b). We investigate the interactions of the late jet with the SN ejecta in Section 6.2 and with the cocoon in Section 6.3 and calculate their associated emissions. The predicted emissions and their detection prospects are confronted with current observational data in Section 6.4. The summary and implications are given in Section 6.5.

6.2 Late jet - SN ejecta interaction

Since the late jet is highly relativistic and the SN ejecta is sub-relativistic, the late jet will catch up with the SN ejecta in a time roughly equal to the distance of the SN ejecta from the explosion center (where the jet emerged), r_{SN} , divided by light speed c . If the late jet is launched with a delay of t_F , then $r_{SN} \approx V_{SN} t_F \approx 10^{11} V_{SN,9} t_{F,2}$ cm (hereafter we use the convention $X_n = X/10^n$ unless specifically notified). At this time the radial width of the ejecta is about the same size of the initial stellar envelope, $\Delta_{SN} \sim r_* \sim 10^{11}$ cm. The ejecta has hardly moved from the initial position of the progenitor stellar envelope for a jet delay $t_F \sim 100$ s. The particle density in the SN ejecta is $n_{SN} \simeq 10^{24} V_{SN,9}^{-2} t_{F,2}^{-2} M_{SN,1} \Delta_{SN,11}^{-1}$ cm $^{-3}$, where M_{SN} is in units of the solar mass, and it is extremely optically thick. If there is any emission from the interaction between the late jet and the SN ejecta, that emission should be thermal.

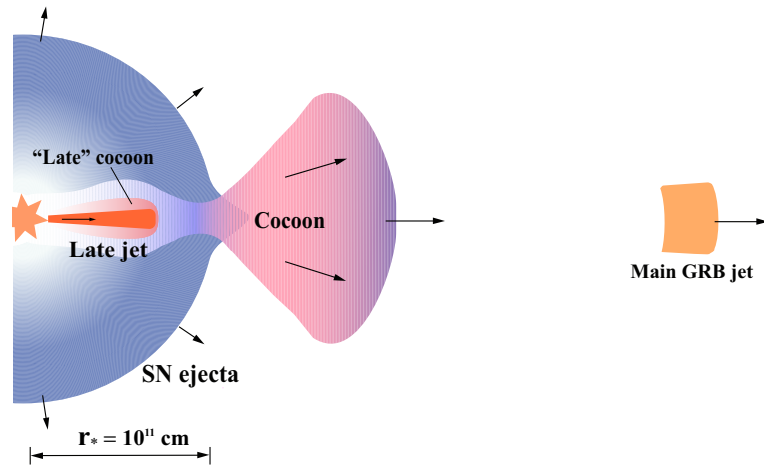


Figure 6.1: Schematic illustration of multiple components in a long GRB and an accompanying supernova (SN). An initial, highly relativistic jet, as shown in the right end of the illustration, is responsible for the prompt GRB. A cocoon, that was inflated by the initial GRB jet as the jet was punching through the envelope of the progenitor star, has broken out of the stellar surface at the same time as the main jet, and has accelerated to mildly relativistic speed. A nearly spherically symmetric sub-relativistic ejecta is responsible for the SN. A late jet responsible for the late X-ray flares in GRBs is launched from the central source and will catch up with the above components. The “late” cocoon is produced when the late jet crosses the SN ejecta. The distances are not to scale.

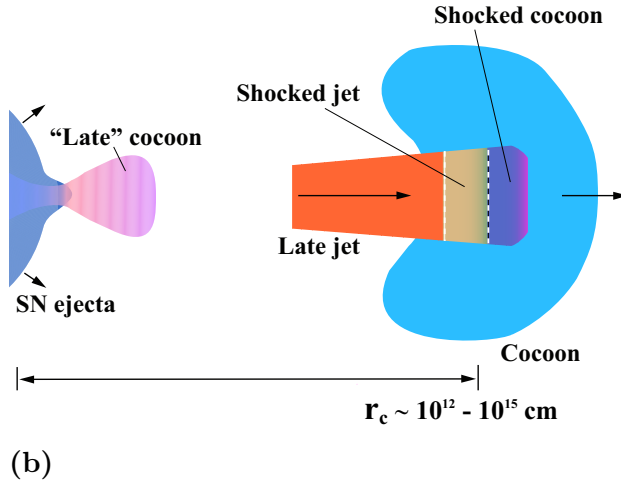
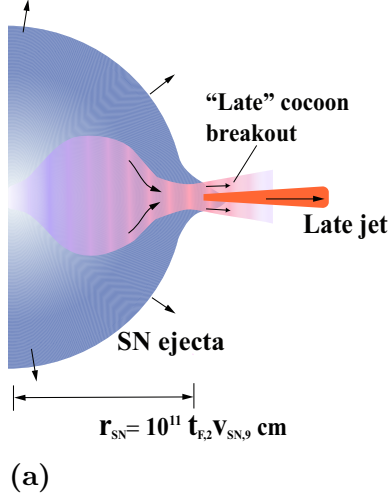


Figure 6.2: **(a)**: Schematic illustration of the late jet - SN ejecta interaction, at a slightly later time than shown in Figure 6.1. The breakout of the “late” cocoon produces a short thermal emission lasting for ~ 10 s. **(b)**: Schematic illustration of the late jet - cocoon interaction, at a somewhat later time than in (a), when the late jet has completely emerged out of the SN ejecta and is colliding with the cocoon created by the main GRB jet as it made its way through the progenitor star. A pair of shocks are going through the cocoon and the late jet, respectively. Note that the “late” cocoon has expanded and cooled down at this time.

6.2.1 The cavity in the SN ejecta

We recall that the main GRB jet has already traversed the star and left a cavity in the polar region before the late jet comes. Since the material enclosing the “wall” of the cavity was heated up by the passage of the main jet, it has tendency to refill the cavity. To find out whether the cavity in the SN ejecta has been filled up before the late-jet encounter, we estimate the time it takes for filling up the cavity.

When inside the star, the cocoon material has a relativistic temperature, i.e., the local sound speed $c_{s,c} = c/\sqrt{3}$. Thus the cocoon material may fill the cavity on a time scale of $r_*\theta_j/c_{s,c} \sim 1$ s, much shorter than the onset of the late jet t_F . However the cocoon will also break out and flow away from the ejecta at that same speed in ~ 10 s, leaving behind a somewhat evacuated polar region. The filling of the polar cavity by the rest of the SN ejecta is uncertain. Assuming a temperature $T \sim 10^8$ K for the SN-shocked ejecta material, it has $c_s \sim 1.2 \times 10^8 T_8^{1/2}$ cm s⁻¹, so the filling time would be $r_*\theta_j/c_s(T) \approx 10^2 r_{*,11} T_8^{-1/2}$ s, comparable to t_F . Considering that the ejecta local temperature possibly decreases from inner parts to outer parts and the transverse size of the cavity gets bigger outward, it is likely that when the late jet hits the ejecta the cavity is partly filled – the inner part is filled but the outer part is not. However, for a very late jet, e.g., $t_F \sim 10^3$ s, the cavity is surely filled before the late jet comes up; and then the question that arises is whether the jet is powerful enough to cross the new refilled cavity. This issue will be discussed elsewhere.

6.2.2 Late jet - SN ejecta crossing

The late jet comoving particle density is $n_j = L_j / (\pi \Gamma_j^2 c^3 r_{SN}^2 \theta_j^2 m_p) = 7 \times 10^{16} L_{j,49} \Gamma_{j,11}^{-2} r_{SN,11}^{-2} \theta_{j,-1}^{-2}$ cm⁻³, where L_j is the late jet luminosity. Because $n_{SN}/n_j \gg 1$, the late jet will be decelerated to a non-relativistic speed after it first hits the ejecta. It will undergo the same process as the GRB main jet did when propagating through the progenitor star. A cocoon forms in the SN ejecta and makes a way for the jet head by pushing the ejecta material sideways. To distinguish it from the cocoon associated with the main GRB jet, let us call this cocoon associated with the late jet as the “late cocoon” (see in Figures 6.1 and 6.2a).

When the jet is moving inside the ejecta, the jet head has been slowed down to be

at a sub-relativistic speed (Ramirez-Ruiz et al. 2002; Matzner 2003):

$$v_h = \left(\frac{L_j}{\pi r_{SN}^2 \theta_j^2 \rho_{SN} c} \right)^{1/2} = 0.8 \times 10^9 L_{j,49}^{1/2} \theta_{j,-1}^{-1} M_{SN,1}^{-1/2} \Delta_{SN,11}^{1/2} \text{ cm s}^{-1}. \quad (6.1)$$

Note that if the SN ejecta width is constant then v_h has no dependence on r_{SN} and therefore on t_F ; but if the SN ejecta is uniformly distributed from the centre to the radius r_{SN} , i.e., $\Delta_{SN} \approx r_{SN}$, then v_h increases with t_F as $\propto t_F^{1/2}$. SN explosion simulations show the latter case, i.e., $\Delta_{SN} \approx r_{SN}$, is the most probable one (e.g., Tanaka et al. 2009).

A constraint on the late jet property can be derived from the requirement that the duration t_{dur} of the jet must be larger than the time that the jet spends to cross the SN ejecta. Thus $t_{dur} > \Delta_{SN}/v_h$ implies $L_{j,49}^{1/2} t_{dur,2} \theta_{j,-1}^{-1} > 1.2 M_{SN,1}^{1/2} \Delta_{SN,11}^{1/2}$.

6.2.3 Thermal emission from the late cocoon break out

The late cocoon – formed by the interaction of late jet with SN ejecta² – will break out of the star immediately following the breakout of head of the late jet (Figure 6.2a). The luminosity of the thermal emission from the late cocoon breakout can be estimated from its temperature and transverse size. Prior to its breakout, the late cocoon has a pressure p_c and its leading head moves with the jet head at the same speed in the radial direction and expands transversely into the SN ejecta with a speed v_\perp . The ram pressure balance at the lateral interface between the late cocoon and the ejecta material gives

$$p_c = \rho_{SN} v_\perp^2, \quad (6.2)$$

where ρ_{SN} is the ejecta mass density.

The late cocoon contains an energy E_c that is approximately equal to the jet luminosity L_j times the shell crossing time Δ_{SN}/v_h , and it is radiation pressure dominated. The volume of the late cocoon just before the breakout is $V_c = \pi \Delta_{SN} r_\perp^2 / 3$, where $r_\perp = \Delta_{SN} v_\perp / v_h$

²The late cocoon should not be confused with the cocoon that was formed and left behind by the main GRB jet. The latter will be discussed in Section 6.3.

is the transverse size. So the pressure is

$$p_c = \frac{E_c}{3V_c} = \frac{L_j v_h}{\pi \Delta_{SN}^2 v_\perp^2}. \quad (6.3)$$

Combining with Eq. (6.2) gives

$$p_c = \left(\frac{L_j \rho_{SN} v_h}{\pi \Delta_{SN}^2} \right)^{1/2}, \quad (6.4)$$

and the thermal temperature is

$$T_{th} = \left(\frac{3p_c}{a} \right)^{1/4} = 1.2 \times 10^8 L_{j,49}^{3/16} \theta_{j,-1}^{-1/8} M_{SN,1}^{1/16} r_{SN,11}^{-1/4} \Delta_{SN,11}^{-5/16} \text{ K}, \quad (6.5)$$

where Eq. (6.1) is used. For a late jet with $t_F \sim 10^2$ s, the typical thermal photon energy should be a few keV. T_{th} becomes smaller for larger t_F ; for instance, when the SN ejecta width Δ_{SN} is $\approx r_{SN}$ and, if $L_j \propto t_F^{-1.5}$ (Lazzati et al. 2008), we have $T_{th} \propto t_F^{-0.8}$.

Let us estimate the luminosity of the thermal emission from the late cocoon breakout. The late cocoon transverse expansion speed is

$$v_\perp = \left(\frac{p_c}{\rho_{SN}} \right)^{1/2} = 0.6 \times 10^9 L_{j,49}^{3/8} \theta_{j,-1}^{-1/4} M_{SN,1}^{-3/8} r_{SN,11}^{1/2} \Delta_{SN,11}^{-1/8} \text{ cm s}^{-1}. \quad (6.6)$$

The cocoon transverse size is $r_\perp = \Delta_{SN} v_\perp / v_h = 0.8 \times 10^{11} L_{j,49}^{-1/8} \theta_{j,-1}^{3/4} M_{SN,1}^{1/8} r_{SN,11}^{1/2} \Delta_{SN,11}^{3/8} \text{ cm}$. Notice that r_\perp is almost $\sim r_{SN}$ for fiducial parameter values.

If we assume the broke-out late cocoon expands isotropically, considering the photon diffusion, Appendix C shows that the thermal emission luminosity is $L_{th} \sim \sqrt{c_s c / \tau_c} E_c / r_{SN}$, where $c_s \approx c / \sqrt{3}$ is the sound speed in the cocoon and is also the speed at which the broke-out late cocoon expands, and τ_c is the late cocoon's initial optical depth. τ_c depends on the mass of the late cocoon, M_c , for which we do not have a firm knowledge; we can only infer M_c must be a small fraction of the SN ejecta mass. Thus, as an order of magnitude estimation we take $M_c \sim 0.1 M_\odot$, which implies $\tau_c \sim 10^{10}$. Plugging the numbers in we find

$$L_{th} = 3.3 \times 10^{45} L_{j,49}^{1/2} \theta_{j,-1} M_{SN,1}^{1/2} M_{c,-1}^{-1/2} r_{\perp,11} \Delta_{SN,11}^{1/2} r_{SN,11}^{-1} \text{ erg s}^{-1}. \quad (6.7)$$

This thermal transient will last for a time comparable to the time it takes for the bulk of the late cocoon to escape the ejecta. After that, the luminosity drops as $\propto t^{-1}$ due to adiabatic cooling (see Appendix C). The late cocoon’s outflow speed is $\sim c_s = c/\sqrt{3}$, so the escape time is $\Delta t_{esc} \approx \Delta_{SN}/c_s = 6 \Delta_{SN,11}$ s.

An even stronger ($L \sim 10^{46}$ erg s $^{-1}$, due to larger L_j) thermal pulse is associated with the cocoon breakout caused by the main GRB jet. This thermal transient is also short (~ 10 s), with spectral peak at X-rays, and it happens during the earliest times of the main “burst” γ -ray emission when the X-Ray Telescope (XRT) is not pointing towards the burst. Moreover, this emission is probably over-shone by the X-ray extension of the prompt emission itself by 1 – 2 orders of magnitude. Therefore, it is difficult to observe. On the other hand, the thermal transient due to the late cocoon breakout that we consider here arises after the prompt emission has died off and at a time when XRT is already pointing towards the burst. Hence, this transient should be easier to detect.

Note that Eq. (6.7) is based on the assumption that the late cocoon has a spherical shape. It is possible that the late cocoon is beamed, at the breakout and during the later expansion, toward the direction of the late jet that produced it. This is because when the jet head moves near the outer surface of the ejecta, it probably accelerates due to the rapid density drop of the stellar materia there; thus the lateral expansion of the cocoon’s leading head immediately following the jet head should be suppressed. Therefore at that time, the overall cocoon might be in an “hourglass” shape, as illustrated in Ramirez-Ruiz et al. (2002) and in our Figure 6.2a, rather than a conic shape. At the breakout, the hot cocoon material escapes and accelerates radially from a “nozzle” which has a transverse size on the same order of the jet’s. Thus, the transverse size of the visible emitting cocoon right at the breakout could be $r_{th,\perp} \sim r_{SN}\theta_j$, while $r_{\perp} \sim \Delta_{SN}v_{\perp}/v_h$ would be the transverse size of cocoon at its *widest* cross section. In this beamed cocoon case, L_{th} would be smaller than the estimation in Eq. (6.7) by a factor of $\sim \theta_j^{-2}$.

6.3 Late jet - cocoon interaction

We now turn to the interaction of the late jet, after it has successfully crossed the SN ejecta, with the cocoon that was formed by the main GRB jet (see Figure 6.2b). The cocoon breaks out from the star at the same time when the main jet breaks out. Then it accelerates to a mildly relativistic speed. The delay of the late jet with respect to the cocoon breakout is t_F and the late jet catches up with the adiabatically cooled cocoon at $r_i \simeq ct_F/(\beta_j - \beta_c)$, where β_j (Γ_j) and β_c (Γ_c) are the speed (LFs) of the late jet and the cocoon, respectively. When the cocoon speed is mildly relativistic, $r_i \approx 6 \times 10^{14} t_{F,2} \Gamma_{c,1}^2$ cm, which is much further than the late jet - SN ejecta interaction site. For a sub-relativistic cocoon, r_i is close to but still outside the jet - SN ejecta interaction region.

6.3.1 Cocoon geometry and dynamics

At the breakout, the cocoon has an energy E_c , and an energy-to-mass ratio η_c . The cocoon opening angle θ_c is determined by its transverse expansion speed $\sim c/\sqrt{3}$, thus $\theta_c \sim 1/\sqrt{3} = 0.6$. During the early stages of expansion, the cocoon's radial width, Δ_c , is approximately the width of the stellar envelope r_* . Later on, due to the radial expansion of a relativistically moving gas, Δ_c asymptotically approaches $r/(2\Gamma_c^2)$ in the lab frame; this happens when $r \geq r_w \approx r_* \eta_c^2$. The cocoon's LF can be described as $\Gamma_c(r) \approx \theta_c r/r_*$ when $r < r_s$, and $\Gamma_c \approx \eta_c$ when $r \geq r_s$, where $r_s = \eta_c r_*/\theta_c$ is the saturation radius (Paczynski 1986; Goodman 1986; Shemi & Piran 1990; Piran, Shemi & Narayan 1993; Mészáros, Laguna & Rees 1993). The evolution of the cocoon's comoving volume, $V'_c(r) = \pi \theta_c^2 r^2 \Delta_c \Gamma_c(r)$, is described by

$$V'_c = \begin{cases} \pi \theta_c^3 r^3, & \text{for } r < r_s \\ \pi \theta_c^2 r^2 \eta_c r_*, & \text{for } r_s < r < r_w \\ \pi \theta_c^2 r^3 / (2\eta_c), & \text{for } r > r_w. \end{cases} \quad (6.8)$$

The pressure evolution of the cocoon follows the adiabatic expansion law: $p_c \propto V_c^{-\gamma}$. Initially the radiation pressure dominates, so $\gamma = 4/3$. When the cocoon's optical depth to Thomson scattering decreases to below unity, the photons decouple from the matter and the radiation pressure drops exponentially; then the gas pressure takes over the dominance of

the pressure with $\gamma = 5/3$. The transition happens at radius $r_t = [\sigma_T E_c / (\eta_c m_p c^2 \pi \theta_c^2)]^{1/2} = 3.5 \times 10^{14} E_{c,51}^{1/2} \eta_{c,1}^{-1/2}$ cm, where σ_T is the Thomson scattering cross section. The initial pressure at the breakout is given by

$$p_{c,0} = \frac{E_c}{3V'_c(r_*)} = 5 \times 10^{17} E_{c,51} r_{*,11}^{-3} \text{ dyn cm}^{-2}. \quad (6.9)$$

The evolution of the cocoon pressure is thus given by

$$\frac{p_c(r)}{p_{c,0}} = \begin{cases} \left(\frac{r_*}{r}\right)^4, & \text{for } r < r_s, \\ \left(\frac{\theta_c}{\eta_c}\right)^{4/3} \left(\frac{r_*}{r}\right)^{8/3}, & \text{for } r_s < r < r_w, \\ (2\eta_c \theta_c)^{4/3} \left(\frac{r_*}{r}\right)^4, & \text{for } r > r_w. \end{cases} \quad (6.10)$$

The comoving density of the cocoon is assumed to be homogeneous; the same is for the late jet. The width of the late jet is determined by its duration and the radial expansion, so $\Delta_j(r) = ct_{dur} + r/(2\Gamma_j^2)$. The jet comoving density is

$$n_j(r) = \frac{E_{j,iso}}{4\pi r^2 m_p c^3 \Gamma_j^2 (t_{dur} + \frac{r}{2\Gamma_j^2 c})}. \quad (6.11)$$

6.3.2 Cavity in the cocoon

There was also initially a cavity in the cocoon left by the passage of the main jet. Here we estimate how quickly the cavity would be filled. The filling up process starts when the main jet dies off. For a typical duration of GRB $t_{grb} \approx 10$ s, the cocoon has moved to a radius $r_c \approx ct_{grb} = 3 \times 10^{11} t_{grb,1}$ cm. Since $r_c < r_s$, the cocoon gas is still relativistic, the sound speed is $c_s \approx c/\sqrt{3}$, and the time required for cavity to close is $\approx r_c \theta_j / c_s = 0.6 t_{grb,1} \theta_{j,-1}$ s which is $\ll t_F$. Thus the cavity is securely filled when the late jet reaches the cocoon.

Now let us consider a possibility that there is a continuous low-level central engine activity (a *low-power* jet) following the end of the main GRB jet and preceding the late jet. This low-power jet and the late jet more or less are the same phenomenon, only with different energy fluxes. The low-power jet might have too small radiation luminosity to have an observational imprint, however it might still be dynamically important for keeping open the polar cavity in the SN ejecta and the cocoon.

To keep the cavity open without significant energy dissipation from the jet and cocoon, the transverse pressure, i.e., the thermal pressure, of the low-power jet should be greater than or equal to the cocoon's pressure at r_c . Though the low-power jet started with a high thermal pressure at a distance $r_0 \sim 10^2$ km from the explosion centre where it was launched, at r_c its thermal pressure has dropped to be much smaller than the cocoon pressure because it has adiabatically expanded by a much larger factor than the cocoon does. Thus, when this low-power jet entered the cavity left by the main GRB jet, it will be squashed rapidly by the gas pressure in the cocoon.

The ram pressure of the low power jet, $p_{j,ram}(r_c) = L_{j,low}/(4\pi r_c^2 c)$ where $L_{j,low}$ is the jet luminosity, can help bore a cavity through the cocoon under suitable conditions. For a long-lasting, continuous jet, the event that takes place after it has been squashed is as follows. If $p_{j,ram}(r_c) > p_c(r_c)$, then the residual, incoming jet will punch a new channel through the cocoon. In doing this, the jet is heated up by the reverse shock, so that the jet which is moving inside the channel could have an enhanced p_j (thermal pressure) that is comparable to p_c , and can keep the channel open. If we assume the low-power jet was launched at the end of the GRB, i.e., $t_{grb} \sim 10$ s, making the equality $p_{j,ram} = p_c(r_c)$ gives $L_{j,low} = 2 \times 10^{48}$ erg s $^{-1}$, with other parameters at fiducial values. The same equality at later times gives the time dependence $L_{j,low}(t) \propto t^{-2}$. So a decaying luminosity profile $L_{j,low}(t) = 2 \times 10^{48} t_1^{-2}$ erg s $^{-1}$ for the low-power jet is required to keep the cavity open, i.e., the minimum required total energy for a low-power jet to keep the cavity open is a few $\times 10^{49}$ erg. Note that at this minimal jet luminosity, the process of keeping the cavity open is *not* smooth and a fraction of jet energy is dissipated and it should have some radiation associated with it.

In conclusion, the polar cavity left by the main GRB jet in the cocoon can fill up quickly – before the late jet reaches the cocoon. The presence of a continuous low-power jet can keep this cavity open, provided that the jet has a minimal total energy of a few $\times 10^{49}$ erg. In the following calculation we consider the case when the cavity is filled up. Clearly if the cavity is empty the late jet cocoon interaction is trivial.

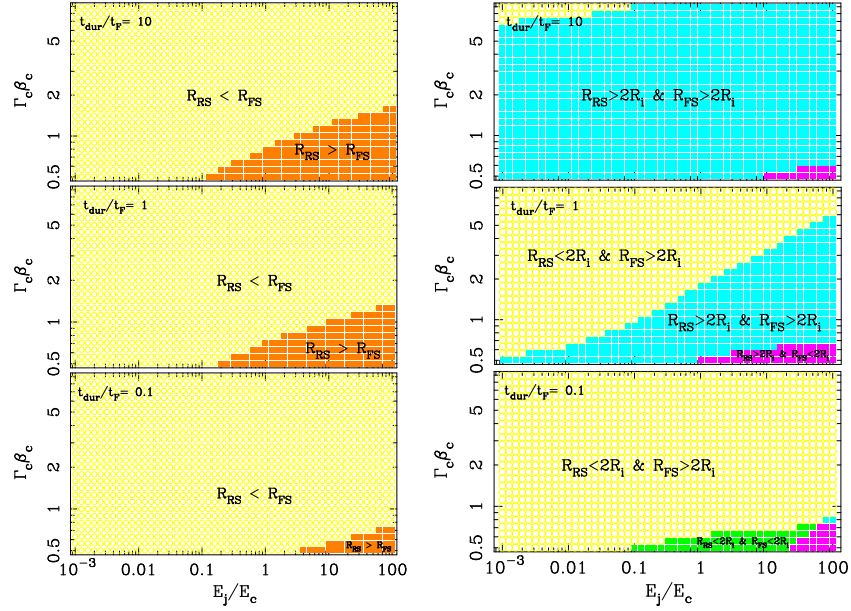


Figure 6.3: *Left* panels: the comparison between the RS crossing radius r_{RS} and the FS crossing radius r_{FS} in the late jet - cocoon interaction for a set of model parameter space. *Right* panels: the comparison of the two crossing radii with $2r_i$, where r_i is the radius at which the late jet catches up with the cocoon and the interaction begins. Γ_c and β_c are the cocoon's LF and dimensionless speed, respectively. E_j and E_c are the kinetic energies of the late jet and the cocoon, respectively. Both crossing radii are numerically calculated from Eq. (6.16). Other parameter values are: $E_c = 10^{50}$ erg, $\theta_j = 0.1$, $\theta_c = 0.6$, $t_F = 300$ s, $\Gamma_j = 100$, $\epsilon_e = 0.1$ and $\epsilon_B = 0.01$. We find the results in this figure do not depend on t_F or Γ_j as long as $t_F \geq 10^2$ s, and $\Gamma_j \gg 1$ (say $\sim 10^2$).

6.3.3 The jet - cocoon interaction phases

The dynamical process of the late jet - cocoon interaction can be decomposed into three phases in the following sequence³: (i) The *Collision Phase* takes place when the jet runs into the cocoon with a forward shock (FS) propagating into the cocoon and a reverse shock (RS) propagating into the jet (see Figure 6.2b). (ii) The *Penetration Phase* begins when either the RS crosses the entire jet or the FS crosses the entire cocoon, whichever comes first. In the first case the shocked fluid (RS-shocked jet and FS-shocked cocoon fluid) will decelerate, after RS crosses the jet, when more and more cocoon material are swept by the FS. In the latter case the shocked fluid will be accelerated, after FS crosses the entire cocoon, by the remaining unshocked jet ejecta, and a new particle population will be accelerated at the RS. (iii) The *Expansion Phase* begins when both the FS and RS have run through their courses, and the entire shocked fluid expands adiabatically.

The collision phase

In this phase, the FS propagates into the cocoon and the RS propagates into the jet. For simplicity we approximate the interaction using a planar geometry. The entire jet / cocoon system can be divided into several zones. Outside the FS (RS) front is the unshocked cocoon (jet), and these are taken to be cold plasma, i.e., $e = n$ and $p = 0$, where e , p and n are the fluid energy density (including the rest mass energy), pressure and particle number density, respectively, all measured in its comoving frame. In between the FS front and the RS front are the shocked cocoon fluid and the shocked jet fluid. These shocked fluids move with the same LF (Γ_s) and have the same thermal pressure; they are separated by a contact discontinuity (CD) plane.

The fluid properties across a shock front are governed by the mass, momentum and energy conservation laws (e.g., Landau & Lifshitz 1959; Blandford & McKee 1976). Across the shock the fluid particle density increases by a factor of $(\hat{\gamma}\bar{\Gamma} + 1)/(\hat{\gamma} - 1)$, and $e = \bar{\Gamma}n$, where $\bar{\Gamma}$ is the shocked fluid LF measured in the unshocked fluid comoving frame; $\hat{\gamma}$ is given by: $p = (\hat{\gamma} - 1)(e - n)$. We use $m_p = c = 1$ to simplify the formulae.

³The three-phase decomposition treatment follows Dermer (2008) who studied the emission due to the external shocks between a GRB jet and a stationary circumburst dense cloud.

At the CD, the pressure in the shocked jet material equals the pressure in the shocked cocoon material, i.e.,

$$\begin{aligned}
& (\hat{\gamma}_{RS} - 1)(\bar{\Gamma}_{sj} - 1) \left(\frac{\hat{\gamma}_{RS}\bar{\Gamma}_{sj} + 1}{\hat{\gamma}_{RS} - 1} \right) n_j \\
& = (\hat{\gamma}_{FS} - 1)(\bar{\Gamma}_{sc} - 1) \left(\frac{\hat{\gamma}_{FS}\bar{\Gamma}_{sc} + 1}{\hat{\gamma}_{FS} - 1} \right) n_c,
\end{aligned} \tag{6.12}$$

where the subscript “RS” refers to the reverse-shocked fluid and “FS” the forward-shocked one, and $\bar{\Gamma}_{sj}$ and $\bar{\Gamma}_{sc}$ are the shocked fluid LFs measured in the unshocked jet and cocoon comoving frames, respectively. $\hat{\gamma}$ lies between 4/3 and 5/3, and can be written in terms of $\bar{\Gamma}$ as $\hat{\gamma} = (4\bar{\Gamma} + 1)/3\bar{\Gamma}$ (Kumar & Granot 2003). Then Eq. (6.12) simplifies to

$$(\bar{\Gamma}_{sj}^2 - 1)n_j = (\bar{\Gamma}_{sc}^2 - 1)n_c. \tag{6.13}$$

Since $\bar{\Gamma}_{sj} = \Gamma_j \Gamma_s (1 - \beta_j \beta_s)$ and $\bar{\Gamma}_{sc} = \Gamma_s \Gamma_c (1 - \beta_s \beta_c)$, we find from the last equation that

$$\Gamma_s = \Gamma_j \frac{\sqrt{a} + \Gamma_c / \Gamma_j}{(a + 1 + 2\sqrt{a}\bar{\Gamma}_{jc})^{1/2}}, \tag{6.14}$$

where $a = n_j/n_c$ is the density ratio, $\bar{\Gamma}_{jc}$ is the unshocked jet LF measured in the unshocked cocoon rest frame. Note that this expression for Γ_s is valid for both sub-relativistic and relativistic shocks, and for $4/3 \leq \hat{\gamma} \leq 5/3$.

The shock (RS or FS) front moves with a LF different from the LF of the shocked fluid. The shock front LF as measured in the unshocked fluid comoving frame – which we denote as $\bar{\Gamma}_{RS,j}$ for the RS and as $\bar{\Gamma}_{FS,c}$ for the FS – is given by the solution to the shock-jump conditions as a function of $\hat{\gamma}$ and $\bar{\Gamma}$ (Eq. 5 of Blandford & McKee 1976). Using the expression of $\hat{\gamma}$ in terms of $\bar{\Gamma}$, we find

$$\bar{\Gamma}_{RS,j} = \frac{4\bar{\Gamma}_{sj}^2 - 1}{\sqrt{8\bar{\Gamma}_{sj}^2 + 1}}, \quad \text{and} \quad \bar{\Gamma}_{FS,c} = \frac{4\bar{\Gamma}_{sc}^2 - 1}{\sqrt{8\bar{\Gamma}_{sc}^2 + 1}}. \tag{6.15}$$

These expressions are valid for both sub-relativistic and relativistic shocks.

The pair of shocks exist until one of the two shocks, either the RS or FS, has traversed through the unshocked fluid. From that time on, the interaction will move to the

next dynamic phase (*Penetration*). To determine which shock (RS or FS) crossing occurs first, we calculate two radii, r_{RS} and r_{FS} , where r_{RS} is the distance of the system when the RS crosses the rear end of the jet, and r_{FS} is when the FS crosses the front end of the cocoon, pretending that the pair of shocks had existed all the way to the larger of the two radii.

At r_{RS} or r_{FS} , the total distance that the shock has traveled through the unshocked fluid is equal to the radial width of the jet or the cocoon at that radius. Thus the two radii can be obtained by solving the equations

$$\Delta_j(r_{RS}) = \int_{r_i}^{r_{RS}} \frac{(\beta_j - \beta_{RS})}{\beta_j} dr \quad \text{and} \quad \Delta_c(r_{FS}) = \int_{r_i}^{r_{FS}} \frac{(\beta_{FS} - \beta_c)}{\beta_c} dr, \quad (6.16)$$

where we have used $dt = dr/\beta_j \simeq dr/\beta_c$.

If $r_{RS} < r_{FS}$, the RS crosses the jet before the FS crosses the cocoon, and vice versa. We calculate r_{RS} and r_{FS} for different parameters. The results are shown in Figure 6.3. We find that $r_{RS} < r_{FS}$, i.e., the RS crossing occurs first, for most of the parameter space of E_j/E_c and $\Gamma_c\beta_c$; $r_{RS} > r_{FS}$ can only happen when the cocoon bulk motion is sub-relativistic ($\Gamma_c\beta_c < 1$) and the energy carried by the late jet is much larger than that of cocoon ($E_j/E_c \gg 1$). We will use this result later (Sub-sections 6.3.4 - 6.3.5) to simplify the calculation of the light curve by assuming that RS crossing always occurs before FS crossing.

The penetration phase

After the RS crosses the jet, the FS continues to pass through the cocoon. We consider the entire shocked fluid, both the old and the newly shocked, moving together with the same LF. In the rest frame of the unshocked cocoon, the LF of the shocked fluid is determined by the equation for the deceleration of a relativistic blast wave in the adiabatic limit as the

blast wave sweeps up the stationary ambient medium:

$$\Gamma'_s(x') = \frac{\Gamma'_{s,\Delta}}{\sqrt{1 + 2\Gamma'^2_{s,\Delta} m_c(x') c^2 / E'_{j,iso}}} \quad (6.17)$$

(Böttcher & Dermer 2000) where the prime sign denotes the unshocked cocoon rest frame, $\Gamma'_{s,\Delta}$ is the shocked fluid LF at the end of the collision phase, $m_c(x')$ is the isotropic equivalent swept-up mass at the distance x' that the blast wave has traveled.

A significant deceleration of FS occurs after a point where $\Gamma'^2_{s,\Delta} m_c(x'_d) c^2 = E'_{j,iso}$. Before this point, the FS is coasting into the unshocked cocoon at roughly the same speed it had prior to the RS crossing. After this point, the FS decelerates as it sweeps more and more cocoon material (similar to the external shock scenario for the GRB afterglows). If the FS crossing is earlier than the RS crossing, the process is similar except that it is the RS that continues to travel through the unshocked jet.

The expansion phase

After the FS eventually crosses the entire cocoon, the shocked fluid expands outward with a LF determined by Eq. (6.17) but with $m(x')$ replaced by the isotropic equivalent total mass of the cocoon. The relativistic electrons cool via radiation and expansion. The radiation from an adiabatically expanding relativistic shell, when it is optically thin to the Thomson scattering, is discussed in Barniol Duran & Kumar (2009). We will address the optical thick case in Section 6.3.5.

6.3.4 The emission from the late jet - cocoon interaction

We calculate the emission from the late jet - cocoon interaction, and estimate the flux densities at the optical and X-ray bands using standard shock synchrotron emission (e.g., Sari et al. 1998), and taking into account the synchrotron self Compton (SSC) radiation. Just behind the shock front, a fraction of the bulk kinetic energy of the fluid upstream, ϵ_e , is transferred to the electrons, and another fraction, ϵ_B , goes to the magnetic field. All the swept-up electrons are shock-heated into a power-law energy distribution with a spectral

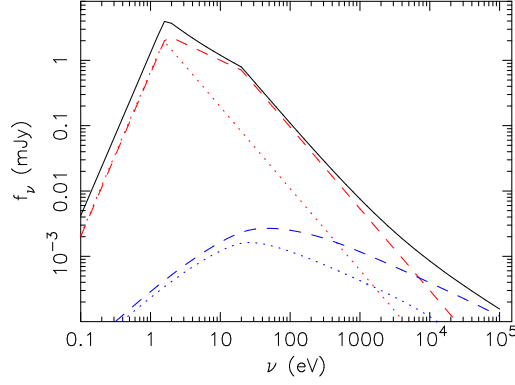


Figure 6.4: The observed spectrum from the late jet - cocoon interaction at the peak of the light curve for $E_j = E_c = 10^{50}$ erg, $\Gamma_c = 3$, $t_{dur}/t_F = 0.3$ and $z = 2$. Other parameter values are same as in Figure 6.3. Various lines represent contributions from different emission regions and spectral components: *red dashed* - RS synchrotron; *red dotted* - RS SSC; *blue dashed* - FS synchrotron; *blue dotted* - FS SSC; *solid* - the sum. For these parameter values, the cocoon is optically thin, and the order of the frequencies is $\nu_c < \nu_{opt} < \nu_a < \nu_i < \nu_X$; ν_{opt} is in the synchrotron-self-absorption optically thick regime, and the spectral peak is around UV band. The SSC emission contribution is important only for γ -ray band and above but is negligible at both optical and X-ray bands.

index p . The minimum LF of shock heated electrons is

$$\gamma_i = \epsilon_e \frac{m_p}{m_e} \left(\frac{p-2}{p-1} \right) (\bar{\Gamma} - 1), \quad (6.18)$$

where $\bar{\Gamma}$ is the shocked fluid LF measured in the unshocked fluid frame. The magnetic field energy density downstream of the shock front is given by

$$U'_B = \frac{B'^2}{8\pi} = 4\bar{\Gamma}(\bar{\Gamma} - 1)\epsilon_B n_0 m_p c^2, \quad (6.19)$$

where B' is the comoving frame field strength and n_0 is the particle number density of the unshocked cocoon or jet. The synchrotron characteristic frequency that corresponds to γ_i is

$$\nu_i = \frac{eB'\gamma_i^2\Gamma_s}{2\pi m_e c(1+z)}, \quad (6.20)$$

where e is the electron charge.

The electron cooling LF, γ_c , is determined by radiative cooling due to synchrotron

and SSC radiations:

$$\gamma_c m_e c^2 = \frac{4}{3} \sigma_T c \gamma_c^2 U'_B (1 + Y) t', \quad (6.21)$$

where σ_T is the electron's Thomson cross section, t' is the elapsing time in the shocked fluid rest frame, and Y is the Compton parameter defined as the ratio of the SSC to synchrotron luminosities; γ_c is obtained by numerically solving Eq. (6.21) (e.g., McMahon, Kumar & Piran 2006). Electrons with $\text{LF} > \gamma_c$ will cool to γ_c in time t' ; the cooling effect is negligible for electrons with $\text{LF} < \gamma_c$. The synchrotron cooling frequency is

$$\nu_c = \frac{\Gamma_s e B' \gamma_c^2}{2\pi m_e c (1 + z)}. \quad (6.22)$$

The self-absorption frequency for the synchrotron electrons, ν'_a , measured in the shocked fluid comoving frame is calculated by (Sari & Piran 1999; Li & Song 2004; McMahon et al. 2006; Shen & Zhang 2009)

$$\max(\gamma_m, \gamma_a) \times 2m_e \nu_a'^2 = F'_{\nu_a'}, \quad (6.23)$$

where $F'_{\nu_a'}$ is the flux density at ν'_a radiated away from the surface of the shocked region.

The emergent synchrotron spectrum of the shock-heated electrons can be approximated as a piece-wise power law function. The peak of the f_ν -spectrum is at $\nu_{max} = \min(\nu_i, \nu_c)$ and the flux density at the peak is

$$f_{\nu, max} = \frac{N_e}{4\pi D^2} \frac{\Gamma_s m_e c^2 \sigma_T B'}{3e(1 + z)}, \quad (6.24)$$

where N_e is the isotropic equivalent total number of shock-heated electrons, D is the luminosity distance. We also calculate the observed flux density due to SSC by (Rybicki & Lightman 1979)

$$f^{ic}(\nu) = \frac{3}{4} \sigma_T \delta s \int \frac{d\nu_s}{\nu_s^2} \nu f^{syn}(\nu_s) \int_{\gamma_i}^{\infty} \frac{d\gamma}{\gamma^2} n_e(\gamma) F\left(\frac{\nu}{4\gamma^2 \nu_s}\right), \quad (6.25)$$

where δs is the line-of-sight width of the emitting source, ν_s and $f^{syn}(\nu_s)$ are the synchrotron frequency and flux density (in the observer frame), respectively, and $n_e(\gamma)$ is the number

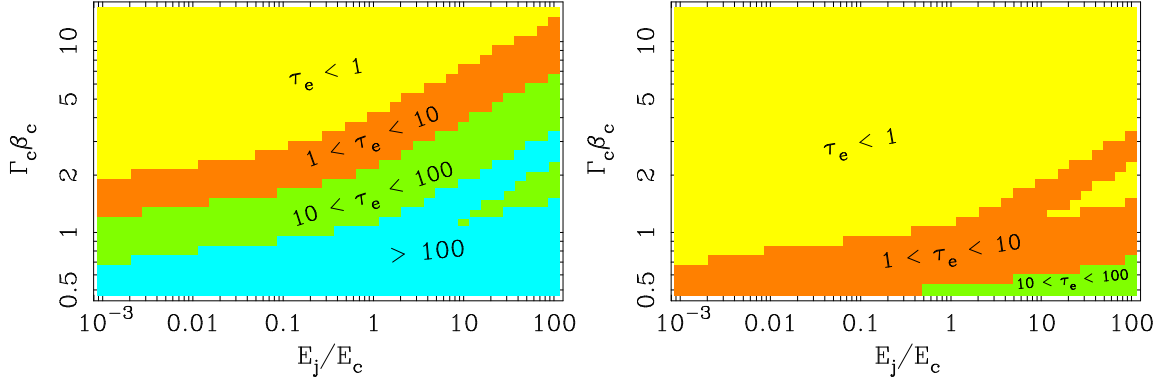


Figure 6.5: Contours of τ_e — the shocked region optical depth to Thomson scattering at the peak of the flux from the late jet - cocoon interaction. *Left*: for $t_F = 10^2$ s; *Right*: for $t_F = 10^3$ s. For even larger t_F (say $\sim 10^4$ s), we find $\tau_e < 1$ for all parameter space. Other parameter values are same as in Figure 6.3 except $t_{dur}/t_F = 0.3$.

of shocked electrons per unit volume per unit interval of γ ; $n_e(\gamma) \propto \gamma^{-p}$ for $\gamma > \gamma_i$ [the modification of $n_e(\gamma)$ due to the radiative cooling is included in our calculations]. The function $F(x) = 2x \ln x + x + 1 - 2x^2$ for $0 < x < 1$ and is 0 otherwise. Using the expression for optical depth τ_e due to Thomson scattering, the SSC flux density can be written as

$$f^{ic}(\nu) = \frac{(3/4)\tau_e}{\int_{\gamma_1}^{\infty} n_e(\gamma) d\gamma} \int \frac{d\nu_s}{\nu_s^2} \nu f^{syn}(\nu_s) \int_{\gamma_1}^{\infty} \frac{d\gamma}{\gamma^2} n_e(\gamma) F\left(\frac{\nu}{4\gamma^2\nu_s}\right). \quad (6.26)$$

Figure 6.4 depicts the spectrum observed at the time when the RS crosses the jet. The order of the characteristic frequencies in this example is $\nu_c < \nu_{opt} < \nu_a < \nu_i < \nu_X$, and ν_a is in the UV band. The SSC contribution is negligible at optical band and it becomes important for photon energy $\geq \sim 1$ keV.

6.3.5 Light curves

The light curve from the late jet - cocoon interaction is mainly determined by the evolution of $f_{\nu, max}$, ν_i , ν_c and ν_a . The optical depth of the shocked fluid region may alter the final light curve shape, which will be addressed later in this sub-section (§6.3.5). We follow the treatment of Yu & Dai (2009) and calculate the light curve. We define T_{exp} as the time when the shocked fluid has traveled a distance of $2r_i$, where r_i is the interaction radius (here and in the following, times denoted with the capitalized letter “T” are the observer’s times

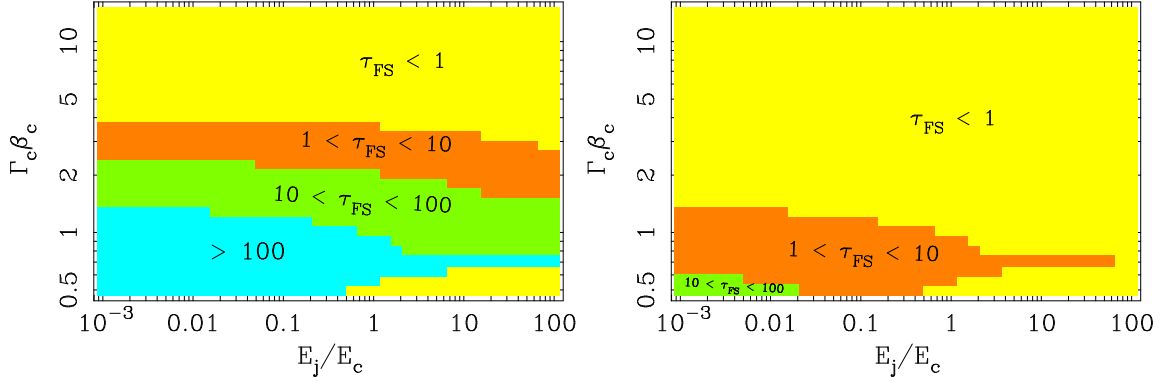


Figure 6.6: Contours of τ_{FS} — the optical depth for the unshocked cocoon that is still in front of the FS at the peak of the flux from the late jet - cocoon interaction. *Left:* for $t_F = 10^2$ s; *Right:* for $t_F = 10^3$ s. For even larger t_F (say $\sim 10^4$ s), we find $\tau_{FS} < 1$ for all parameter space. Other parameter values are same as in Figure 6.3 except $t_{dur}/t_F = 0.3$.

and $T = 0$ is the time when the interaction begins). Thus, $T_{exp} = r_i/(2\Gamma_s^2 c)$; before T_{exp} , the increase of the radius can be neglected and B' and Γ_s are considered to be constant; after T_{exp} , the attenuation of the density and B' due to the radius increase must be taken into account.

We also define the shock-crossing time $T_{cro} = \min(T_{RS}, T_{FS})$, where T_{RS} and T_{FS} , calculated in Eq. (6.16), are the crossing times for the reverse shock and the forward shock, respectively (Figure 6.3 shows $T_{RS} < T_{FS}$ for most of the model parameter space). Before T_{cro} , the radial spreading of the shocked region is suppressed by the existence of two shocks, thus the volume of the shocked region $V' \propto r^2$ and the internal energy density $e' \propto V'^{-1} \propto r^{-2}$; the total number of shock heated particles increases linearly with time. After T_{cro} , the radial expansion has to be considered and the shocked region experiences adiabatic cooling. During this phase, $V' \propto r^s$ (where $s = 2 \sim 3$) and the internal energy density $e' \propto V'^{-4/3} \propto r^{-4s/3}$.

Therefore the evolution of B' and $f_{\nu, max}$ are as follows: (i) For $T_{cro} < T_{exp}$,

$$B' \propto \begin{cases} T^0, & T < T_{exp}; \\ T^{-2s/3}, & T > T_{exp}; \end{cases}, \quad (6.27)$$

$$f_{\nu, \max} \propto \begin{cases} T, & T < T_{\text{cro}}; \\ T^0, & T_{\text{cro}} < T < T_{\text{exp}}; \\ T^{-2s/3}, & T > T_{\text{exp}}; \end{cases} \quad (6.28)$$

(ii) For $T_{\text{cro}} > T_{\text{exp}}$,

$$B' \propto \begin{cases} T^0, & T < T_{\text{exp}}; \\ T^{-1}, & T_{\text{exp}} < T < T_{\text{cro}}; \\ T^{-2s/3}, & T > T_{\text{cro}}; \end{cases} \quad (6.29)$$

$$f_{\nu, \max} \propto \begin{cases} T, & T < T_{\text{exp}}; \\ T^0, & T_{\text{exp}} < T < T_{\text{cro}}; \\ T^{-2s/3}, & T > T_{\text{cro}}. \end{cases} \quad (6.30)$$

And the temporal dependences of the characteristic frequencies are given by

$$\nu_i \propto \begin{cases} T^0, & T < T_{\text{exp}}; \\ T^{-2s/3}, & T > T_{\text{exp}}, \end{cases} \quad (6.31)$$

$$\nu_c \propto \begin{cases} T^{-2}, & T < T_{\text{exp}}; \\ T^{2s-2}, & T > T_{\text{exp}}, \end{cases} \quad (6.32)$$

for $T_{\text{cro}} < T_{\text{exp}}$, and

$$\nu_i \propto \begin{cases} T^0, & T < T_{\text{exp}}; \\ T^{-1}, & T_{\text{exp}} < T < T_{\text{cro}}; \\ T^{-2s/3}, & T > T_{\text{cro}}, \end{cases} \quad (6.33)$$

$$\nu_c \propto \begin{cases} T^{-2}, & T < T_{\text{exp}}; \\ T, & T_{\text{exp}} < T < T_{\text{cro}}; \\ T^{2s-2}, & T > T_{\text{cro}}, \end{cases} \quad (6.34)$$

for $T_{\text{cro}} > T_{\text{exp}}$.

Note that the evolution of ν_c given above ignores SSC cooling. SSC cooling is included in our numerical calculation as described by Eq. (6.26). We find that the resultant

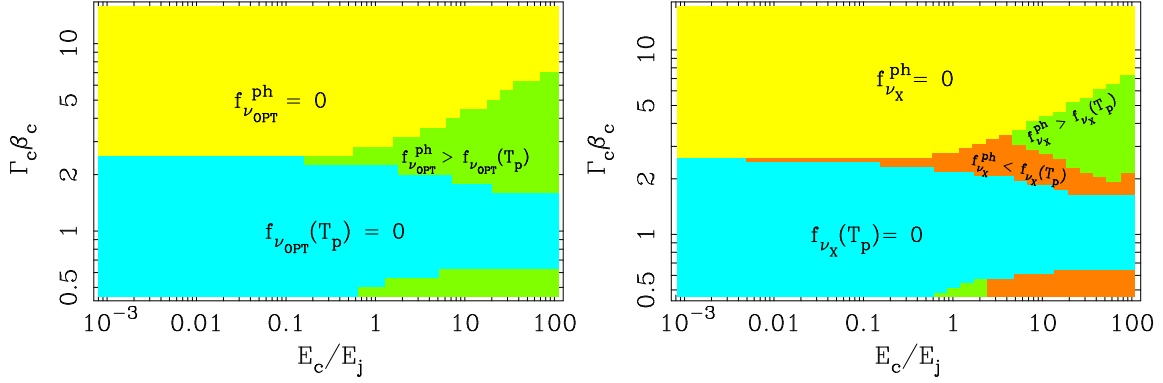


Figure 6.7: The comparison between the observed in situ flux density at T_p and the photospheric flux density, at the optical (*Left*) and X-ray (*Right*) bands, respectively. The photospheric flux is meaningful only in cases of $(\tau_e + \tau_{FS}) > 1$ at T_p ; those cases where $(\tau_e + \tau_{FS}) < 1$ are marked with $f_\nu^{ph} = 0$. In cases of $\tau_{FS} > 1$, the emission produced at T_p is undetectable, and the light curve is dominated by photosphere emission arriving at a later time; these cases are marked with $f_\nu(T_p) = 0$. When $\tau_e > 1$ and $\tau_{FS} < 1$, the light curve is dominated by either the in situ emission produced at T_p and diminished by a factor of τ_e or the photospheric emission, whichever is larger, so is the observed peak flux.

ν_c scalings are not very different from those given above.

To calculate the light curve, we first calculate B' , $f_{\nu,max}$, ν_i , ν_c and ν_a at the expected peak time $T_p = \min(T_{cro}, T_{exp})$, then we use the temporal evolution of B' and $f_{\nu,max}$ to get the observed flux density at other times. The SSC contribution to the flux is included in the light curve calculation. In addition, the optical thickness of the late jet - cocoon system to Thomson scattering could alter the light curve shape because it could delay the escape of the photons from the system; we will consider this next, and then discuss the light curve results.

Optically thick cocoon

When r_i is small – either because of a low LF of the cocoon or a small t_F – the cocoon could be optically thick to Thomson scattering. For instance, the optical depth of the entire cocoon at r_i is estimated to be $\approx 2\sigma_T E_c / [4\pi r_i^2 \Gamma_c m_p c^2 (1 - \cos \theta_c)] \sim 0.1 E_{c,51} \Gamma_{c,1}^{-5} t_{F,2}^{-2}$. Figures 6.5 and 6.6 depict the calculated τ_e and τ_{FS} — the optical depths of the shocked region and the unshocked cocoon, respectively — at the expected light curve peak time T_p .

When $\tau_e \gg 1$, the photons are subject to numerous scattering (diffusion) before

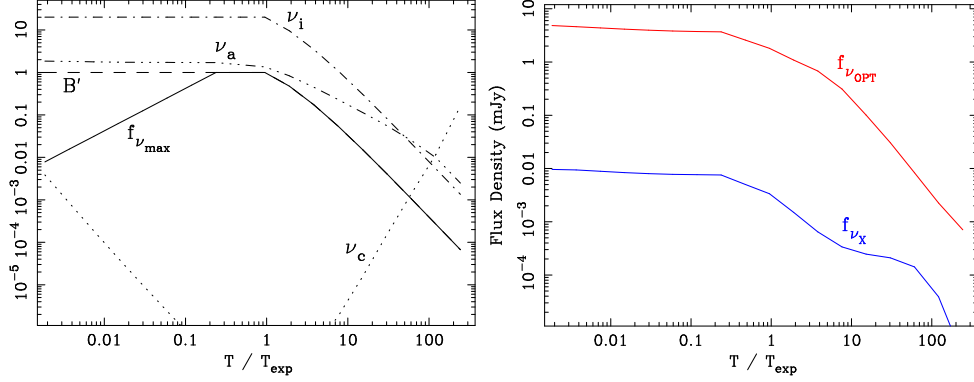


Figure 6.8: *Left*: temporal evolutions of B' , ν_i , ν_c , ν_a and $f_{\nu,max}$ during the late jet - cocoon interaction for same model parameter values as in Figure 6.4. ν_i , ν_c and ν_a are in units of eV, whereas B' and $f_{\nu,max}$ are normalized by their maximum values, respectively. *Right*: observed light curves in optical and X-ray bands. The observer's time T is normalized by the expansion time scale $T_{exp} = r_i/(2\Gamma_s^2 c)$ and $T = 0$ is when the interaction begins.

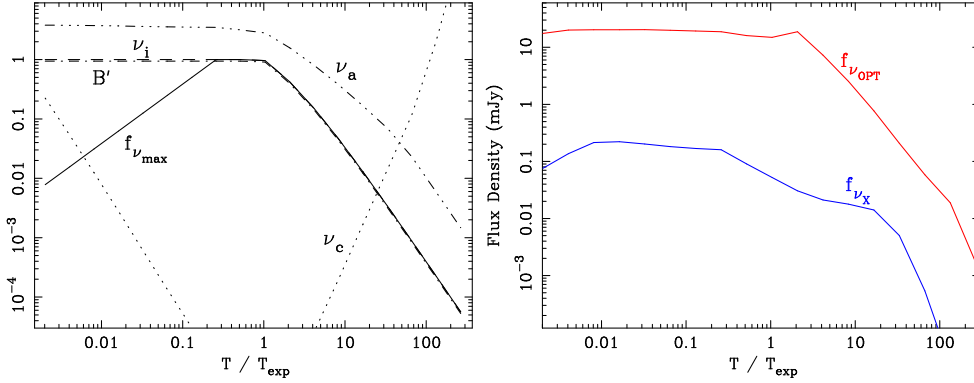


Figure 6.9: *Left*: same as Figure 6.8 but for $E_j = 10 \times E_c = 10^{51}$ erg and $\Gamma_c = 5$. *Right*: observed light curves. Both the optical and X-ray light curves show a flat part at $T < T_{exp}$ because both frequencies are in the fast cooling regime and the decrease of $\nu_c \propto T^{-2}$ just compensates for the increase of $f_{\nu,max} \propto T$. The optical peak at $T > T_{exp}$ is due to the fact that ν_c increases steeply and ν_a drops below ν_{opt} . A rise does not show up in the X-ray light curve at $T > T_{exp}$ because ν_X is always above all of ν_a , ν_i and ν_c .

escaping the plasma. The emergent flux is spread over the diffusion time scale

$$\Delta T_d \approx \frac{r_{ph}}{2\Gamma_s^2 c}, \quad (6.35)$$

which is the delay between the actually observed time of a photon and the time it would have been observed in the absence of scattering, where r_{ph} is the photosphere radius.

When $\tau_e \gg 1$, we consider all the photons emitted during the time up to T_p as a photon gas co-expanding with the baryon gas; the expansion of the system is governed by the radiation pressure rather than the gas pressure, and the scattering between photons and electrons is nearly elastic. This treatment is different from the one adopted by Pe'er, Meszaros & Rees (2006) who consider the case where the gas pressure dominates over the radiation pressure and photons *Compton* scatter off thermal electrons.

The equation of state for the photon gas is $(h\nu)^4 \propto V^{-4/3}$, where $h\nu$ is the characteristic photon energy and $V \propto r^2 \Delta_c$ is the volume of the system (in the photon-baryon gas co-expanding phase, the LF of the system is constant). The width of the system Δ_c is $\propto r$ for the thin shell case and is constant for the thick shell case. Since the system is shock-compressed after the collision, we believe the thin shell case is a more likely possibility to consider than the thick shell case. Thus the temporal evolution of the photon energy is $h\nu \propto T^{-1}$, where T is the observer's time. The shape of the spectrum at the photosphere is unchanged from that at the time T_p .

We first calculate the flux density at T_p neglecting all optical-thick effects. If $\tau_e > 1$ and $\tau_{FS} < 1$, the promptly observed flux in situ at T_p is $1/\tau_e$ of that calculated when τ_e is neglected. Then we also calculate the emergent flux at the photosphere. The real peak flux of the light curve is either the observed flux in situ at T_p or the photospheric flux at later time, whichever is larger, and the light curve would be dominated by that larger component. In case the observed flux in situ at T_p is stronger than the photospheric flux, we calculate elaborately the light curve shape following T_p in the way described in Sec 6.3.5 and numerically estimate its peak time and pulse width. In case the observed light curve is dominated by the flux at the photosphere, its peak time is the photospheric time $T_{ph} \sim r_{ph}/(2\Gamma_s^2 c)$ and the pulse width is also $\approx T_{ph}$. If $\tau_{FS} > 1$, then the unshocked

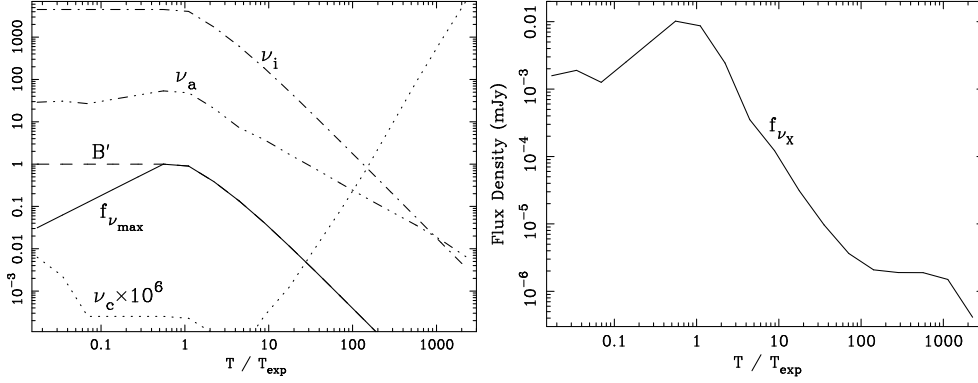


Figure 6.10: *Left*: same as Figure 6.8 but for $E_j = 10^2 \times E_c = 10^{52}$ erg and $\Gamma_c \beta_c = 0.5$. *Right*: observed light curve in X-rays. The optical light curve is not shown, because for this set of parameter values the cocoon is extremely optically thick ($\tau_e \gg 1$ and $\tau_{FS} = 0$; see Figure 6.5 and 6.6), and we find the optical light curve is dominated by the photosphere emission, whose numerical light curve shape has to be calculated differently from that in the optically thin case. However in the X-ray band, the prompt non-thermal flux, after diminished by the optical thick effect, is still brighter than the later photospheric flux. Thus we use the diminished prompt non-thermal flux to represent the observed X-ray light curve.

cocoon blocks the light produced in the shocked region from reaching the observer, thus the emission at the photosphere is what we actually see only and it will completely dominate the light curve. We show in Figure 6.7 a comparison between the observed flux in situ at T_p and the photospheric flux for the considered model parameter space.

6.3.6 Results

Figures 6.8 - 6.10 depict the light curves and the temporal evolutions of emission properties for different values of model parameters. Initially the light curve remains constant up to the shock crossing time or the expansion time, whichever is smaller. This is because $\nu_c < \nu_{opt}$, and therefore the increase of $f_{\nu, max}$ is compensated by the decrease of ν_c . Later, the X-ray flux decays due to the adiabatic expansion, while the optical flux continues to rise as long as $\nu_{opt} < \nu_a$. Therefore generally the optical pulse peaks later and is wider than the X-ray pulse.

The peak flux density distributions are presented in Figure 6.11. For the range of model parameter values, i.e., $E_j/E_c = 10^{-2} - 10^2$, $\Gamma_c \beta_c = 0.5 - 20$, $\epsilon_B = 10^{-2} - 10^{-4}$, $t_F = 10^2 - 10^4$ s and $E_c = 10^{50}$ erg, the optical peak flux density $f_{\nu_{opt}}$ ranges from ~ 0.01

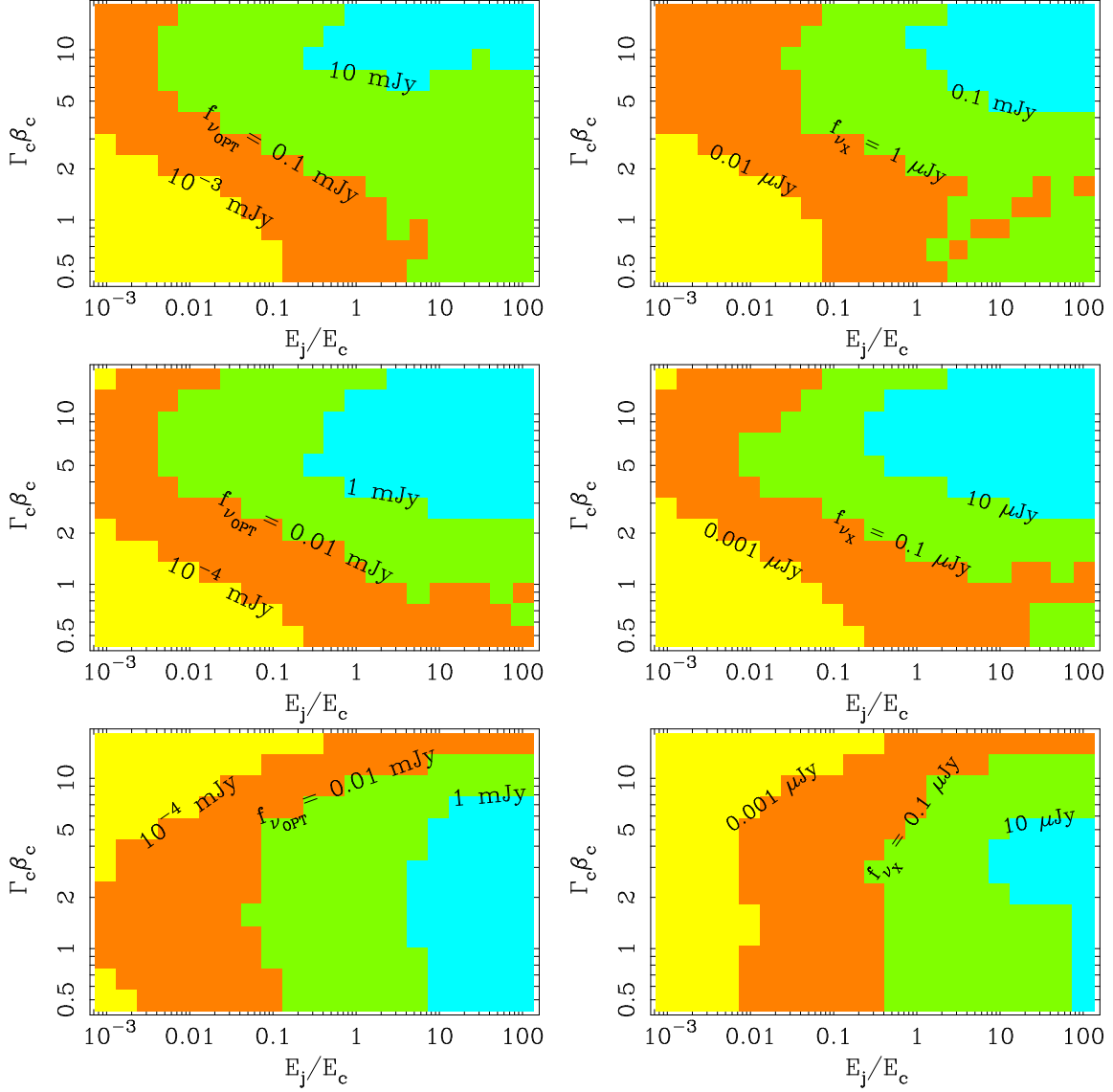


Figure 6.11: The contours of the observed peak flux densities from the late jet - cocoon interaction. *Left panels:* at the optical band ($\nu = 2$ eV). *Right panels:* at the X-ray band ($\nu = 1$ keV). The flux density values labeled on the contours are the demarcation values for two neighbouring contour belts. The ratio of the late jet's duration over its delay t_{dur}/t_F is 0.3 and the redshift is $z = 2$. *Top panels:* for $t_F = 10^2$ s; other parameter values are same as in Figure 6.3. *Middle panels:* same as in top panels except for $\epsilon_B = 10^{-4}$. *Bottom panels:* same as in top panels except for $t_F = 10^4$ s.

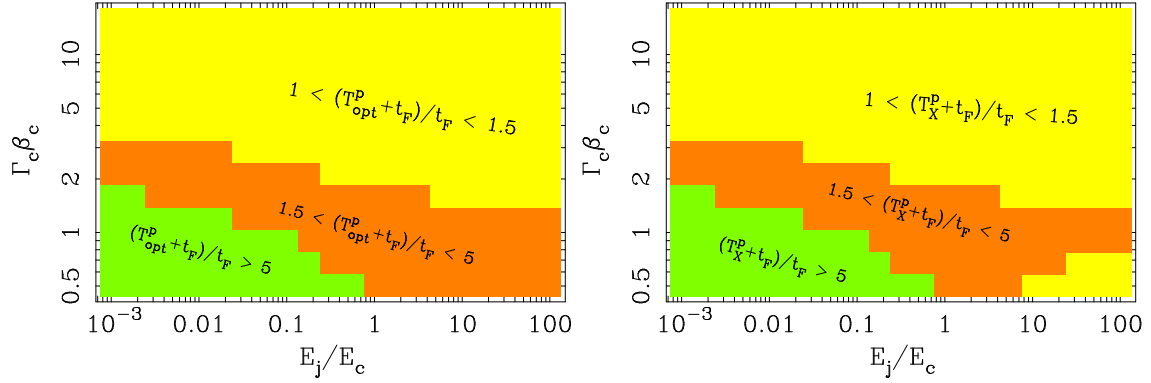


Figure 6.12: Contours of the light curve peak time for the emission from the late jet - cocoon interaction, since the burst trigger and normalized by the delay time of the late jet. *Left:* for the optical light curve; *Right:* for the X-ray light curve. Model parameter values are $t_{dur}/t_F = 0.3$ and $t_F = 100$ s. Other parameter values are same as in Figure 6.3.

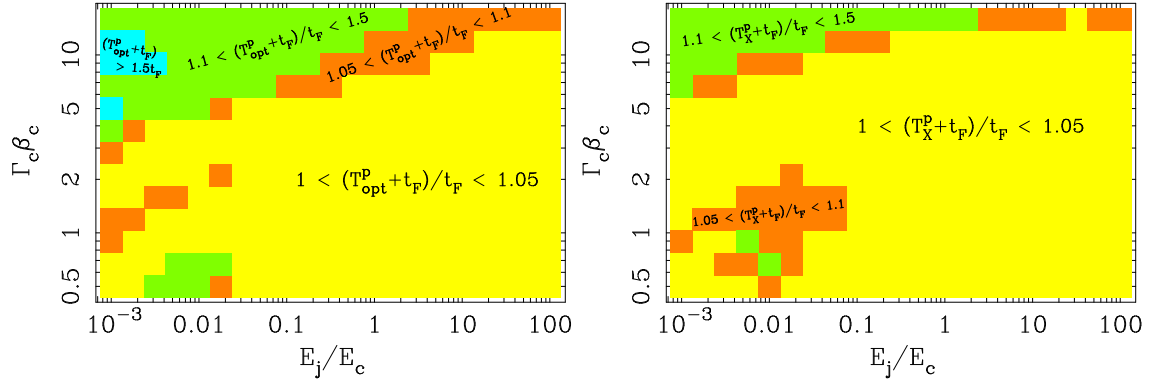


Figure 6.13: Same as Figure 6.12 except for $t_F = 10^4$ s.

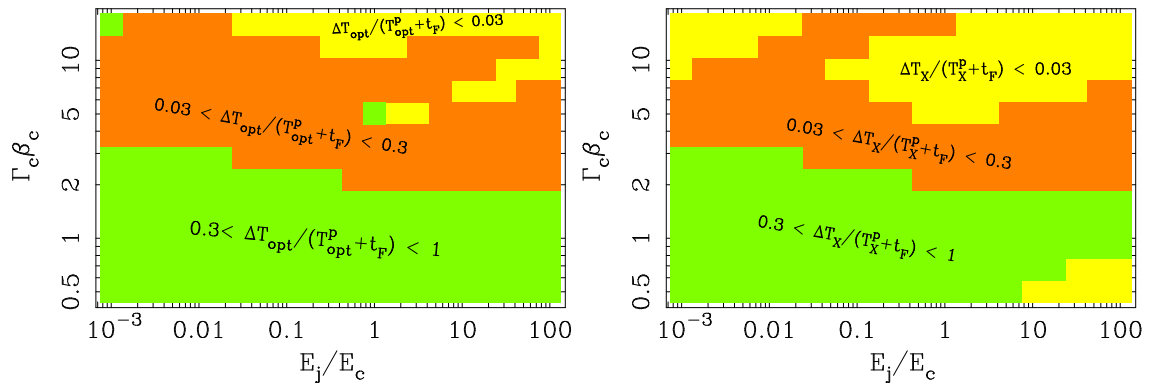


Figure 6.14: Contours of the full width at half maximum (FWHM) of the light curve from the late jet - cocoon interaction, normalized by the peak time of the light curve since the burst trigger. *Left:* for the optical light curve; *Right:* for the X-ray light curve. Model parameter values are $t_{dur}/t_F = 0.3$ and $t_F = 100$ s. Other parameter values are same as in Figure 6.3.

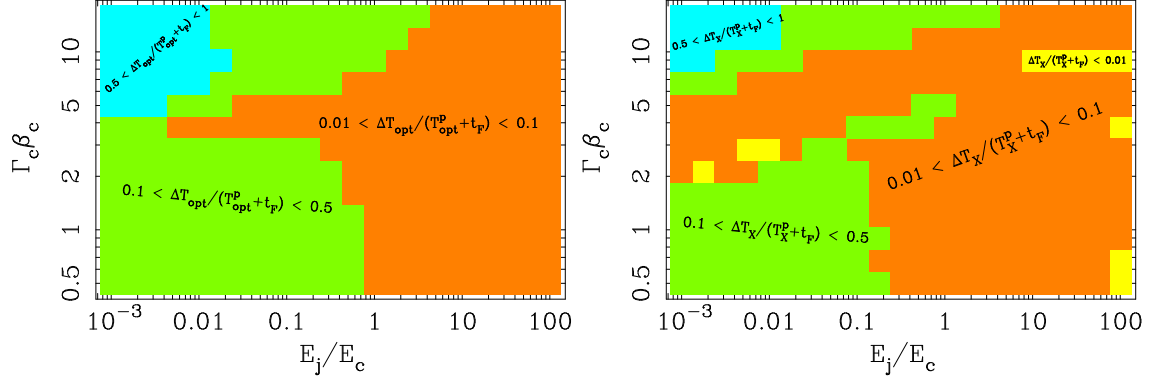


Figure 6.15: Same as Figure 6.14 except for $t_F = 10^4$ s.

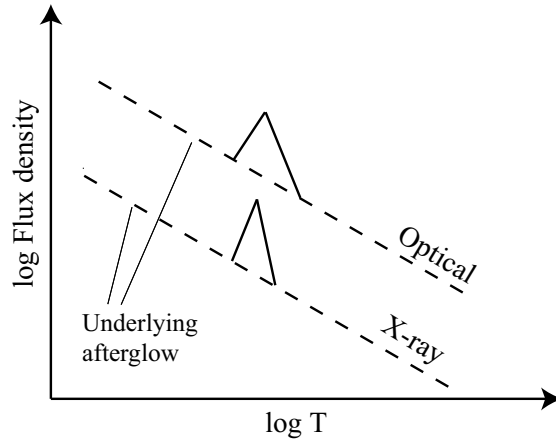


Figure 6.16: The schematic light curve for the emission from the late jet - cocoon interaction superposed on the underlying afterglow light curve. Note the zero time in this figure is the burst trigger time, different from the zero times in Figures 6.8 - 6.10.

μJy to $\sim 0.1 \text{ Jy}$, and the X-ray peak flux density is $f_{\nu_X} \approx 0.001 \mu\text{Jy} - 1 \text{ mJy}$ for $z = 2$. For typical parameter values, i.e., $E_j/E_c = 10^{-1}$, $\Gamma_c\beta_c = 3$, $\epsilon_B = 10^{-2}$ and $t_F = 10^2 \text{ s}$, the fluxes are $f_{\nu_{opt}} \sim 0.1 \text{ mJy}$, $f_{\nu_X} \sim 1 \mu\text{Jy}$. The ratio of the peak flux densities at optical and X-rays is roughly constant: $f_{\nu_{opt}}/f_{\nu_X} \sim 10^2$, since the optical band is much closer to the spectral peak than the X-rays. The peak flux density is highest for $\Gamma_c \approx 5 - 10$, i.e., when the cocoon is mildly relativistic.

The peak flux densities have very broad ranges. The higher ends of the ranges are high compared to the afterglows, but they correspond to some certain extreme model parameter value (i.e., $E_j/E_c \sim 10^2 - 10^3$) and higher values among model parameter ranges (e.g., $\Gamma_c \sim 5 - 10$). The flux values corresponding to typical model parameter values are comparable to those of observed afterglows (see Figures 6.17 - 6.18).

Figure 6.11 also shows the dependence of peak flux densities on ϵ_B and t_F . When ϵ_B varies from 10^{-2} to 10^{-4} , f_ν decreases by a factor of ~ 10 . This reflects the fact that synchrotron electrons' peak specific radiation power and characteristic frequencies are all linearly dependent on B' . When t_F increases from 10^2 s to 10^4 s , f_ν drops by a factor of $\sim 10^2$. This is because the interaction radius $r_i \propto t_F$ and therefore both the cocoon and jet densities are smaller at r_i and so is B' for a larger t_F . However for $\Gamma_c\beta_c < 2$, f_ν increases for a larger t_F ; this is due to the optical thickness when t_F is small (see Section 6.3.5).

Figures 6.12 and 6.13 show the distribution of peak times of the light curves, according to which the peak time can be approximated by t_F , particularly for large values of t_F . We measure the full width at half maximum (FWHM) of the light curves to characterize the pulse width, whose distribution is shown in Figures 6.14 and 6.15. The ratio of the pulse width to the peak time, $\Delta t/t$, has a broad range of 0.01 - 0.5; typically, for lower $\Gamma_c\beta_c$ or E_j/E_c , pulses are wider. The optical pulses are often wider than X-ray pulses, but the difference is not large.

6.4 Observational implication and detection prospects

6.4.1 The Late jet - SN ejecta interaction

We find that late jet - SN ejecta interaction produces a thermal transient due to the breakout of a “late” cocoon produced by the late jet crossing the SN ejecta. It peaks at X-ray band and lasts for ~ 10 s with a bolometric luminosity of $\sim 10^{45}$ erg s $^{-1}$. For a typical GRB red shift of $z = 1 - 2$, this luminosity translates to an observed flux of $\sim 10^{-13} - 10^{-12}$ erg s $^{-1}$ cm $^{-2}$. With a sensitivity of 2×10^{-14} erg s $^{-1}$ cm $^{-2}$ in 10^4 s (Gehrels et al. 2004), Swift / XRT may not be able to detect this thermal transient since the predicted flux is only marginally above the sensitivity whereas the duration of the transient is much shorter than the sensitivity-required integration time.

Moreover, there are three possible effects that could lower the predicted thermal emission flux: (i) The cavity in the polar region of the progenitor star created by the main GRB jet is still open, and in that case the interaction between the late jet and the partially filled cavity is weak resulting in a significantly lower signal than we have estimated in Section 6.2.3. The cavity can be kept open, either because the time was too short for the cavity to fill up, or due to a continuous, low-power jet that precedes the late jet. This low-power jet might also keep the cavity in the cocoon open (see Section 6.3.2). (ii) The “late” cocoon could be beamed toward the direction of the late jet; in that case the visible transverse size of the “late” cocoon is smaller than a spherical “late” cocoon. (iii) The cocoon that is in front of the “late” cocoon and the late jet could be optical thick, e.g., $\tau_c \sim 0.1 E_{c,51} \Gamma_{c,1}^{-5} t_{F,2}^{-2}$ (also see Figures 6.5 - 6.6), and block the thermal transient signal.

It was very rare that a distinctive thermal emission was detected at late times in GRBs. A thermal X-ray emission was once detected from X-Ray Flash (XRF) 060218 (Campana et al. 2006). But its long lasting, slowly variable light curve suggests that it originated in the shock breakout of a quasi-spherical, mildly relativistic ejecta and the late jet scenario does not apply to this event. For the prevailing X-ray flares detected in GRBs, spectral fit shows no compelling evidence for a thermal component (Falcone et al. 2007). The non-detection of a late, short thermal emission component seems to be in line with our prediction.

6.4.2 Late jet - cocoon interaction

A schematic sketch of light curves due to emission from the late jet - cocoon interaction, superposed on the underlying external-shock afterglow component, is illustrated in Figure 6.16. The expected emission from late jet - cocoon interaction has the following features:

(1) *Peak flux density.* The peak flux has a broad distribution (see Figure 6.11). Except for the cases of a very slow cocoon or a very low jet-to-cocoon energy ratio, the emission is fairly bright. For instance, the range of the calculated X-ray peak flux densities corresponds to a flux in the 0.3–10 keV band of $\approx 10^{-14} - 10^{-8} \text{ erg s}^{-1} \text{ cm}^{-2}$ (for a spectral index $\beta_X = -1.1$), mostly above the Swift / XRT sensitivity. Therefore, the X-ray emission from this interaction is detectable by Swift / XRT for most of the parameter space.

(2) *A small $\Delta t/t$ (< 0.5 ; see Figures 6.14 and 6.15).*

(3) *A non-thermal spectrum.* The emission is mostly non-thermal, except when the cocoon speed is sub-relativistic and the delay of the late jet is small (e.g., $t_F \lesssim 10^3 \text{ s}$) thus the thermal photospheric emission might dominate. The X-ray band is in the “fast cooling” spectral regime when the emission is non-thermal, and the optical is near the synchrotron self absorption frequency. The flux density ratio of optical and X-ray is roughly $\sim 10^2$ for $p = 2.5$ (this ratio is larger for larger values of p). This implies that whenever a X-ray pulse is observed, we expect to see an accompanying increase of the optical flux.

Could some of the late X-ray flares in GRBs originated from the late jet - cocoon interaction? We compare the properties of these flares with the prediction of our calculations in the following.

(1) The observed peak count rate in the XRT band (0.3 - 10 keV) for flares is distributed over the range of 0.1 - 100 counts s^{-1} (Chincarini et al. 2007). Using the empirical instrument conversion factor this translates to $f_{\nu_X} \approx 1\mu\text{Jy} - 1\text{mJy}$. This range for the observed X-ray flare flux is roughly what is expected for the late jet - cocoon interaction (cf. Figure 6.11).

(2) The observed value for $\Delta t/t$ lies in the range of 0.02 to 0.6, with a mean value of XRT band (0.3 - 10 keV) 0.1 (Chincarini et al. 2007). This range is consistent with our calculation (see Figures 6.12 and 6.13).

(3) It is rare to find an optical flare accompanying a X-ray flare. This is in part

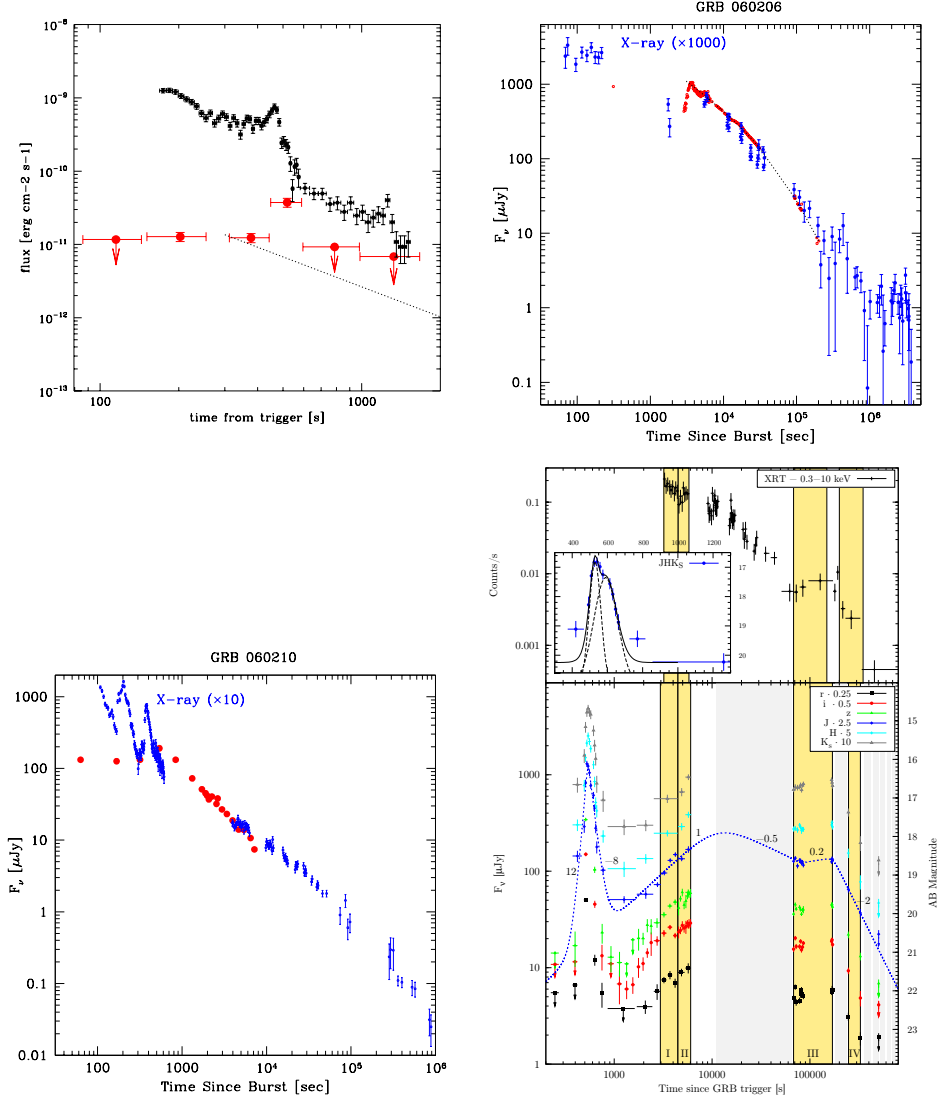


Figure 6.17: Four GRBs that show a late flare or rebrightening in optical afterglow light curve and, in cases where simultaneous X-ray observations are made, a contemporaneous X-ray flare. *Top left:* GRB 050904; filled circles in red are optical data and filled circles in black are X-ray data (from Boër et al. 2006). *Top right:* GRB 060206, and *bottom left:* GRB 060210; the open and filled circles in red color (with unnoticeable errors) are the optical data (from Stanek et al. 2007). *Bottom right:* GRB 080129 (from Greiner et al. 2009).

due to the fact that very few simultaneous optical observations were made in most cases. Nevertheless, we do find four cases where an optical flare or rebrightening is reported and the X-ray data during the time either is missing or does show a flare. These four cases – GRB 050904 (shows an optical flare but its X-ray coverage was too sparse to identify a simultaneous flare; Boër et al. 2006), 060206 (Stanek et al. 2007; Woźniak et al. 2006), 060210 (Stanek et al. 2007; Curran et al. 2007) and 080129 (Greiner et al. 2009) – are shown in Figure 6.17. The last burst shows an early optical flare but without a simultaneous X-ray coverage, and a very late (2×10^5 s since trigger) rebrightening in both optical and X-rays. Among them, the achromatic flarings in GRB 050904, 060210 and 080129 (the very late rebrightening in this burst) are the most likely candidates for a late jet - cocoon interaction event.

On the other hand, there are three cases in which simultaneous optical observations were available but no *optical* flare was detected at the time of very strong X-ray flare (the X-ray flux increased by factors ~ 100 in some of these cases), e.g., GRB 060418, 060607A (Molinari et al. 2007) and 060904B (Rykoff et al. 2009) which are shown in Figure 6.18. This shows that not all X-ray flares are due to the late jet - cocoon interaction. However, neither the late jet nor the cocoon is ruled out in these three X-ray flares. The lack of an optical flare indicates that in these cases it is probable that a low-power, continuous jet with a luminosity of $L_{j,low}(t) = 2 \times 10^{48} t_1^{-2}$ erg s $^{-1}$ (total energy \sim a few $\times 10^{49}$ erg) has kept the cavity open (see Section 6.3.2) and the internal shocks between the more powerful late jet and the preceding, slower, low-power jet gave rise to the X-ray flares.

6.5 Summary

Observations of X-ray flares in many GRB afterglows suggest the existence of a late jet from a long-lived central engine of a GRB at $\sim 10^2$ s but possibly $10^4 - 10^5$ s after the main GRB event. Adopting the collapsing massive star origin for long-duration GRBs, and assuming that the supernova explosion to be at approximately the same time as the GRB, we have investigated the interactions of this late jet with the SN ejecta and, with a cocoon that was left behind when the main GRB jet traversed the progenitor star.

We find that late jet - SN ejecta interaction should produce a thermal transient, lasting about ~ 10 s and with a peak photon energy at a few keV, and if detected, it should appear in the observation around the same time of the flare. However, we find the luminosity of this transient is $\sim 10^{45}$ erg s $^{-1}$, at a typical GRB distance, whose detected flux would be comparable to the Swift / XRT sensitivity. Thus, XRT may not be able to detect this emission. The non-detection of a late, short thermal emission component in GRB observations so far is consistent with the prediction. On the other hand, for the breakout of an extremely luminous late jet (say, $L_j \sim 10^{51}$ erg s $^{-1}$), this thermal emission may be detectable. Future identification of this rare signal can provide another evidence for the massive-star origin of GRBs and new information on the GRB - SN association.

The late jet interaction with the cocoon would cause a flare or rebrightening, superposed on the afterglow light curves, at both the optical and X-ray bands. This flare would have a pulse-width-to-time ratio $\Delta t/t < 1$ (the expected distribution of $\Delta t/t$ is similar to that for X-ray flares). Depending on model parameters, we find for a burst at a redshift $z = 2$ that the peak flux density at optical $f_{\nu_{opt}}$ ranges from 0.01 μ Jy to 0.1 Jy (V-band apparent magnitude 29 to 11.5) and at X-rays f_{ν_X} ranges from 0.001 μ Jy to 1 mJy. For typical parameters $f_{\nu_{opt}} \sim 0.1$ mJy (V-band magnitude ~ 19) and $f_{\nu_X} \sim 1$ μ Jy. Observational identification of this emission would verify the existence of the cocoon produced when the GRB jet traversed the progenitor star, thus it would be another confirmation of the collapsar model for long duration GRBs (e.g., MacFadyen & Woosley 1999; Ramirez-Ruiz et al. 2002; Matzner 2003; Zhang et al. 2004).

The late jet - cocoon interaction might have already been detected in four GRB afterglows in which simultaneous X-ray and optical flares with $\Delta t/t \ll 1$ were observed after the prompt emission has died off (see Figure 6.17). From those candidate events, one can learn about the energetics of late jet and the cocoon by utilizing the emission calculation presented in this work. Let us consider the flare event in GRB 050904 as an example. We find the most probable model parameters – for this burst at $z = 6.3$ and with $t_F = 70$ s – that produce the observed peak $f_{\nu_{opt}}$ and f_{ν_X} (data from Boër et al. 2006; Cusumano et al. 2007; Gou, Fox & Mészáros 2007) to be $E_c \approx 10^{51}$ erg, $\Gamma_c \approx 20 - 50$, $E_j \approx 10^{52}$ erg and $\Gamma_j \approx 500$. Those high energetics seem consistent with the very luminous nature of both the

burst and the flare.

There are three cases in which no optical flare was detected at the time of a strong X-ray flare, even though a number of optical telescopes have been observing these bursts at the time of the X-ray flares (Figure 6.18). This shows that not all X-ray flares are due to the late jet - cocoon interaction. However, neither a late jet nor the cocoon can be ruled out in these cases. It is possible that a low-power jet preceding the late jet with a total energy of at least 10^{49} erg had kept the cavity in the cocoon open, so that the late jet - cocoon interaction was suppressed. If correct this implies a low level continuous emission from the central engine at the level of $\sim 10^{47} (t/10\text{ s})^{-2}$ erg s $^{-1}$ lasting for $\sim 10^2$ s, assuming a radiation efficiency of ~ 0.1 .

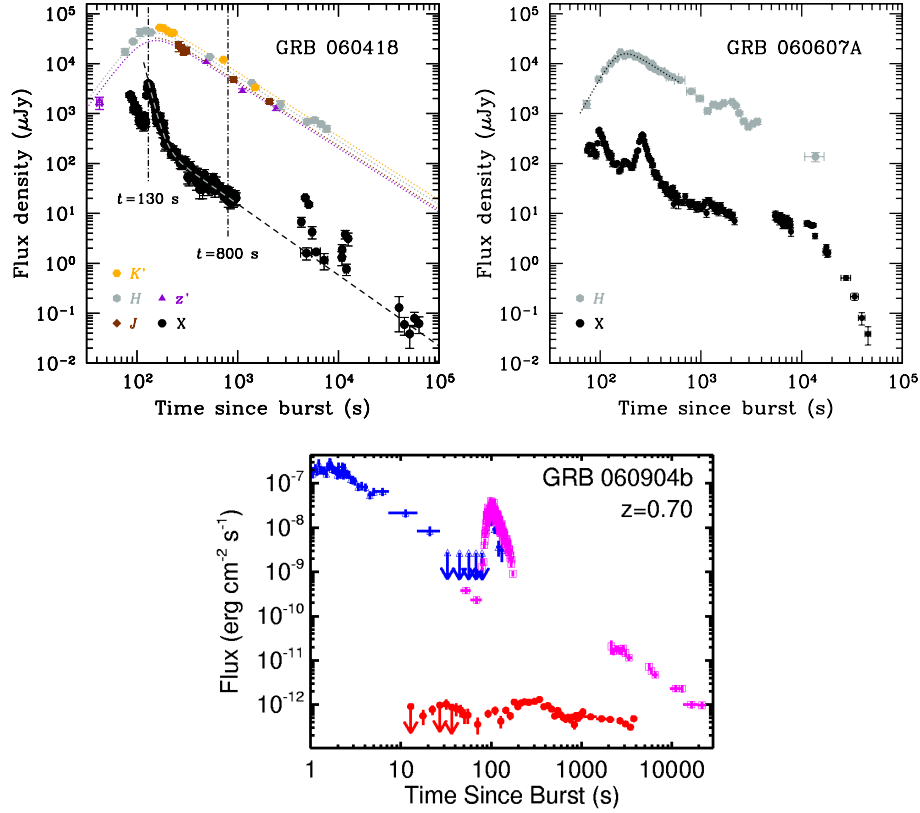


Figure 6.18: The three GRBs that show prominent late X-ray flares but without simultaneous optical flare apparent in the afterglow light curve. *Top left:* GRB 060418; *Top right:* 060607a (both from Molinari et al. 2007). *Bottom:* GRB 060904b; blue triangles are BAT data extrapolated to X-ray band, magenta squares are XRT data and red circles are optical data (from Rykoff et al. 2009).

Chapter 7

Conclusions

Both the theoretical calculations and numerical simulations of the particle acceleration in relativistic shocks show that accelerated electrons' energy spectral index p has a universal value $\approx 2.2 - 2.3$ (e.g., Bednarz & Ostrowski 1998; Lemoine & Pelletier 2003). We showed that the intrinsic parent distribution of p derived in the prompt emission of a sample of ~ 400 GRBs has a Gaussian width of ≥ 0.54 , inconsistent with a δ -function distribution or a universal p (Shen et al. 2006). We find similar results in samples of GRB X-ray afterglows, blazars and pulsar wind nebulae.

A consequence of the ‘internal shock’ model for GRBs is that photons produced in one shell can be scattered by another shell behind it. We find that the scattered flux from a cold slower shell is small and likely to be detected only for those bursts with very weak afterglows (Shen et al. 2008). A hot scattering shell could give rise to a scattered emission as bright as the X-ray plateau component detected in many bursts, provided that the isotropic equivalent total energy carried by the hot electrons is large, $\sim 10^{52} - 10^{56}$ erg. The scattered emission from a faster shell could appear as a late short γ -ray/MeV flash or become part of the prompt emission depending on the delay of the ejection of the shell.

We carefully investigated a dust scattering model that Shao & Dai (2007) proposed to explain the puzzling and prevailing plateau component in GRB X-ray afterglows. We showed that, as one of the model's essential features, the scattered emission undergoes strong spectral softening with time, which clearly contradicts the close-to-zero spectral evolution shown in most of the X-ray afterglow data, thus ruling out this model for explaining the

plateaus in most GRBs (Shen et al. 2009).

We developed a new method to constrain the distance of the GRB prompt emission site from the explosion center, R , by determining the location of the synchrotron self-absorption frequency in the GRB prompt optical-to-X/ γ -ray broadband spectrum. A small sample of four GRBs have simultaneous optical and γ -ray detections in multiple observational time intervals, and also show temporal correlations between the optical and γ -ray LCs. We obtained $R \geq 10^{14}$ cm for this sample (Shen & Zhang 2009). This result rules out the photospheric emission model as the prompt emission mechanism.

We studied a scenario in which a late jet, whose existence is unambiguously indicated by late X-ray flares observed in a majority of GRBs, interacts with various components in a stellar explosion responsible for a GRB (Shen et al. 2010). These components include a SN shell-like ejecta, and a cocoon that was produced when the main jet producing the GRB itself was propagating through the progenitor star. We find that the interaction between the late jet and the SN ejecta probably produces a thermal X-ray transient lasting ~ 10 s and with a luminosity of $\sim 10^{45}$ erg s $^{-1}$. The interaction between the late jet and the cocoon produces synchrotron-self absorbed flares in both optical and X-ray bands, with $\Delta t/t \ll 1$, that are easily detectable with current observing facilities at typical GRB red shifts. Identifying these features in current and future observations would provide valuable information on properties of GRB progenitor stars.

Appendices

Appendix A:

Approximation to the integrand function in calculation of the incident flux on shell 2

Here we show that the integrand function in Eq. (3.6) for the incident flux from shell 1 on point P in shell 2 comoving frame is insensitive to $\sin^2 \alpha''$ so that the integrand can be taken out of the integral as a constant. We will also show that the integrand is of order unity.

Let us call the integrand function $F(\alpha, \theta)$. All equations we have are

$$F(\alpha, \theta) = \frac{(1 + \beta_2 \cos \alpha)^3}{[\beta_1 + \cos(\alpha - \theta)][1 + \beta_1 \cos(\alpha - \theta)]^2} \quad (\text{A-1})$$

$$\tan \alpha'' = \frac{\theta}{\Gamma_2(1 - \frac{\beta_2}{\beta_1} + \frac{\beta_2 \delta t}{R_1})} \quad (\text{A-2})$$

$$\tan \alpha'' = \frac{\sin \alpha}{\Gamma_2(\cos \alpha + \beta_2)}. \quad (\text{A-3})$$

We want to precisely estimate $F(\alpha, \theta)$ and its dependence on $\sin^2 \alpha''$ in the range of α'' from 0 to α''_j , where the subscript “j” always denotes the edge of shell 1. Through equations (A-2) and (A-3), we can express θ in terms of α only:

$$\theta = \frac{\sin \alpha(1 - \frac{\beta_2}{\beta_1} + \frac{\beta_2 \delta t}{R_1})}{\cos \alpha + \beta_2}. \quad (\text{A-4})$$

Then $F(\alpha, \theta)$ becomes $F(\alpha)$. Also, from equation (A-3), express $\sin^2 \alpha''$ in terms of α only:

$$\sin^2 \alpha'' = \frac{\sin^2 \alpha}{\sin^2 \alpha + \Gamma_2^2 (\cos \alpha + \beta_2)}. \quad (\text{A-5})$$

Therefore, we can plot $F(\alpha)$ numerically as a function of $\sin^2 \alpha''$.

The only thing left is to calculate the upper limit of α . Equation (A-2) gives

$$\tan \alpha_j'' = \frac{\theta_j}{\Gamma_2 (1 - \frac{\beta_2}{\beta_1} + \frac{\beta_2 \delta t}{R_1})}. \quad (\text{A-6})$$

Denote $k = \tan \alpha_j''$, and apply it onto equation (A-3) and square both sides of (A-3). Then we get a quadratic equation of $\cos \alpha_j$:

$$(1 + k^2 \Gamma_2^2) \cos^2 \alpha_j + 2\beta_2 k^2 \Gamma_2^2 \cos \alpha_j + k^2 \Gamma_2^2 \beta_2^2 - 1 = 0, \quad (\text{A-7})$$

with roots

$$\cos \alpha_j = \frac{-\beta_2 k^2 \Gamma_2^2 \pm \sqrt{k^2 + 1}}{1 + k^2 \Gamma_2^2}. \quad (\text{A-8})$$

The second root $(-)$ can be ruled out, because when we put it back into equation (A-3), the second root gives $k < 0$, while equation (A-2) requires $k > 0$. Thus

$$\alpha_j = \arccos \left(\frac{-\beta_2 \Gamma_2^2 k^2 + \sqrt{k^2 + 1}}{1 + k^2 \Gamma_2^2} \right) \quad (\text{A-9})$$

is the sole root of the upper limit of α .

We numerically plot $F(\alpha)$ vs. $\sin^2 \alpha''$ for the following model parameter space: Γ_2/Γ_1 ranges from 0.05 to 10, $2\Gamma_1^2 \delta t/R_1$ ranges from 0 to 1000, and $\theta_j = 0.1$. We find, for $\Gamma_2/\Gamma_1 < 1$, $F(\alpha)$ is approximately a linear, monotonically decreasing function of $\sin^2 \alpha''$. Its maximum is 1 and is at $\alpha = 0$, and minimum is always > 0.01 and is at $\alpha = \alpha_j$. A smaller Γ_2/Γ_1 or a larger δt always gives a smaller α_j , thus a minimum of $F(\alpha)$ closer to 1.

This clearly shows that for $\Gamma_2/\Gamma_1 < 1$, $F(\alpha)$ is very weakly dependent on $\sin^2 \alpha''$ thus can be taken out of the integral as a constant ~ 1 .

For $\Gamma_2/\Gamma_1 > 1$, $F(\alpha)$ is not always on order of unity. Since shell 2 is moving toward shell 1, the relativistic beaming effect is important (Panaitescu 2007). When δt is very

small, shell 2 is very close to shell 1, so that α_j'' is larger than $1/\Gamma_{rel}$, where $\Gamma_{rel} \simeq \Gamma_2/(2\Gamma_1)$ is the relative LF between two shells. In this case we find that at an angle $\alpha'' < \alpha_j''$, $F(\alpha)$ starts to drop very sharply from on order of unity to infinitely small, and that dropping-down angle is approximately equal to $1/\Gamma_{rel}$. This means that, in the case of $\Gamma_2/\Gamma_1 > 1$, $\sin^2 \alpha_j''$ in equation (14) should be replaced by a more accurate term $\min(\sin^2 \alpha_j'', 1/\Gamma_{rel}^2)$. However this is only required when δt is small so that $2\Gamma_1^2(T_s - T_p)/R_1 < 100$. Thus the more accurate flux ratio curves for $\Gamma_2/\Gamma_1 > 1$ in our Figure 2 will be slightly flatter in the region of $2\Gamma_1^2(T_s - T_p)/R_1 < 100$ than the ones shown. But our conclusion about a faster shell 2 is *not* affected.

Appendix B:

Derivation of the self-absorption frequency

In this appendix, we provide a rigorous derivation of the blackbody equivalence equation (Eq. 5.3) that we use to calculate the self-absorption frequency. The derivation is carried in the GRB ejecta comoving frame in which the relevant quantities are marked with the prime sign.

The self-absorption frequency ν'_a is defined as $\tau(\nu'_a) = 1$, where $\tau(\nu'_a)$ is the optical depth due to the self-absorption at $\nu' = \nu'_a$. The optical depth $\tau(\nu') = \int \alpha'_{\nu'} ds'$ decreases with the frequency, where $\alpha'_{\nu'}$ is the self-absorption coefficient [$\text{cm}^{-1}\text{Hz}^{-1}$] and the integral is over the line-of-sight width of the emitting source. The integral can be calculated directly only when we have the exact information on the number density of the emitting particles and its distribution over the length, which is not easy. Instead of directly calculating the integral $\int \alpha'_{\nu'} ds'$, we turn to derive the emission coefficient $j'_{\nu'}$ [$\text{erg s}^{-1}\text{cm}^{-3}\text{Hz}^{-1}\text{sr}^{-1}$] and then express the integral of $\alpha'_{\nu'}$ over width into the integral of $j'_{\nu'}$ over width, the latter is just the specific intensity at the source surface which is directly observable.

The synchrotron radiation spectrum, or specific radiation power, of an electron with LF γ gyrating in a magnetic field B with a pitch angle α is

$$P'(\nu', \gamma) = \frac{\sqrt{3}e^3 B \sin \alpha}{m_e c^2} F(\nu'/\nu'_{ch}), \quad (\text{B-1})$$

where e is the electron charge and

$$\nu'_{ch} = \frac{3eB \sin \alpha \gamma^2}{4\pi m_e c} \quad (\text{B-2})$$

is the characteristic photon frequency of the electron. The function

$$F(x) \equiv x \int_x^\infty K_{5/3}(\xi) d\xi \quad (\text{B-3})$$

has the asymptotic form

$$F(x) \sim \begin{cases} \frac{4\pi}{\sqrt{3}\Gamma(1/3)}(x/2)^{1/3} & \sim 2.15x^{1/3}, & \text{if } x \ll 1, \\ (\pi/2)^{1/2}e^{-x}x^{1/2} & \sim 1.25e^{-x}x^{1/2}, & \text{if } x \gg 1, \end{cases} \quad (\text{B-4})$$

where $\Gamma(1/3)$ is the gamma function of argument $1/3$, and it reaches the maximum $F_{max}(x) \simeq 0.92$ at $x \simeq 0.29$. One integral property of the function $F(x)$ is

$$\int_0^\infty x^\mu F(x) dx = \frac{2^{\mu+1}}{\mu+2} \Gamma\left(\frac{\mu}{2} + \frac{7}{3}\right) \Gamma\left(\frac{\mu}{2} + \frac{2}{3}\right), \quad (\text{B-5})$$

where $\Gamma(y)$ is the gamma function of argument y . We will use this property later.

The self-absorption coefficient for any radiation mechanism is given (Rybicki & Lightman 1979) by

$$\alpha'_{\nu'} = -\frac{1}{8\pi m_e \nu'^2} \int d\gamma P'(\nu', \gamma) \gamma^2 \frac{\partial}{\partial \gamma} \left[\frac{N(\gamma)}{\gamma^2} \right], \quad (\text{B-6})$$

where $P'(\nu', \gamma)$ is the single electron's specific radiation power, and $N(\gamma)d\gamma$ is the number density of electrons with energy in the interval from γ to $(\gamma + d\gamma)$. In the case of GRB, $N(\gamma)$ has a two-power-law form and was described in Section 5.2. We rewrite it here as

$$N(\gamma) = \begin{cases} C_\gamma \gamma^{-p_1}, & \text{if } \gamma_m < \gamma < \gamma_p, \\ C_\gamma \gamma_m^{(p_2-p_1)} \gamma^{-p_2}, & \text{if } \gamma > \gamma_p, \end{cases} \quad (\text{B-7})$$

where C_γ is the normalization constant. Note that this distribution set-up is phenomenologically based on the two-power-law shape of the high energy radiation spectrum observed in GRBs; in the context of some specific particle acceleration scenario, e.g., shock acceleration, where two characteristic electron energies, i.e., the injection energy γ_i and the cooling energy γ_c , are involved, there will be $\gamma_m = \min(\gamma_i, \gamma_c)$ and $\gamma_p = \max(\gamma_i, \gamma_p)$. Thus $\partial[N(\gamma)/\gamma^2]/\partial\gamma = (-p-2)N(\gamma)/\gamma^3$, where p could be either p_1 or p_2 depending on the location of γ . For synchrotron radiation the self-absorption coefficient would be

$$\alpha'_{\nu'} = \frac{\sqrt{3}e^3 B \sin \alpha C_\gamma}{8\pi m_e^2 c^2 \nu'^2} \left[(p_1 + 2) \int_{\gamma_m}^{\gamma_p} F(x) \gamma^{-(p_1+1)} d\gamma + (p_2 + 2) \int_{\gamma_p}^\infty F(x) \gamma^{-(p_2+1)} d\gamma \right], \quad (\text{B-8})$$

where $x \equiv x(\gamma) \equiv \nu'/\nu'_{ch}(\gamma) = (4\pi m_e c \nu')/(3eB \sin \alpha \gamma^2)$.

Then we consider two different locations of ν' : $\nu' < \nu'_m$ and $\nu'_m < \nu' < \nu'_p$, respectively. If $\nu' < \nu'_m$, then $F(x)$ falls in the $\propto x^{1/3}$ asymptotic regime. One can transform the integral in Eq. (B-8) for the variable γ into the integral for the variable x . Notice the contribution from the second integral part in Eq. (B-8) is unimportant, as long as $\gamma_m \ll \gamma_p$ and $1/3 < p_1 < p_2$. Thus it gives

$$\alpha'_{\nu'} = \frac{1}{2^{4/3}\Gamma(1/3)} \frac{(p_1 + 2)}{(p_1 + 2/3)} \frac{e^3 B \sin \alpha C_\gamma}{m_e^2 c^2} \left(\frac{4\pi m_e c}{3e B \sin \alpha} \right)^{1/3} \gamma_m^{-(p_1+2/3)} \nu'^{-5/3}. \quad (\text{B-9})$$

If $\nu'_m < \nu' < \nu'_p$, then $x(\gamma_m) \ll 1$ and $x(\gamma_p) \gg 1$. After the transformation of the variable γ into the variable x , the first integral part in Eq. (B-8) is in effect integrating over the x -range from $x(\gamma_m) \sim 0$ to $x(\gamma_p) \sim \infty$, thus we can use Eq. (B-5) to calculate it. For the second integral part of Eq. (B-8), $f(x) \propto x^{1/3}$, but its contribution is unimportant as long as $\gamma_m \ll \gamma_p$ and $1/3 < p_1 < p_2$. Therefore it gives

$$\alpha'_{\nu'} = \frac{\sqrt{3}e^3}{8\pi m_e^2 c^2} \left(\frac{3e}{2\pi m_e c} \right)^{p_1/2} C_\gamma (B \sin \alpha)^{(p_1+2)/2} \Gamma\left(\frac{3p_1+22}{12}\right) \Gamma\left(\frac{3p_1+2}{12}\right) \nu'^{-(p_1+4)/2}. \quad (\text{B-10})$$

To calculate ν'_a from $\tau(\nu'_a) = \int \alpha'_{\nu'_a} ds' = 1$, one has to know the exact information about $N(\gamma_m)$ and its instantaneous distribution over the width of the emitting source along the line of sight, which are always subject to uncertainties. Nevertheless, in their attempts to calculate ν'_a , some authors have calculated $N(\gamma_m)$ by assuming all electrons swept up by the shock are accelerated to relativistic energies either in the blastwave model for GRB afterglows (Granot et al. 1999; Panaitescu & Kumar 2000; Pe'er & Waxman 2004) or in the internal-shock model for prompt emissions (Li & Waxman 2008). We warn that the reality in nature may be that *not all* but only a small fraction of the electrons encountered by the shock can be heated to relativistic energies and radiate, as was suggested by Bykov & Mészáros (1996) and Daigne & Mochkovitch (1998) (also see Kumar & McMahon (2008) for an idea of repeated acceleration of a group of electrons), and this will introduce the biggest uncertainty to $N(\gamma_m)$ hence to this “conventional” approach of calculating ν'_a . In general, this conventional approach over-estimates the number of emitting (and absorbing) electrons and, hence, over-estimates ν_a . In the literature, it is usually suggested that ν_a is slightly below the X-ray band. According to our corrected calculation, ν_a is typically lower

and can extend to close to the optical band in a wide parameter range.

Our new approach here is to express $\int \alpha'_{\nu'} ds'$ in terms of $\int j'_{\nu'} ds'$, both of which contain the term $N(\gamma_m)$ but the latter one is directly observable - it is just the specific intensity at the source surface. Therefore the new approach can avoid the uncertainties associated with partial acceleration and inhomogeneity over the source radial width.

Let us calculate the emission coefficient $j'_{\nu'}$. By definition,

$$4\pi j'_{\nu'} = \int_{\gamma_m}^{\gamma_p} P'(\nu', \gamma) N(\gamma) d\gamma + \int_{\gamma_p}^{\infty} P'(\nu', \gamma) N(\gamma) d\gamma. \quad (\text{B-11})$$

Following the same procedure of calculating $\alpha'_{\nu'}$, the integration gives

$$j'_{\nu'} = \begin{cases} \frac{1}{2^{1/3} \Gamma(1/3)(p_1-1/3)} \frac{e^3 B \sin \alpha C_\gamma}{m_e c^2} \left(\frac{4\pi m_e c}{3eB \sin \alpha} \right)^{1/3} \gamma_m^{(1/3-p_1)} \nu'^{1/3}, & \text{if } \nu' < \nu'_m, \\ \frac{2^{(p_1-1)/2} \sqrt{3}}{4\pi(p_1+1)} \frac{e^3 B \sin \alpha C_\gamma}{m_e c^2} \left(\frac{4\pi m_e c}{3eB \sin \alpha} \right)^{(1-p_1)/2} \Gamma\left(\frac{3p_1+19}{12}\right) \Gamma\left(\frac{3p_1-1}{12}\right) \nu'^{(1-p_1)/2}, & \text{if } \nu'_m < \nu' < \nu'_p. \end{cases} \quad (\text{B-12})$$

The ratio of $j'_{\nu'}$ over $\alpha'_{\nu'}$, also called the source function, is

$$S'_{\nu'} = \frac{j'_{\nu'}}{\alpha'_{\nu'}} = \begin{cases} \frac{2(p_1+2/3)}{(p_1+2)(p_1-1/3)} m_e \gamma_m \nu'^2, & \text{if } \nu' < \nu'_m, \\ \frac{\sqrt{2}}{p_1+1} \left(\frac{4\pi m_e c}{3eB \sin \alpha} \right)^{1/2} \frac{\Gamma\left(\frac{3p_1+19}{12}\right) \Gamma\left(\frac{3p_1-1}{12}\right)}{\Gamma\left(\frac{3p_1+22}{12}\right) \Gamma\left(\frac{3p_1+2}{12}\right)} m_e \nu'^{5/2}, & \text{if } \nu'_m < \nu' < \nu'_p, \end{cases} \quad (\text{B-13})$$

which does not have dependence on $N(\gamma_m)$. It shows that, for synchrotron radiation, the power-law index of the optical thick (to the self absorption) part of the emergent spectrum below ν'_m is 2, while the power-law index of the optical thick spectrum above ν'_m is 5/2.

From the definition of the self-absorption frequency $\int \alpha'_{\nu'_a} ds' = 1$, we have $\int (j'_{\nu'_a} / S'_{\nu'_a}) ds' = 1$. Since $S'_{\nu'_a}$ does not depend on $N(\gamma_m)$ and its distribution over the source width, it can be taken out of the integral. Thus we have $S'_{\nu'_a} = \int j'_{\nu'_a} ds' = F'_{\nu'_a}$, where $F'_{\nu'_a}$ is the specific flux at the source surface in the asymptotic optically thin regime at ν'_a . Rewriting the expression for $S'_{\nu'}$ (Eq. B-13) at $\nu' = \nu'_a$ and using the photon frequency vs. electron energy relation $\nu'_{ch}(\gamma)$ for synchrotron radiation, we get

$$\max(\gamma_m, \gamma_a) \times 2m_e \nu'^2_a = F'_{\nu'_a} C(p_1), \quad (\text{B-14})$$

where γ_a is the energy of the electron whose characteristic photon frequency is ν'_a , and the correction factor

$$C(p_1) = \begin{cases} C_1(p_1) = \frac{(p_1+2)(p_1-1/3)}{p_1+2/3}, & \text{if } \nu'_a < \nu'_m, \\ C_2(p_1) = \sqrt{2}(p_1+1) \frac{\Gamma(\frac{3p_1+22}{12})\Gamma(\frac{3p_1+2}{12})}{\Gamma(\frac{3p_1+19}{12})\Gamma(\frac{3p_1-1}{12})}, & \text{if } \nu'_m < \nu'_a < \nu'_p. \end{cases} \quad (\text{B-15})$$

If we assume a temperature $T' = \max(\gamma_m, \gamma_a)m_e c^2/k$, then Eq. (B-14) becomes

$$2kT' \frac{\nu_a'^2}{c^2} = F'_{\nu'_a} C(\beta_1), \quad (\text{B-16})$$

where for practical uses the correction factor $C(p_1)$ is changed to $C(\beta_1)$ using the relation $\beta_1 = -(p_1 - 1)/2$, and so

$$C(\beta_1) = \begin{cases} C_1(\beta_1) = \frac{(3-2\beta_1)(2/3-2\beta_1)}{5/3-2\beta_1}, & \text{if } \nu'_a < \nu'_m, \\ C_2(\beta_1) = 2\sqrt{2}(1-\beta_1) \frac{\Gamma(\frac{25-6\beta_1}{12})\Gamma(\frac{5-6\beta_1}{12})}{\Gamma(\frac{11-3\beta_1}{6})\Gamma(\frac{1-3\beta_1}{6})}, & \text{if } \nu'_m < \nu'_a < \nu'_p. \end{cases} \quad (\text{B-17})$$

In the samples presented in the main body of the paper, β_1 is among -1.4 to 0, so the ranges for the correction factor are $C_1(\beta_1) = (1.2, 4.5)$ and $C_2(\beta_2) = (1.2, 7.0)$. Therefore Eq. (B-16) shows that, within a factor of a few, at ν'_a the un-absorbed source surface flux density is equal to the flux density of the Rayleigh-Jeans part of the blackbody spectrum with a temperature corresponding to the lowest energy of those electrons that are barely affected by the self absorption. This equation is used to calculate ν'_a in the main body of the paper where the correction factor $C(\beta_1)$ is taken into account.

Appendix C:

Photon diffusive luminosity from a hot, expanding sphere

In this appendix we provide a basis for estimation of the thermal emission from the breakout of the “late” cocoon that was produced in the late jet - SN ejecta interaction studied in Chapter 6. The thermal emission of the broken-out cocoon that was produced by a GRB jet penetrating through the progenitor star was studied by Ramirez-Ruiz et al. (2002) and Matzner (2003). In particular, we consider the photon diffusion in the Thompson-scattering optical thick regime of the cocoon. In general, the problem is to study the thermal emission from a hot gas whose initial state is: isothermal (with $T \sim 10^8\text{K}$), extremely optical thick ($\tau \sim 10^{10}$) and the internal energy is radiation dominated; the gas then freely expands.

Let us consider a sphere of gas and radiation and its expansion. We will consider the expansion sub-relativistic, and homologous inside the gas sphere, meaning $v(r) \propto r$ where r is the radius inside the sphere. The density is always uniform inside the sphere. The internal energy of the sphere is always dominated by the radiation, and it is always isothermal. We assume the accumulated radiative loss up to t is very small compared with, $E_{int}(t)$, the internal energy at t , therefore, the adiabatic law for a photon gas applies, i.e., $E_{int}(t) \propto R(t)^{-1}$. E_0 , R_0 , T_0 and τ_0 are the initial internal energy, radius, temperature and optical depth of the sphere at $t = 0$. The outer boundary of the sphere expands as $R(t) = R_0 + vt = (t_0 + t)v$, where v is the boundary expansion velocity and is a constant, $t_0 = R_0/v$. In the following, we pursue two approaches to derive the surface luminosity from photon diffusion, $L(t)$, as a function of time.

Approach I: energy in the surface layer divided by time t

For a given time t , consider a surface layer of depth s whose photon diffusion time is t , i.e.,

$$\frac{s^2}{\lambda c} = t \quad (\text{C-1})$$

where λ is the photon mean free path. Expressing the temporal dependence in λ and with terms of optical depth, it gives $s = \sqrt{\lambda ct} = (R/R_0)\sqrt{Rct/\tau_0}$. The energy contained in the surface layer is $E_{rad}(t) = 3E_{int}(t)s/R$, where $E_{int}(t) = E_0R_0/R$ is the total internal

energy contained in the sphere under the condition of negligible radiative loss, for which the adiabatic law of radiation strictly applies. This portion of energy will be radiated during time t , so following the spirit of the treatment taken by Nakar & Sari (2010), the diffusive luminosity is

$$\begin{aligned} L(t) &\approx \frac{E_{rad}(t)}{t} \\ &= \frac{3E_0}{t_0} \sqrt{\frac{c/v}{\tau_0}} \left(\frac{t}{t_0}\right)^{-1/2} \left(1 + \frac{t}{t_0}\right)^{-1/2}. \end{aligned} \quad (\text{C-2})$$

The temporal behavior is $L(t) \propto t^{-1/2}$ for $t < t_0$; $L(t) \propto t^{-1}$ for $t > t_0$. Thus, the initial pulse of emission happens in a time scale of t_0 , with an average luminosity $\sim \sqrt{c/(\tau_0 v)} E_0/t_0$, i.e., the energy released in the initial pulse is $\sim \sqrt{c/(\tau_0 v)} E_0$.

Approach II: time derivative of photon number in the surface layer

An alternative approach is to calculate the time derivative of the photon numbers in the surface layer. Since the opacity is dominated by Thompson scattering, the total number of photons, N , is conserved. The average photon energy, $E_{int}(t)/N$, is decreasing with time due to the adiabatic expansion of the sphere, i.e., $E_{int}(t)/N \propto R(t)^{-1}$.

At time t , all photons within the surface layer s can escape. The number of photons that have left or are leaving the sphere up to time t is $N_{esc}(t) = 3Ns/R$. The number rate at which photons diffuse out is

$$\frac{dN_{esc}(t)}{dt} = 3N \frac{d}{dt} \left[\frac{s}{R} \right]. \quad (\text{C-3})$$

The luminosity is simply the photon diffusion number rate multiplied by the average photon energy, i.e.,

$$\begin{aligned} L(t) &= \frac{E_0 R_0}{NR(t)} \frac{dN_{esc}(t)}{dt} \\ &= \frac{3E_0}{2t_0} \sqrt{\frac{c/v}{\tau_0}} \left(1 + 2\frac{t}{t_0}\right) \left(\frac{t}{t_0}\right)^{-1/2} \left(1 + \frac{t}{t_0}\right)^{-3/2}. \end{aligned} \quad (\text{C-4})$$

The peak value and general temporal decaying behavior of $L(t)$ in (C-4) are essentially

identical to the result of approach I (Eq. C-2).

Comparing with a third approach

In the context of a supernova shock breakout, Arnett (1996) constructed an analytical model for the photon diffusion from a gas sphere for which a time-independent gradient profile for the temperature inside the sphere is considered. We summarize here his results about the diffusive luminosity from the sphere: when $t < \sqrt{2t_0t_{0,d}}$, $L(t)$ is more or less constant with an average value $\sim E_0/t_{0,d}$, where $t_{0,d} \approx \tau_0 R_0/c$; when $t > \sqrt{2t_0t_{0,d}}$, $L(t)$ decays with time as in a Gaussian. Thus, the cumulative radiative energy loss within the characteristic time scale of $\sqrt{2t_0t_{0,d}}$ is $E_{rad} \sim E_0 \sqrt{c/(v\tau_0)}$, same as in approaches I and II.

Therefore, between the results of the first two approaches and that of Arnett's approach, the luminosity and the duration of the initial emission pulse are different, but the energy radiated in the pulse is same. The reason for these differences is that Arnett (1996) considers the gradient of temperature inside the sphere, while our approaches use the isothermal assumption.

In the context of a cocoon we discuss in Chapter 6, we think the assumption of an isothermal sphere is appropriate since the cocoon is heated by the moving jet head on its way from the stellar center to close to the surface of the star, as apposed to the situation for a star where heating is done at one point deep inside and at the bottom of the star and hence a temperature gradient is more justifiable.

Bibliography

- [1] Abdo A. A. et al., 2009, *Science*, 323, 1688
- [2] Achterberg, A., Gallant, Y. A., Kirk, J. C., Guthemann, A. W., 2001, *MNRAS*, 328, 393
- [3] Akerlof C. W. et al., 2003, *PASP*, 115, 132
- [4] Alcock C., Hatchett S., 1978, *ApJ*, 222, 456
- [5] Amati A., Frontera, F., Tavani, M., et al., 2002, *A&A*, 390, 81
- [6] Arnett D., 1996, *Supernovae and Nucleosynthesis*, Princeton University Press, Prece-ton, New Jersey. p. 557
- [7] Arons J., 2002, in *ASP Conf. Ser. 271, Neutron Stars in Supernova Remnants*, ed. P. O. Slane & B. M. Gaensler, San Francisco: ASP, p.71 (astro-ph/0201439)
- [8] Band D., Matteson J., Ford L. et al. 1993, *ApJ*, 413, 281
- [9] Baring M. G., Harding A. K. 1997, *ApJ*, 491, 663
- [10] Baring M. G., 2006, *Advances in Space Research*, 38, 1281
- [11] Barniol Duran R., Kumar P., 2009, *MNRAS*, 395, 955
- [12] Barthelmy S. D. et al., 2005, *Nature*, 438, 994
- [13] Beardmore A. P., Page K. L., Gehrels N., Greiner J., Kennea J., Nousek J., Osborne J. P., Tagliaferri G., 2005, *GCN Circ.*, 4043

- [14] Bednarz, J., & Ostrowski, M., 1998, *Phys. Rev. Lett.*, 80, 3911
- [15] Blandford R. D., McKee C. F., 1976, *Physics of Fluids*, 19, 1130
- [16] Blandford R. D. & Znajek R. L., 1977, *MNRAS*, 179, 433
- [17] Blandford, R. D., Ostriker, J. P., 1978, *ApJ*, 221, L29
- [18] Blandford, R. D., Königl, A., 1979, *ApJ*, 232, 34
- [19] Bloom J. S. et al., 1999, *Nature*, 401, 453
- [20] Bloom J. S., Djorgovski S. G., Kulkarni S. R., 2001, *ApJ*, 554, 678
- [21] Bloom J. S. et al., 2002, *ApJ*, 572, L45
- [22] Bloom J. S., Kulkarni S. R., Djorgovski S. G., 2002, *AJ*, 123, 1111
- [23] Bloom J. S., Perley D., Foley R., Prochaska J. X., Chen H. W., Starr D., 2005, *GCN Circ.* 3758
- [24] Boër M., Atteia J. L., Damerdji Y., Gendre B., Klotz A., Stratta G., 2006, *ApJ*, 638, L71
- [25] Böttcher M., Dermer C. D., 2000, *ApJ*, 532, 281
- [26] Bucciantini N. et al., 2006, *MNRAS*, 368, 1717
- [27] Bucciantini N. et al., 2008, *MNRAS*, 383, L25
- [28] Burrows D. N. et al., 2005, *Science*, 309, 1833
- [29] Burrows D. N. et al., 2007, *Phil. Trans. R. Soc. A*, 365, 1213
- [30] Butler N. R., Kocevski D., 2007, *ApJ*, 668, 400
- [31] Bykov A. M., Mészáros P., 1996, *ApJ*, 461, L37
- [32] Campana S. et al., 2006, *Nature*, 442, 1008
- [33] Campana S. et al., 2006b, *A&A*, 454, 113

- [34] Castro Cerón, J. M. et al., 2006, ApJ, 653, L85
- [35] Cenko S. B. et al., 2006, ApJ, 652, 490
- [36] Chevalier R., Li Z.-Y. 2000, ApJ, 536, 195
- [37] Chevalier R. A., 1989, ApJ, 346, 847
- [38] Chen S. L., Li A., Wei D. M., 2006, ApJ, 647, L13
- [39] Chincarini G. et al., 2007, ApJ, 671, 1903
- [40] Christensen L., Hjorth J., Gorosabel J., 2004, A&A, 425, 913
- [41] Cohen E., Piran T., 1999, ApJ, 518, 346
- [42] Costa E., Frontera F., Heise J., Feroci M., et al. 1997, Nature, 387, 783
- [43] Crider, A., Liang, E. P., Preece, R. D., et al., 1999, ApJ, 519, 206
- [44] Curran P. A. et al., 2007, A&A, 467, 1049
- [45] Cusumano G. et al., 2007, A&A, 462, 73
- [46] Cucchiara A., Fox D. B., Berger E., 2006, GCN Circ. 4729
- [47] Cui X.-H, Liang E.-W., Lv H.-J., Zhang B.-B., Xu R.-X., 2010, MNRAS, 401, 1465
- [48] Dai Z. G., Lu T., 1998a, A&A, 333, L87
- [49] Dai Z. G., Lu T., 1998b, Phys. Rev. Lett., 81, 4301
- [50] Dai Z. G., 2004, ApJ, 606, 1000
- [51] Dai Z. G., Wang X. Y., Wu X. F., Zhang B., 2006, Science, 311, 1127
- [52] Daigne F., Mochkovitch R., 1998, MNRAS, 296, 275
- [53] Della Valle M. et al., 2003, A&A, 406, L33
- [54] Dermer C. D., 2008, ApJ, 684, 430

- [55] De Pasquale, M., Piro, L., Gendre, B., et al., 2006, *A&A*, 455, 813
- [56] Di Matteo T. Perna R., Narayan R., 2002, *ApJ*, 579, 706
- [57] Donato, D., Sambruna, R. M., & Gliozzi, M., 2005, *A&A*, 433, 1163
- [58] Duncan R. C. & Thompson C., 1992, *ApJ*, 392, L9
- [59] Doi H., Takami K., Yamazaki R., 2007, *ApJ*, 659, L95
- [60] Draine B. T., 2003, *ApJ*, 598, 1026
- [61] Draine B. T., Bond N. A., 2004, *ApJ*, 617, 987
- [62] Draine B. T., Lee H. M., 1984, *ApJ*, 285, 89
- [63] Eichler D., Livio M., Piran T., Schramm D. N., 1989, *Nature*, 340, 126
- [64] Esin A. A., Blandford R., 2000, *ApJ*, 534, L151
- [65] Evans P. A. et al, 2007, *A&A*, 469, 379
- [66] Falcone A. D. et al, 2007, *ApJ*, 671, 1921
- [67] Fan Y. Z., Wei D. M., 2005, *MNRAS*, 364, L42
- [68] Fan Y.-Z., Zhang B., Wei D.-M. 2009, *Phys. Rev. D*, 79, 021301
- [69] Fan Y., Piran T., 2006, *MNRAS*, 369, 197
- [70] Fenimore, E. E., Conner, J. P., Epstein, R. I., et al. 1988, *ApJ*, 335, L71
- [71] Ford, L. A., Band, D. L., Matteson, J. L., et al., 1995, *ApJ*, 439, 307
- [72] Fruchter A. S. et al, 2006, *Nature*, 441, 463
- [73] Fynbo J. P. U., Hjorth J., Jensen B., Jakobsson P., Moller P., Näränen J., 2005, *GCN Circ.*, 3136
- [74] Fynbo J. P. U. et al., 2005, *GCN Circ.* 3176
- [75] Galama T. J. et al., 1998, *Nature*, 395, 670

- [76] Genet F., Daigne F., Mochkovitch, R., 2007, MNRAS, 381, 732
- [77] Gehrels N., et al., 2004, ApJ, 611, 1005
- [78] Genet F., Daigne F., Mochkovitch, R., 2007, MNRAS, 381, 732
- [79] Ghisellini G., Celotti A., Ghirlanda G., Firmani C., Nava L., 2007, MNRAS, 382, L72
- [80] Giannios D. & Spruit H. C., 2007, A&A, 469, 1
- [81] Gotthelf, E. V., 2003, ApJ, 591, 361
- [82] Goldreich P., Julian W. H., 1969, ApJ, 157, 869
- [83] Godet O. et al., 2006, A&A, 452, 819
- [84] Goodman J. 1986, ApJ, 308, L47
- [85] Gou L.-J., Fox D. B., Mészáros P., 2007, ApJ, 668, 1083
- [86] Granot J., Piran T., Sari R., 1999, ApJ, 527, 236
- [87] Granot J., Kumar P., 2006, MNRAS, 366, L13
- [88] Granot J., Königl A., Piran T., 2006, MNRAS, 370, 1946
- [89] Greiner J. et al., 2009, ApJ, 693, 1912
- [90] Gupta N., Zhang B., 2008, MNRAS, 384, L11
- [91] Hayakawa S., 1970, Prog. Theor. Phys., 43, 1224
- [92] Heng K., Lazzati D., Perna R., 2007, ApJ, 662, 1119
- [93] Hededal, C. B., Haugbølle, T., Frederiksen, J. T., & Nordlund, Å., 2004, ApJ, 617, L107
- [94] Hill G., Prochaska J. X., Fox D., Schaefer B., Reed M., 2005, GCN Circ., 4255
- [95] Hjorth J. et al., 2003, Nature, 423, 847
- [96] Jakobsson P. et al., 2006, A&A, 447, 897

- [97] Jakobsson P. et al., 2006, A&A, 460, L13
- [98] Janka H.-Th., Langanke K., Marek A., Martínez-Pinedo G., Müller B., 2007, Physics Reports, 442, 38
- [99] Katz J. I., Piran T., 1998, ApJ, 501, 425
- [100] Katz J. I., Piran T., Sari R., 1998, Phy. Rev. Let., 80, 1580
- [101] Kaneko Y. et al., 2008, ApJ, 677, 1168
- [102] Kelson D., Berger E., 2005, GCN Circ., 3101
- [103] King A. et al., 2005, ApJ, 630, L113
- [104] Kirk, J. G., Guthmann, A. W., Gallant, Y. A., Achterberg, A., 2000, ApJ, 542, 235
- [105] Klebesadel R. W., Strong I. B., Olson R. A., 1973, ApJ, 182, L85
- [106] Kobayashi S., Zhang B., 2007, ApJ, 655, 391
- [107] Komissarov S. S., Vlahakis N., Königl, A., Barkov M. V., 2009, MNRAS, 394, 1182
- [108] Kouveliotou C, Meegan C A, Fishman G J, et al., 1993, ApJ, 413, L101
- [109] Kulkarni S. R. et al., 1999, Nature, 398, 389
- [110] Kulkarni S. R. et al., in *Gamma-Ray Bursts*, 5th Huntsville Symposium, AIP Conf. Seri. 526, eds.: Kippen M. et al., AIP, New York, 2000, p.277
- [111] Kumar P. et al., 2007, MNRAS, 376, L57
- [112] Kumar P., McMahon E., 2008, MNRAS, 384, 33
- [113] Kumar P., Granot J., 2003, ApJ, 591, 1075
- [114] Kumar P., Narayan R., Johnson J. L., 2008a, Science, 321, 376
- [115] Kumar P., Narayan R., Johnson J. L., 2008b, MNRAS, 388, 1729
- [116] Kumar P. & Narayan R., 2009, MNRAS, 395, 472

- [117] Kumar P. & Panaitescu A., 2000, *ApJ*, 541, L51
- [118] Kumar P. & Panaitescu A., 2000, *ApJ*, 541, L9
- [119] Kumar P. & Panaitescu A., 2008, *MNRAS*, 391, L19
- [120] Landau L. D., Lifshitz E. M., 1959, *Fluid Mechanics*. Pergamon Press, Addison-Wesley Pub. Co., London, p. 501
- [121] La Parola V. et al., 2006, *A&A*, 454, 753
- [122] Lazar A., Nakar E., Piran T, 2009, *ApJ*, 695, L10
- [123] Lazzati D., Begelman M. C., 2005, *ApJ*, 641, 972
- [124] Lazzati D., Perna R., 2007, *MNRAS*, 375, L46
- [125] Lazzati D., Perna R., Begelman M. C., 2008, *MNRAS*, 388, L15
- [126] Lee W. H. & Ramirez-Ruiz E., 2002, *ApJ*, 577, 893
- [127] Lee W. H. & Ramirez-Ruiz E., 2007, *New Journal of Physics*, 9, 17
- [128] Lemoine, M., & Pelletier, G., 2003, *ApJ*, 589, L73
- [129] Li Y., Li A., Wei, D. M., 2008, *ApJ*, 678, 1136
- [130] Li Z., Song L. M., 2004, *ApJ*, 608, L17
- [131] Li Z., Waxman E., 2008, *ApJ*, 674, L65
- [132] Liang E.-W. et al, 2006, *ApJ*, 646, 351
- [133] Liang E.-W., Zhang B.-B., Zhang, B., 2007, *ApJ*, 670, 565
- [134] Lindner C. C., Milosavljević M., Couch S. M., Kumar P., 2010, *ApJ*, 713, 800
- [135] Lithwick Y., Sari R., 2001, *ApJ*, 555, 540
- [136] Lovelace R. V. et al., 2002, *ApJ*, 572, 445
- [137] Lu R.-J., Hou S.-J., Liang E.-W., 2010, Preprint (arXiv:1005.4242)

- [138] Lyden-Bell D., 1996, MNRAS, 279, 389
- [139] Lyutikov M., Blandford R., 2003, Preprint (astro-ph/0312347)
- [140] Lyutikov M., 2006, MNRAS, 369, L5
- [141] MacFadyen A. I., Woosley S. E., 1999, ApJ, 524, 262
- [142] MacFadyen A. I., Woosley S. E., Heger A., 2001, ApJ, 550, 410
- [143] Madau P., Blandford R. D., Rees M. J., 2000, ApJ, 541, 712
- [144] Malesani D. et al., 2004, ApJ, 609, L5
- [145] Mathis J. S., Rumpl W., Nordsieck K. H., 1977, ApJ, 217, 425
- [146] Margutti R., Bernardini G., Barniol Duran R., Guidorzi R., Shen R.-F., Chincarini G., 2010, in preparation
- [147] Mauche C. W., Gorenstein P., 1986, ApJ, 302, 371
- [148] Matzner C., 2003, MNRAS, 345, 575
- [149] McMahon E., Kumar P., Piran T., 2006, MNRAS, 366, 575
- [150] Medvedev M. V., 2000, ApJ, 540, 704
- [151] Meegan C. A., Fishman G. J., Wilson R. B., et al., 1992, Nature, 355, 143
- [152] Mészáros P., Laguna P., Rees M. J., 1993, ApJ, 415, 181
- [153] Mészáros P., 2002, ARA&A, 40, 137
- [154] Mészáros P., 2006, Rep. Prog. Phys. 69, 2259
- [155] Mészáros P., Gruzinov A., 2000, ApJ, 543, L35
- [156] Mészáros P. & Rees M. J., 1993, 1993ApJ...405..278
- [157] Mészáros P. & Rees M. J., 1997, ApJ, 476, 232
- [158] Mészáros P. & Rees M. J., 1999, MNRAS, 306, L39

- [159] Mészáros P. & Rees M. J., 2000, *ApJ*, 530, 292
- [160] Medvedev M. V., Loeb A., 1999, *ApJ*, 526, 697
- [161] Metzger B. D., Thompson T. A., Quataert E., 2007, *ApJ*, 659, 561
- [162] Miralda-Escudé J., 1999, *ApJ*, 512, 21
- [163] Molinari E. et al., 2007, *A&A*, 469, L13
- [164] Morsony B. J., Workman J. C., Lazzati D., Medvedev M. V., 2009, *MNRAS*, 392, 1397
- [165] Murase K., Ioka K., 2008, *ApJ*, 676, 1123
- [166] Murakami, T., Fujii, M., Hayashida, K., et al., 1988, *Nature*, 335, 234
- [167] Nakar E., 2007, *Phys. Rep.*, 442, 166
- [168] Nakar E., Piran T., Granot J., 2003, *New Astronomy*, 8, 495
- [169] Nakar E., Granot J., 2007, *MNRAS*, 380, 1744
- [170] Nakar E. & Sari R., 2010, Preprint (arXiv:1004.2496)
- [171] Narayan R., Paczynski B., Piran T., 1992, *ApJ*, 395, L83
- [172] Narayan R., Piran T., Kumar P., 2001, *ApJ*, 557, 949
- [173] Niemiec, J., & Ostrowski, M., 2004, *ApJ*, 610, 851
- [174] Nousek J. A. et al., 2006, *ApJ*, 642, 389
- [175] O’Brien P. et al., 2006, *ApJ*, 647, 1213
- [176] Ostrowski, M., & Bednarz, J., 2002, *A&A*, 394, 1141
- [177] Overbeck J. W., 1965, *ApJ*, 141, 864
- [178] Paczyński B., 1986, *ApJ*, 308, L43
- [179] Paczyński B., 1998, *ApJ*, 494, L45

- [180] Paczyński B. & Xu G., 1994, *ApJ*, 427, 708
- [181] Pagani C., La Parola V., Burrows D. N., 2005, *GCN Circ.*, 3934
- [182] Page K. L. et al., 2007, *ApJ*, 663, 1125
- [183] Panaitescu A., Kumar, P., 2000, *ApJ*, 543, 66
- [184] Panaitescu A., & Mészáros P., 2000, *ApJ*, 544, L17
- [185] Panaitescu A., Mészáros P., Burrows D., Nousek J., Gehrels N., O’Brien P., Willingale R., 2006, *MNRAS*, 369, 2059
- [186] Panaitescu A., 2007, *MNRAS*, 379, 331
- [187] Pe’er A. & Waxman E., 2004, *ApJ*, 603, L1
- [188] Pe’er A., Mészáros P., Rees M. J., 2006, *ApJ*, 652, 482
- [189] Pe’er A., Mészáros P., Rees M. J., 2006, *ApJ*, 642, 995
- [190] Pei Y. C., 1992, *ApJ*, 395, 130
- [191] Perley D. A. et al., 2008, *ApJ*, 672, 449
- [192] Perna R. & MacFadyen A., 2010, *ApJ*, 710, L103
- [193] Piran T., Shemi A., Narayan R., 1993, *MNRAS*, 263, 861
- [194] Piran T., 1999, *Physics Reports*, 314, 575
- [195] Piran T., 2005, *Rev. Mod. Phys.*, 76, 1143
- [196] Piran T., Sari R., Zou Y.-C., 2009, *MNRAS*, 393, 1107
- [197] Piro L. et al., 1998, *A&A*, 331, L41
- [198] Popham R., Woosley S. E., Fryer C., 1999, *ApJ*, 518, 356
- [199] Predehl P., Schmitt J. H. M. M., 1995, *A&A*, 293, 889
- [200] Preece, R. D., Pendleton, G. N., et al. 1998, *ApJ*, 496, 849

- [201] Preece, R. D., Briggs, M. S., Mallozzi, R. S., et al. 2000, *ApJS*, 126, 19
- [202] Preece, R. D., Briggs, M. S., Giblin, T. W., et al., 2002, *ApJ*, 581, 1248
- [203] Racusin J. L. et al., 2008, *Nature*, 455, 183
- [204] Ramirez-Ruiz E. & Fenimore E. E., 2000, *ApJ*, 539, 712
- [205] Ramirez-Ruiz E., Celotti A. & Rees M. J., 2002, *MNRAS*, 337, 1349
- [206] Rees M. J., Mészáros P., 1992, *MNRAS*, 258, 41
- [207] Rees M. J., Mészáros P., 1994, *ApJ*, 430, L93
- [208] Rees M. J., Mészáros P., 2005, *ApJ*, 628, 847
- [209] Romano P. et al., 2006, *A&A*, 456, 917
- [210] Roming, P. W. A. et al., 2005, *Space Sci. Rev.*, 120, 95
- [211] Rosswog S. & Davies M. B., 2002, *MNRAS*, 334, 481
- [212] Rosswog S. & Liebendörfer M., 2003, *MNRAS*, 342, 673
- [213] Rosswog S., Ramirez-Ruiz E., Davies M. B., 2003, *MNRAS*, 345, 1077
- [214] Rosswog S., 2007, *MNRAS*, 376, L48
- [215] Rybicki G. B., Lightman A. P., 1979, *Radiative Processes in Astrophysics*. Wiley-Interscience Press, New York.
- [216] Rykoff E. S. et al., 2009, *ApJ*, 702, 489
- [217] Ryde F., Björnsson C.-I., Kaneko Y., Mészáros P., Preece R., Battelino M., 2006, *ApJ*, 652, 1400
- [218] Ryde F. & Pe'er A., 2009, *ApJ*, 702, 1211
- [219] Sakamoto, T., Lamb, D. Q., Kawai, N., et al., 2005, *ApJ*, 629, 311
- [220] Sari R., Piran T., Narayan R., 1998, *ApJ*, 497, L17

- [221] Sari R., Piran T., 1999, ApJ, 520, 641
- [222] Schady P. et al., 2007, MNRAS, 377, 273
- [223] Shao L., Dai Z. G., 2007, ApJ, 660, 1319
- [224] Shao L., Dai Z. G., Mirabal N., 2008, ApJ, 675, 507
- [225] Shemi A., Piran T., 1990, ApJ, 365, L55
- [226] Shen R., Kumar P., Robinson E. L., 2006, MNRAS, 371, 1441
- [227] Shen R.-F., Barniol Duran R., Kumar P., 2008, MNRAS, 384, 1129
- [228] Shen R.-F., Willingale R., Kumar P., O'Brien P. T., Evans P. A., 2009, MNRAS, 393, 598
- [229] Shen R.-F., Zhang B., 2009, MNRAS, 398, 1936
- [230] Shen R., Kumar P., Piran T., 2010, MNRAS, 403, 229
- [231] Sikora, M., Begelman, M. C., Rees, M. J., 1994, ApJ, 421, 153
- [232] Smith R. K., Dwek E., 1998, ApJ, 503, 831
- [233] Stanek K. Z. et al., 1999, ApJ, 522, L39
- [234] Stanek K. Z. et al., 2007, ApJ, 654, L21
- [235] Stern B. in: Poutanen J, Svensson R, eds. High Energy Processes in Accreting Black Holes, ASP Conference Series 161. San Francisco: ASP, 1999, p277
- [236] Tanaka M. et al., 2009, ApJ, 692, 1131
- [237] Thoene C. C. et al., 2006, GCN Circ. 5373
- [238] Thoene C. C., Perley D. A., Bloom J. S., 2007, GCN Circ. 6663
- [239] Thompson C., Mészáros P., Rees M. J., 2007, ApJ, 666, 1012
- [240] Thompson T. A., Chang P., Quataert E., 2004, ApJ, 611, 380

- [241] Uhm Z. L., Beloborodov A. M., 2007, *ApJ*, 665, L93
- [242] Usov V. V., 1992, *Nature*, 357, 472
- [243] Uzdensky D. A., MacFadyen A. I., 2006, *ApJ*, 647, 1192
- [244] van de Hulst H. C., 1957, *Light Scattering by Small Particles*. John Wiley & Sons, Inc., New York
- [245] Vestrand W. T. et al., 2002, *Proceedings of SPIE*, 4845, 126
- [246] Vestrand W. T. et al., 2005, *Nature*, 435, 178
- [247] Vestrand W. T. et al., 2006, *Nature*, 442, 172
- [248] Walker K. C., Schaefer B. E. & Fenimore E. E., 2000, *ApJ*, 537, 264
- [249] Waxman E., Draine B. T., 2000, *ApJ*, 537, 796
- [250] Weingartner J. C., Draine B. T., 2001, *ApJ*, 548, 296
- [251] Wheeler C. J., Yi I., Höflich P., Wang L., 2000, *ApJ*, 537, 810
- [252] Wheeler C. J., Meier D. L., Wilson J. R., 2002, *ApJ*, 568, 807
- [253] Willingale R. et al., 2007, *ApJ*, 662, 1093
- [254] Woosley S. E., Bloom J. S., 2006, *ARA&A*, 44, 507
- [255] Woosely S. E., Heger A., 2006, in Holt S. S., Gehrels N., Nousek J. A., eds, *AIP Conf. Proc. Vol. 836, Gamma Ray Bursts in the Swift Era*, American Institute of Physics, Melville, NY, p. 398
- [256] Workman J. C., Morsony B. J., Lazzati D., Medvedev M. V., 2008, *MNRAS*, 386, 199
- [257] Woźniak P. R., Vestrand W. T., Wren J. A., White R. R., Evans S. M., Casperson D., 2006, *ApJ*, 642, L99
- [258] Yost S. A. et al., 2007a, *ApJ*, 657, 925
- [259] Yost S. A. et al., 2007b, *ApJ*, 669, 1107

- [260] Yu Y. W., Dai Z. G., 2007, *A&A*, 470, 119
- [261] Yu Y. W., Dai Z. G., 2009, *ApJ*, 692, 133
- [262] Yu Y. W., Wang X. Y., Dai Z. G., 2009, *ApJ*, 692, 1662
- [263] Zhang B., Mészáros P., 2001, *ApJ*, 552, L35
- [264] Zhang B., Mészáros P., 2002, *ApJ*, 581, 1236
- [265] Zhang B., 2006, *Advances in Space Research*, 40, 1186
- [266] Zhang B., Fan Y. Z., Dyks J., Kobayashi S., Mészáros P., Burrows D. N., Nousek J. A., Gehrels N., 2006, *ApJ*, 642, 354
- [267] Zhang B., 2007, *Chin. J. Astron. Astrophys.*, 7, 1
- [268] Zhang B. et al., 2009, *ApJ*, 703, 1696
- [269] Zhang B., Pe'er A., 2009, *ApJ*, 700, L65
- [270] Zhang B.-B., Zhang B., Liang E.-W., Wang X.-Y., 2009, *ApJ*, 690, L10
- [271] Zhang W., Woosley S. E., Heger A., 2004, *ApJ*, 608, 365

Vita

Rongfeng Shen was born in Xiangyang, Hubei Province, in central China. He attended the County 1st High School in Xiangyang from 1992 to 1995. He obtained his Bachelor Degree of Engineering in Wuhan University of Technology, China, in 1999. At that time he became interested in natural sciences. Then he entered the Institute of High Energy Physics, Chinese Academy of Sciences at Beijing, and studied in the area of high energy astrophysics for his Master of Sciences degree from 1999 to 2003. During the following year, he worked at the Institute of High Energy Physics as a Guest Researcher. In the summer of 2004, he joined the Graduate School of the University of Texas at Austin.

Permanent Address: 45 Changzheng Rd, Xiangfan, Hubei, 441000, P. R.
China

This dissertation was typeset with $\text{\LaTeX} 2_{\epsilon}^1$ by the author.

¹ $\text{\LaTeX} 2_{\epsilon}$ is an extension of \LaTeX . \LaTeX is a collection of macros for \TeX . \TeX is a trademark of the American Mathematical Society. The macros used in formatting this dissertation were written by Dinesh Das, Department of Computer Sciences, The University of Texas at Austin, and extended by Bert Kay, James A. Bednar, and Ayman El-Khashab.